The Dynamics of the S-Web and Implications for the Solar Wind and Heliosphere

by

Aleida Katherine Higginson

A dissertation submitted in partial fulfillment
of the requirements for the degree of
Doctor of Philosophy
(Atmospheric, Oceanic, and Space Sciences)
in The University of Michigan
2016

Doctoral Committee:

Professor Thomas H. Zurbuchen, Co-Chair
Professor Susan T. Lepri, Co-Chair
Spiro K. Antiochos, NASA Goddard Space Flight Center
Professor Lee W. Hartmann
Professor Justin C. Kasper

This dissertation is not dedicated to any particular person, but is, itself, a testimony to persistence.

ACKNOWLEDGEMENTS

First, thank you to my committee, Thomas Zurbuchen, Sue Lepri, Spiro Antiochos, Justin Kasper, and Lee Hartmann for committing your time to reading and improving my dissertation.

Thank you Spiro Antiochos for your mentorship and for providing such a fantastic work environment. Thank you for teaching me how to have a scientific discussion, to keep an open mind, to think critically, and to never take anything too seriously. Thank you also for teaching me how to present our work so that everyone knows that everything we do is the best, newest, most awesome, and most groundbreaking work EVER. #sweb4eva

Thank you Thomas Zurbuchen for recruiting me to Michigan and SHRG. Thank you for always making sure that I had whatever resources I needed and for never giving up on me. I have no doubt that your continual insistence that I be the most efficient and successful version of myself possible will continue to drive me for the rest of my career.

Thank you Sue Lepri for helping me to understand in-situ data and connect it clearly to my results, but also thank you for your continual support–from admission to qualifying exams to defense. You always made me feel connected to the group even though I was far away at Goddard.

Thank you Rick DeVore for developing the best MHD code currently in existence (obviously) and for setting aside so many hours to teach me how to use it. I'm sorry I broke ARMS so often, but someone had to do it. Thank you for always being available for a consultation.

Thank you to my husband, Joshua Higginson. All my thank yous could never be summarized in a paragraph, but I can at least list a few. Thank you for supporting me through my decision to attend graduate school and the application process. Thank you for dealing with a long-distance relationship for two years and for driving from New Jersey/Delaware to Michigan every month to visit me. Thank you for spending two hours in the car commuting every single day after we got married so I could work at Goddard and we could still live together. Thank you for cooking dinner for me (almost) every night. Thank you for the countless hugs and "How can I help?"s and runs to the grocery store for whatever diabetes-inducing craving I decided would help me to graduate. I could never have done this without you. I hope you take as much pride in the title of Dr. Higginson as I do because the success is partially yours as well.

To my immediate family, you also share in this. Thank you to my parents, Richard Young and Alice Young for always supporting my education in every way. Thank you to my siblings Brandon, Kara, Vance, and Annika for loving me and making me laugh and telling me to keep doing what I'm doing. Thank you to my grandmother, Oma, for praying for me every day. I'm sorry that the quickest route from Maryland to Michigan does not, in fact, run through Canada, no matter how hard you insist that it does. Thank you also to Kathleen Higginson for the love and support and essential shipments of chocolate!

I would never have made it this far without two women in particular. Dr. Gina DiBraccio and Dr. Carrie Black you are both such awesome examples of how to be a badass woman in science and I love you for it. Thank you for always having extra tissues as I fought my way through classes and reminding me how to breathe (literally) when the post-processing seemed to never end and the pressure became too high. You are absolutely rock stars and your friendship is invaluable to me.

Science is a collaborative effort and there are two ways I learned this over the past five years. First, by partly building my dissertation using tools and ideas built by others, and second, by recognizing that no one person can know everything (with the obvious exception of Spiro and Zeus). Thank you to Dr. Mark Stakhiv and Dr. Kalman Knizhnik for helping me learn this second part over and over again. Thank you for always being there to answer my stupid questions and to work through whatever monstrous derivation was assigned to us; without you this process would have taken me much longer. Marcus, thank you for your friendship and support–and I know you know exactly what I mean. Kalman, thank you for your friendship and constant sarcasm. It has been a joy to share an office with you for three years. (Am I serious? You can't tell, can you?!)

Thank you also to the ones who have blazed the trail ahead of me: Ben Lynch, Dan Gershman, Jacob Gruesbeck, Micah Weberg, Sophie Masson, Peter Wyper, and Silvina Guidoni. Thank you for your encouragement, support, and scientific vision. I always left each of our conversations feeling once again that graduation was possible.

I'd like to thank the Harvard-Smithsonian Center for Astrophysics Solar REU program and staff (particularly Kelly Korreck and Kathy Reeves), as well as the students who participated with me in 2010 (both official and honorary). Without this research experience, I never would have discovered solar and helio- physics or considered graduate school. Thank you to my summer adviser, Nick Murphy, for your patience and for not even blinking when I asked you what magnetic reconnection was.

Thank you Dr. Lauren Woolsey, my forever conference buddy and gamer extraordinaire. Thank you for loving me as much as I love you, for always sharing a room with me at conferences (even when it meant not staying in the same room as your husband!), for sending me lovely cards when I most needed them, for introducing me to the world of tabletop games, and for not withdrawing your love when I couldn't stand to play them with you anymore. Thank you also to future Dr. Sam Schonfeld for your ready smile, constant support, and for distracting Lauren when necessary. ;)

Keri Hoadley and Paul Regencia, you both know I wouldn't even have applied to graduate school if our exclusive, VIP GRE study group hadn't magically assembled in 2010. You are brilliant physicists and educators and it is a privilege to watch you change the world.

Thank you also to the other facilitators of my introduction to scientific research. Thank you to Norbert Zacharias and Charlie Finch at the USNO for giving me my first research opportunity and teaching me FORTRAN77 before I even knew what a for-loop was. Thank you to Niescja Turner for being a wonderful undergraduate adviser and research mentor and for teaching me about the magnetosphere. I hope you still have that painting of the Sun-Earth interaction in your office for future students to inquire about. :)

Beyond the world of science (if such a thing exists) there are those friendships that will always stand out to me as essential for the success of this thesis. 629 Brooks St., where would I be without you? Thank you for providing a haven of comfort in Ann Arbor. Even though I only lived there a year and a half, it is forever my permanent Ann Arbor home. Thank you to Kaarin and Ben for being fantastic landlords and neighbors and friends. Thank you to Katherine Mitchell and Elizabeth Matzen for being the best roommates-turned-sisters I couldn't have imagined if I had tried (chocolate and Chakotay forever). I am looking forward to LADYCATION for the rest of my life. A huge thank you to Eva Foti for being the best hostess and lease-taker-over ever!

Dr. Melanie Krook, I would be a different person today if our friendship hadn't developed out of our sense of camaraderie at GradCru. Thank you for getting up at 6 AM to go running with an almost-stranger in 15 degree weather. Thank you for showing me what hard work looks like every day (and every night with those silly cells of yours), and thank you for encouraging and loving me every second of every minute since we met in 2011. I'm already looking forward to our conversations in 2061 and beyond.

To the Shiverseses, I am so thankful for a quiet and steady friendship like ours. Thank you for always encouraging me and baking me cakes. Thank you for all of the deep conversations and late nights which have provided such a welcome rest from my crazy schedule. And especially thank you for sharing Finn-snuggles with me as I finished up this final year.

Future Dr. Kaleb Smith, thank you for being my own personal Dwayne Johnson. You are a wonderful friend and your optimism is contagious. I can't wait to see where your PhD takes you, and, oh yeah, visit you at the beach every year.

Kiefer Zapferstellan, thank you for nearly 15 years of fantastical musings and warm friendship. Our philosophical discussions have always been the highlight of any visit home (or of gym class, depending which decade we're talking about). I'm so looking forward to watching your family grow.

Dear Ms. Susan Jennings, thank you for being my second mom and a wonderful friend. Your constant enthusiasm and joy has brought me countless smiles and I know that graduating was only possible because I had a crazy cheerleader like you.

Mr. Davis Rice, your mentorship and support has been invaluable. Since Day 1 of Latin I you have always provided a quiet place of reflection, be it physical (like a classroom) or metaphorical (like a conversation). And thank you for always, always asking me what I am reading.

Finally thank you to all the members of the AOSS/CLASP family. Thank you to SHRG for helping me learn hard things and providing such a happy place for science. Thank you to all of my fellow students for your help and friendship and thank you to Sandra Pytlinski and Deborah Eddy for ensuring that all technical aspects of my graduate career went as smoothly as possible.

GO BLUE!

TABLE OF CONTENTS

Chapter

LIST OF FIGURES

LIST OF APPENDICES

Appendix

LIST OF ABBREVIATIONS

AIA Atmospheric Imaging Assembly

ARMS Adaptively Refined Magnetohydrodynamic Solver

CMEs Coronal Mass Ejections

FIP First Ionization Potential

HCS Heliospheric Current Sheet

MHD magnetohydrodynamic

PFSS Potential Field Source Surface

SDO Solar Dynamics Observatory

SEPs Solar Energetic Particles

S-Web Separatrix-Web

ABSTRACT

The Dynamics of the S-Web and Implications for the Solar Wind and Heliosphere

by

Aleida Katherine Higginson

Co-Chair: Thomas H. Zurbuchen

Co-Chair: Susan T. Lepri

The Sun's powerful magnetic field is responsible for all the observed properties of the highly dynamic corona and heliosphere, from the solar UV–X-ray radiation, to the composition of solar wind plasma, to the location and acceleration of energetic particles throughout the solar system. Two long-standing mysteries posed by the in situ observations are the large angular extent of slow solar wind about the heliospheric current sheet (HCS) and the large longitudinal spread of impulsive solar energetic particles (SEPs). In the classical picture of the solar/heliospheric magnetic field, slow solar wind should occur only near the HCS and impulsive SEPs should occupy only a narrow spread about the point of origin in the corona. The recently proposed Separatrix-Web (S-Web) Theory postulates that these observations can be explained by the dynamical interaction of open and closed flux in regions of complex magnetic topology. This dissertation presents the first numerical simulations of the dynamic S-Web and rigorously calculates its effects on the slow solar wind and SEP populations. We show that photospheric motions at coronal-hole boundaries are responsible for the release of slow solar wind plasma from the magnetically closed solar corona, specifically through prolific interchange magnetic reconnection. The location of this plasma once it is released into the solar wind depends strongly on the geometry of the coronal-hole flux. We demonstrate how the dynamics at the boundaries of narrow corridors of open flux (coronal hole corridors) are responsible for the observations of slow solar wind plasma at high latitudes in the heliosphere, far from the HCS. Furthermore, we show how energetic particles that are accelerated within a small region on the Sun near a coronal-hole corridor can be observed many tens of degrees in longitude away from the flare region in heliosphere. At the heart of the S-Web theory is the concept that the detailed topology of the Sun's magnetic field is imprinted directly on the heliosphere. Our results show that the complex and dynamic mapping of the magnetic field from the Sun to the heliosphere is essential for understanding the observed properties of interplanetary plasma and particles.

CHAPTER I

Introduction

1.1 The Sun's Atmosphere

The closest thing to a surface on the Sun is the photosphere, a thin layer about 500 km thick with a density around 10^{17} cm^{-3} and a blackbody temperature of 5770 K. This is where the Sun becomes optically thin, allowing photons to freely escape from its interior. It is comprised of mostly neutral hydrogen and helium, with traces of heavier elements. Beneath this surface lies a messy convection zone, a radiative zone, and the Sun's core, where nuclear fusion takes place. These inner layers and their relative thicknesses are shown on the left in Figure 1.1.

Plasma from the convection zone is constantly rising to the photosphere above it, bringing the magnetic field with it. Hot plasma rises at the center of convection cells, pushing plasma to the edges, where it cools and submerges again. The left of Figure 1.2 shows this network of convective cells in an image taken of the quiet sun by the Swedish 1-m Solar Telescope.

The ratio of plasma to magnetic pressures is β:

$$\beta = \frac{nk_BT}{B^2/2\mu_0}, \tag{1.1}$$

where n is the plasma density, k_B is the Boltzmann constant (1.38×10^{-23} kg m^2 s^{-2} K^{-1}), T is the plasma temperature, B is the magnetic field magnitude, and μ_0 is the permeability

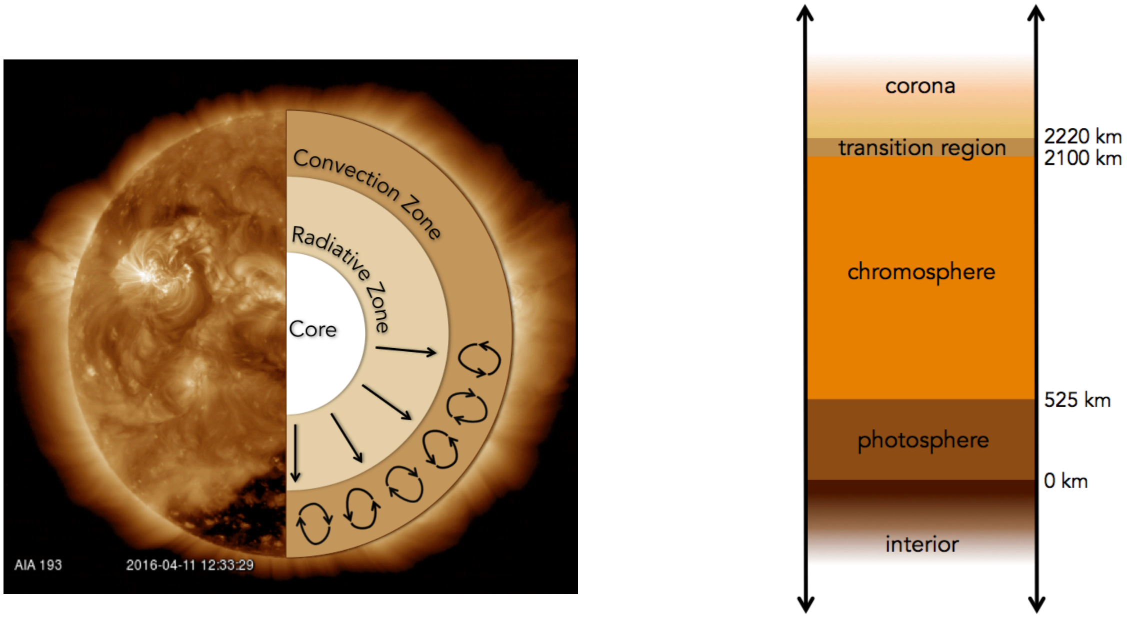

Figure 1.1: (Left) The interior structure of the sun on an image taken by the AIA on board the SDO. The core extends from 0.0 - 0.3 $R_{\odot}$, the radiative zone from 0.3 - 0.7 $R_{\odot}$, and the convection zone from 0.7 - 1.0 $R_{\odot}$. (Right) The layers of the Sun's atmosphere above the photosphere. Adapted from Carroll & Ostlie (2007).

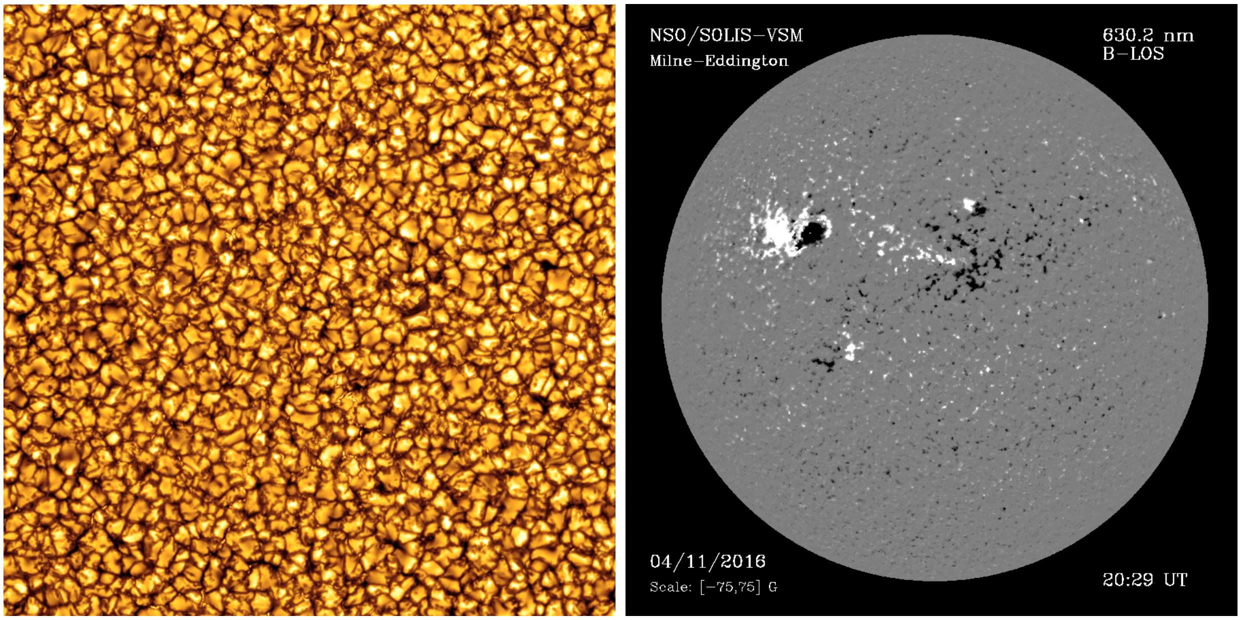

Figure 1.2: (Left) Solar granulation cells in the quiet sun are visible at 436.4 nm. This observation by Michiel van Noort and Luc Rouppe van der Voort on 22 August 2008 was taken by the Swedish 1-m Solar Telescope (SST). (http://www.isf.astro.su.se/) (Right) This magnetogram taken by the Vector Spectromagnetogram instrument at the National Solar Observatory shows large concentrations of magnetic field (active regions) as well as the smaller bunches of flux in the quiet sun. These smaller structures make up the magnetic network.

of free space ($4\pi \times 10^{-7} NA^{-2}$). On the photosphere, β is high, meaning that the plasma is able to move the magnetic field freely. As the convective motions push the magnetic field to the edges of the cells, the magnetic field becomes concentrated in the narrow channels between cells. This pattern in the magnetic field is called the magnetic network.

The right of Figure 1.2 is a magnetogram taken by the Vector Spectromagnetogram instrument at the National Solar Observatory. Here, black and white indicate polarity of the magnetic field. The large regions of strong magnetic field are active regions. Far from these regions, however, in the quiet-sun, are smaller regions of localized magnetic flux which are the bundles of magnetic field piled up in the network between convective cells.

Convective cells exist on two scales. Smaller cells called "granules" are 500 km across and have lifetimes around 5 minutes. "Supergranules" are much larger, around 30,000 km in diameter, with lifetimes $\sim$ 1 day. (*Kivelson and Russell*, 1995) In addition to the radial motion of the plasma outwards from the center of the cells, supergranules exhibit a rotational motion $\sim$ 1 km/s (*Brandt et al.*, 1988; *Duvall and Gizon*, 2000). These photospheric motions have a large effect on the structure of the magnetic field in the atmosphere and it is this process, through the slow build up of energy, that drives much of the explosive and dynamic behavior of the Sun.

Above the photosphere, the Sun's atmosphere experiences dramatic changes in temperature with altitude. These regions and their heights are shown on the right of Figure 1.1. While the top of the photosphere is cooler than the base (at 4400 K), in the chromosphere above it the temperature begins to increase with height. By 2100 km the temperature is near 10,000 K. Above the chromosphere lies the transition region, and above that, the hot, highly-ionized corona. The transition region experiences the largest temperature gradient, rising from chromospheric temperatures to over 1 MK in only $\sim$ 120 km. The source of this heating is one of the major unsolved mysteries in heliophysics.

Despite the high temperature, the drop in density means that the corona is a low β region; now the structure in the magnetic field carries influence over the behavior of the plasma. The amazing complexity of the magnetic field in the corona can be seen in the eclipse image in Figure 1.3. The chromosphere and transition region extend only about 3% of a solar radius away from the surface of the Sun, and so in Figure 1.3, almost the entirety of what the viewer sees is the hot corona.

The magnetic field divides the corona into two topological regions: "closed" and "open." Closed regions are where the magnetic field is connected to the photosphere at both ends. The loop-type structures seen in Figure 1.3 are examples of this. Since the corona is low β, these closed magnetic fields confine the plasma to the corona. Open magnetic field appears as the bright rays near the two poles in Figure 1.3. Here the field is connected to the photosphere at one end, but the other end extends out into the solar system, eventually connecting to the very edge of the heliosphere. In open regions, plasma from the photosphere is able to

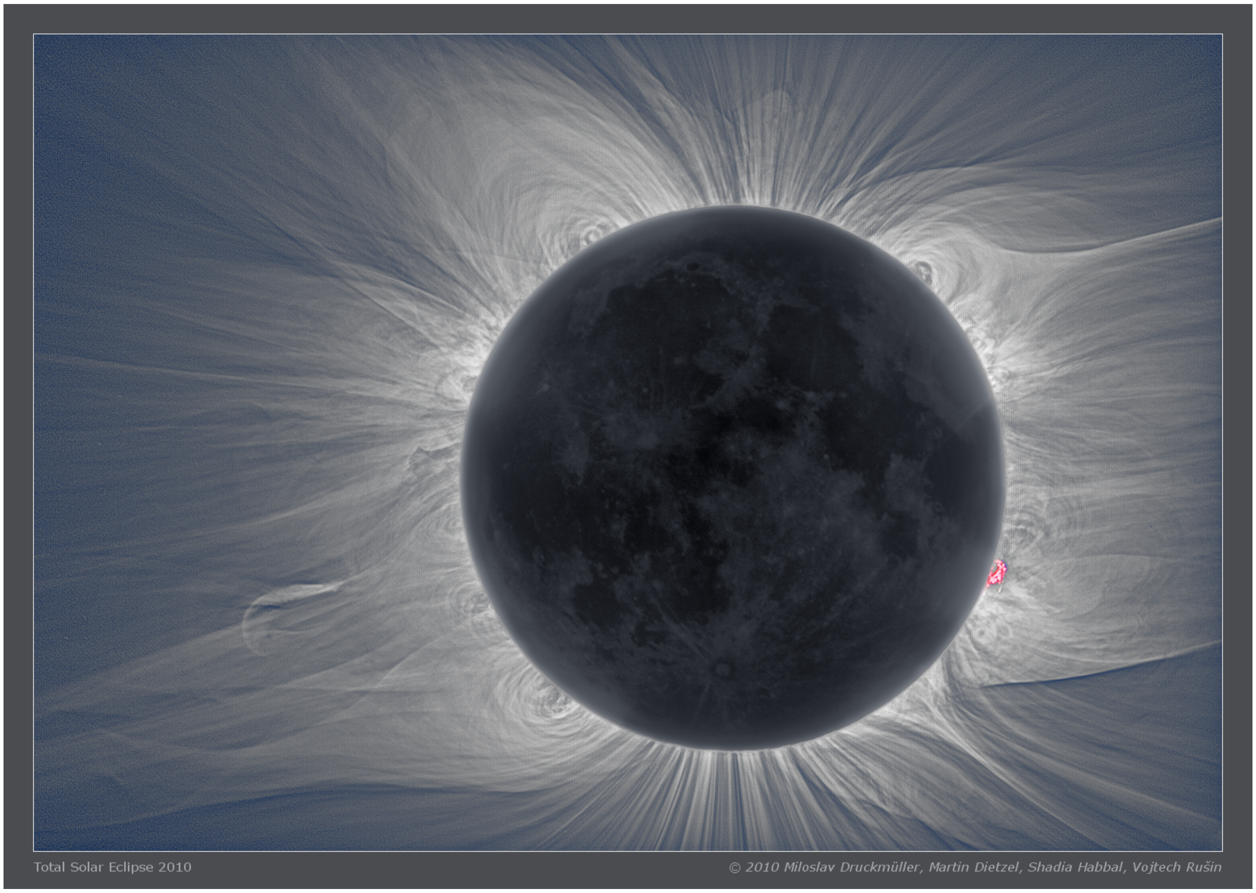

Figure 1.3: A white light image of the solar corona taken during the total solar eclipse on November 11, 2010. (http://www.zam.fme.vutbr.cz/ druck/Eclipse/index.htm)

follow these field lines away from the Sun and become the solar wind.

Regions of open magnetic field are known as coronal holes, since these regions appear dark in EUV imagery and resemble literal holes in the solar atmosphere (see the south pole on the left of Figure 1.1). Above the closed-field regions, the flux from the coronal holes must expand to fill the entire heliosphere. The boundary between the flux systems of opposite polarity coronal holes in the heliosphere is known as the Heliospheric Current Sheet (HCS). When traced back from the solar wind into the corona, this boundary must map back to the boundary between the open and closed magnetic field. This boundary, like the rest of the Sun, is driven by the photospheric motions discussed above, and it is the ensuing dynamics from these motions that we examine in this thesis.

1.2 The Solar Wind

The solar wind is the outwards expansion of the hot solar atmosphere into empty space. It's supersonic nature was predicted by *Parker* (1958), who realized that the exponential pressure decay for a static atmosphere could not approach the emptiness of the interstellar medium. Because an equilibrium is not possible, he argued that the corona must be an expanding transonic fluid, continuously emanating from the Sun. His predictions were verified by in-situ measurements by Mariner II (*Neugebauer and Snyder*, 1962).

The solar wind comes in two flavors, excluding explosive, transient events such as Coronal Mass Ejections (CMEs) and Solar Energetic Particles (SEPs). Generally these two types of solar wind are referred to as ”fast” and ”slow.” The fast solar wind has typical speeds $>$ 500 km/s, while the slow solar wind has speeds $<$ 500 km/s. While they can, as the name suggests, be classified by speed, the plasma composition is a better way to differentiate between the two classes. This is because it is the plasma composition which offers the strongest insight into the source regions of the fast and slow solar wind.

While the fast solar wind is known to originate in coronal holes, the origin of the slow solar wind is still a topic of voracious debate. Any theory for the origin of the slow solar wind must account for four key properties: 1) speed, 2) charge-state composition, 3) elemental composition, and 4) location. To demonstrate these properties, observations from the Ulysses spacecraft are described below. The Ulysses mission was one of the most important missions to-date for studying the structure of the solar wind in the heliosphere. Launched in 1990 and active until 2009, it was the first instrument suite to orbit the Sun outside the plane of the ecliptic. Its orbit extended from 1.3 AU to 5.4 AU, and, at an 80° inclination to the solar equator, it was able to sample all solar latitudes, and all types of solar wind, during both solar minimum and maximum.

Figure 1.4 from *McComas et al.* (2008) illustrates the relationship between 1) and 4) during the three orbits of the Ulysses mission. In panels a through c, a characteristic image of the sun from each time period is shown. The speed of the solar wind is plotted radially over top of this, where the colors represent the polarity of the magnetic field. Panel d shows the sunspot number in black, indicating the level of solar activity during each orbit, and the tilt of the heliospheric current sheet in red. This tilt depends strongly of the configuration of the coronal holes. In panels a and c, during solar minimum, the bright closed-field streamers are confined to the equatorial regions and the flux is roughly dipolar. During these times the tilt is minimal. In panel b, when coronal holes can extend to low latitudes and the coronal-hole boundary can exhibit complicated structure, the dark coronal holes are mixed in with the bright, dense coronal streamers, and during these times the tilt of the heliospheric current sheet can be extreme.

The speed of the solar wind in Figure 1.4 depends strongly on latitude and on the structures in the corona. During solar minimum the highest speed wind occurs over the polar coronal holes, while the slow wind surrounds the streamer belt. During solar maximum, when the coronal holes can occur at all latitudes and the coronal hole boundary is extremely complex, there is a mixing of slow and fast wind over a wide range of latitudes. It is important to note that even during solar minimum, when the slow solar wind surrounds the equatorial region, the slow wind does not exist solely in a thin band in the ecliptic. Any theory for

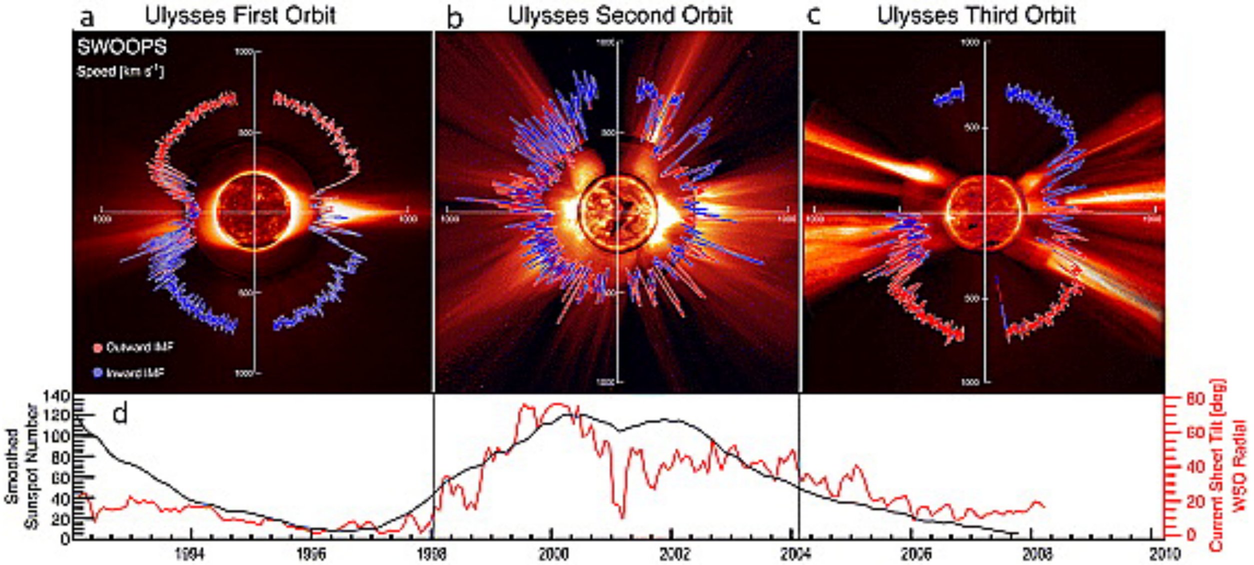

Figure 1.4: (a-c) Polar plots of the solar wind speed for Ulysses' three polar orbits colored to indicate measured magnetic polarity. In each, the earliest times are on the left (nine o'clock position) and progress around counterclockwise. (d) Contemporaneous values for the smoothed sunspot number (black) and heliospheric current sheet tilt (red), lined up to match panels a-c. In panels a-c, the solar wind speed is plotted over characteristic solar images for solar minimum for cycle 22 (8/17/96), solar maximum for cycle 23 (12/07/00), and solar minimum for cycle 23 (03/28/06). From the center out, we blend images from the Solar and Heliospheric Observatory (SOHO) Extreme ultraviolet Imaging Telescope (Fe XII at 1950 nm), the Mauna Loa K coronameter (700950 nm), and the SOHO C2 white light coronagraph. Taken from *McComas et al.* (2008)

the origin of the slow solar wind must be able to explain the large extent of the slow solar wind, which, as seen in Figures 1.4a and 1.4c, can extend up to thirty degrees away from the heliospheric current sheet.

Slow wind origin theories must also be able to explain the hot source region of the slow wind. Figure 1.5 from *Geiss et al.* (1995) illustrates the relationship between 1), 2) and 4). Here data from Ulysses is plotted over four years as the spacecraft made its way from less than 10 degrees latitude up to 80 degrees. These four years stretched from declining solar maximum into solar minimum. Panel A shows the velocity, where the relationship between speed and location is again apparent, with slow wind speeds below 30 degrees and fast wind speeds above the pole. The strong variability between 1992 and 1994 corresponds to the spacecraft repeatedly entering a high-speed stream from a coronal hole with each solar rotation. Panel B shows the "freeze-in" temperature of the solar wind based on the charge-state ratio between O^{7+} and O^{6+}. The charge-states of the oxygen ions (and others, such as carbon) depend on the electron density and temperature, which determines the ionization and recombination rates in the corona. (*Hundhausen et al.*, 1968) As the electron density drops with radius, the collisional rate eventually becomes low enough that the ions no longer evolve, and their states become "frozen in" permanently. These charge-states are determined between 1 and 4 solar radii, and so provide vital information about source region of the plasma.

Comparing Panels A and B reveals the inverse relationship between solar wind speed and freeze-in temperature. The fast wind stemming from coronal holes originates in a much cooler region than the slow solar wind. This dichotomy actually aligns closely with spectroscopic observations of the temperature in the closed and open regions in the corona. Observations of coronal holes yield temperatures around 0.8 MK (*Del Zanna and Bromage*, 1999; *Doschek et al.*, 1997; *Landi*, 2008), while temperatures in the closed-field corona can reach 2 MK (*Feldman et al.*, 1978; *Laming et al.*, 1997; *Warren and Brooks*, 2009). These observations, coupled with the association of the slow solar wind with the closed-field streamer structures

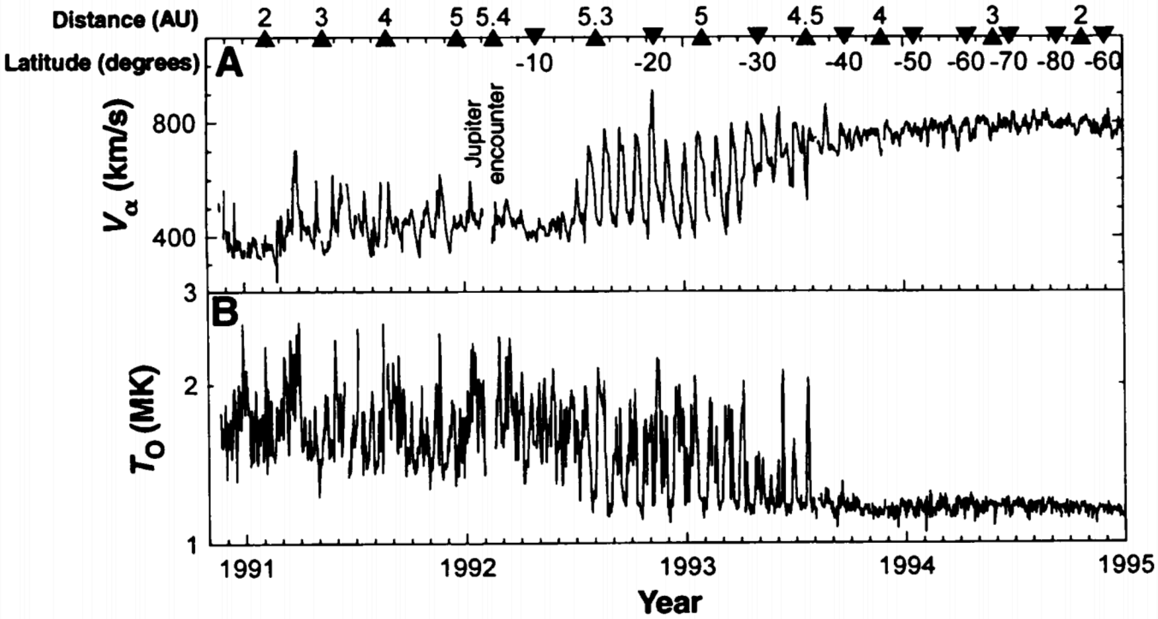

Figure 1.5: The changing solar wind conditions encountered by Ulysses during 4 years of observation. A. The speed of He ions, V_α, and B. the freeze-in temperature of O, T_O, as a function of time and the heliographic latitude of Ulysses (distance from the Sun in astronomical units is also given). The varying conditions at lower latitude contrast with the quiet flow at higher latitude. During 10 months in 1992 and 1993, the spacecraft regularly went into and out of the high speed stream from the southern polar coronal hole. The high speed streamers are identified by the combination of high velocity and low freeze-in temperatures. Taken from *Geiss et al.* (1995).

(see Figure 1.4), strongly suggest that the slow solar wind originates in the hot, magnetically-closed corona.

The last key property of the slow wind plasma, its elemental composition, also supports this hypothesis. Figure 1.6 from *von Steiger and Zurbuchen* (2011) shows an overview of key quantities 1), 2), 3), and 4) throughout the lifetime of the mission. Panel a shows the wind speed, panel b shows the derived freeze-in temperature for oxygen, panel c shows the ratio of iron to oxygen, and panel d shows the sunspot number (indicating solar activity level). The yellow bars shows time periods where the spacecraft was above 70° latitude and over a coronal hole. In panels a), b), the relationship between speed, freeze-in temperature, and location shown in Figures 1.4 and 1.5 holds throughout the lifetime of the mission, during both solar minimum and solar maximum. Panel c shows that there also exists an inverse relationship between the speed of the solar wind and the enhancement in the abundance of elements like iron over oxygen. This trend is the so-called ”First Ionization Potential (FIP) Effect” (e.g. *Meyer*, 1985).

Spectroscopic observations show that, in the corona, elements with FIPs above 10 eV are enhanced above their photospheric values, and that their degree of enhancements is ordered by their FIP (*Pottasch*, 1963; *Feldman and Laming*, 2000; *Laming*, 2004). While the exact mechanism behind this process is still debated, it is inextricably associated with the closed-field corona. Measurements of newly emerged flux loops by *Sheeley* (1995) and *Widing* (1997) showed originally photospheric abundances, that over the course of ~ 1 day became more FIP biased, eventually reaching coronal values where low FIP elements exhibit an enhancement of up to 4 times their photospheric abundances (*Feldman and Widing*, 2003).

Combining these observations with in-situ measurements such as in Figure 1.6, which show the abundance ratios like Fe/O and Mg/O (*Geiss et al.*, 1995) increase with decreasing solar wind speed again strongly implies that the origin for the slow solar wind must be the hot, coronal plasma from long-lived closed-field loops. However, regardless of a partic-

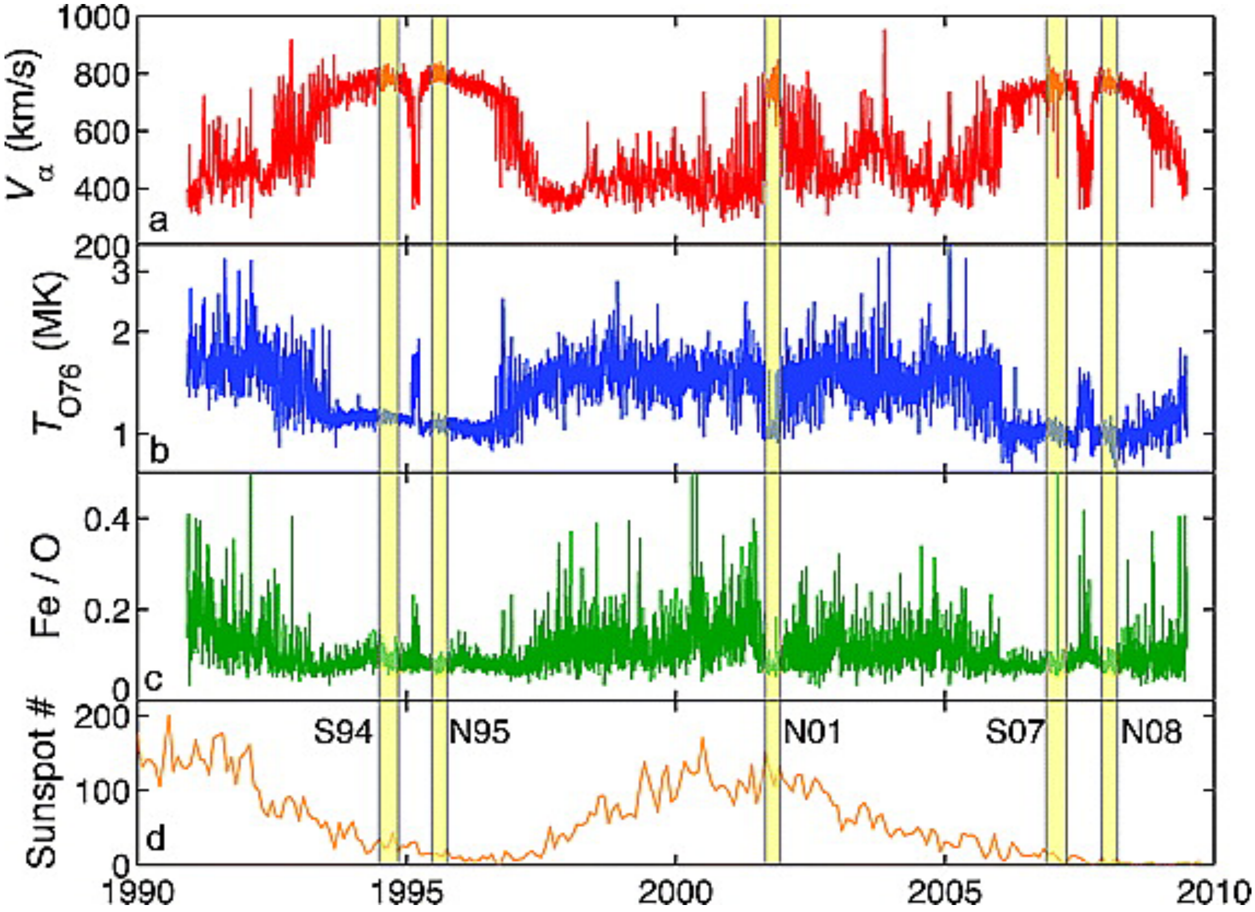

Figure 1.6: Overview of solar wind properties during the entire Ulysses mission: (a) solar wind speed, (b) freezing-in temperature derived from the O7+/O6+ charge state ratio, (c) Fe/O abundance ratio, and (d) mean monthly sunspot number. The high-latitude passes when Ulysses was poleward of 70 heliolatitude are indicated by shaded bands, except for the south polar pass in 2000 as this was not dominated by a high-speed stream due to solar maximum conditions during that time period. Taken from *von Steiger and Zurbuchen* (2011)

ular origin theory's chosen source region, to be complete it must able to account for the elemental abundances and the three other key properties of the slow solar wind, which, repeated together are: 1) speed, 2) charge-state composition, 3) elemental composition, and 4) location.

There are several theories for the origin of the slow solar wind. The expansion factor model hypothesizes that the slow wind originates from the very edges of coronal holes (*Wang and Sheeley*, 1990; *Cranmer et al.*, 2007). These edges can have extremely large magnetic field expansion factors, meaning that they expand super-radially. This inherently steady-state model predicts that the solar wind at these edges is slowed down by the difference in momentum deposition between the centers and edges of coronal holes. The differences in speed must arise when similarly-sized flux tubes at the center and the edges of the coronal holes low in the corona experience the same acceleration mechanisms, but the flux tubes at the edges must expand to fill much larger swaths of the heliosphere than the flux tubes at the center of coronal holes. Recent modeling efforts have shown that, through the effects of a particular form of Alfvén wave heating, it is possible to achieve the charge-state differences between the fast wind, in this case coming from the centers of coronal holes, and the slow wind, coming from the edges (*Oran et al.*, 2015). It remains to be seen, however, how this theory can account for the observed differences in elemental composition.

The streamer top model predicts that the slow solar wind is streaming away from the tops of helmet streamers. Observations of magnetic disconnection events in these regions show many "blobs" moving away into the solar wind (e.g. *Suess et al.*, 1996; *Sheeley et al.*, 1997). While these blobs would contain hot, coronal plasma, there are two problems that this theory alone cannot account for. First, the number of these blobs can in no way account for the bulk of the slow wind that is observed. Earth is embedded in slow solar wind 70% of the time, and these blobs do not occur frequently enough to explain the long duration of slow wind periods. Second, it constrains the location of the slow solar wind too tightly. By this model, the slow solar wind would only be observed directly along the HCS. As discussed above, the Ulysses observations show that the slow solar wind, even at solar minimum, can be found at high-latitudes, up to thirty degrees away from the heliospheric current sheet.

The interchange model (*Fisk et al.*, 1998; *Fisk*, 2003; *Fisk and Zhao*, 2009) predicts that the open field from coronal holes is able to diffuse everywhere into the closed-field regions. Here, the field lines are able to undergo interchange reconnection. In this process, and open and closed magnetic field line come together and reconnect in a 3D fashion which results in the switching of their foot points. The open end of the field line in the heliosphere remains unaffected, but in the low corona it is now connected to a foot point which used to be closed. This newly opened section of the field line contains hot corona plasma. This plasma, which was previously trapped in the corona, is now able to stream away into the solar wind. This model would give the slow solar wind the correct closed-loop plasma, but there are no observations of open magnetic fields penetrating deep into the closed-field corona. Additionally, modeling efforts (*Edmondson et al.*, 2010b; *Linker et al.*, 2011) suggest that the coronal hole boundary must remain continuous, restricting the diffusion of open magnetic fields into the closed field region. Finally, while the streamer top model predicts a too-narrow band of slow solar wind, the interchange model provides no limits on the location of the slow solar wind, predicting instead that it could be observed anywhere at any point in the solar cycle.

The S-Web model, which is the subject of this dissertation, is currently the only model capable of explaining all four of the key properties of the slow solar wind. It assumes that the source region of the slow wind is the closed-field corona, and that reconnection allowed only along the structured coronal-hole boundary is responsible for its release. As described in detail below, this place's significant constraints on the location of the slow solar wind, while also predicting that it will be observed at high latitudes above the HCS.

1.3 The S-Web Theory for the Origin of the Slow Solar Wind

The Separatrix-Web (S-Web) Theory, proposed by *Antiochos et al.* (2011), is based on the assumption that the slow solar wind originates in the closed-field corona. To escape, the hot plasma with coronal compositions must make its way from the closed-field regions onto open field lines. The S-Web Theory predicts that magnetic reconnection at the boundary between open and closed field (the coronal hole boundary) provides this escape mechanism. This section describes in detail how the precise configuration of the coronal-hole boundaries allows slow solar wind to escape to high latitudes above the HCS.

Figure 1.7 from *Antiochos et al.* (2011) shows a sketch of how a narrow corridor of open flux maps to an arc above the HCS. Shown here is an inner radial surface, representing the photosphere, and an outer, transparent radial shell representing a surface in the heliosphere above the height of the closed-field region. The yellow region on the inner surface represents the closed field region, and the gray represents a system of coronal holes. There is a large polar coronal hole connected to a smaller coronal hole at lower latitudes by a narrow corridor of open flux. The green line between the yellow and gray sections on the inner surface outlines the coronal hole boundary. This boundary must map to the HCS in the heliosphere, and so the HCS is shown on the outer transparent shell in the same green.

Because the outer shell is above the height of the closed-field corona, all of the flux on this outer shell must originate from inside the system of coronal holes on the inner surface. The red lines show how four points on the inner radial surface connect to the outer shell. The gray arc on the outer shell, which is connected to the HCS on either end, maps to the coronal hole corridor and separates the fluxes from the polar coronal hole and the lower latitude coronal hole. The coronal hole at the pole must expand to map to everywhere above this gray arc on the outer surface, while the flux from the lower latitude coronal hole fills the space between the HCS (green line) and the arc.

It is important to note that the location of the arc depends solely on the ratio of fluxes between the two coronal holes. The width of the corridor itself does not affect the location

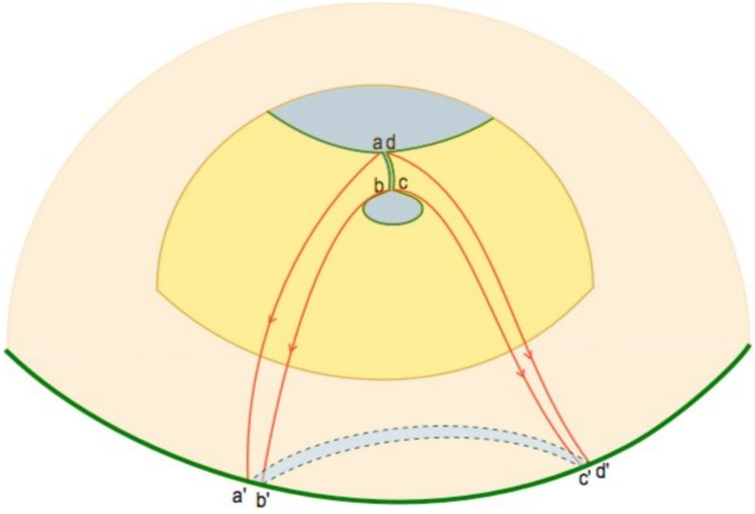

Figure 1.7: Magnetic field topology of an open-field region consisting of a large polar coronal hole and a smaller low-latitude hole connected by an open-field corridor. The inner surface is the photosphere, with the dark gray and bright yellow regions corresponding to open and closed field, respectively. The outer transparent surface is a radial surface in the heliosphere. The dark green line is the polarity inversion line and the light gray arc indicates where the open-field corridor maps to on this outer surface. Taken from *Antiochos et al.* (2011).

or extent of the arc in the heliosphere. The S-Web Theory predicts that if the open-field corridor is sufficiently narrow, such that supergranular motion can stretch across it, then any reconnection along the coronal-hole boundary in this region would result in plasma from closed field lines being released along this S-Web arc. In this way, the S-Web Theory is able to account for the large latitudinal extent of the slow solar wind. The dynamics at the coronal-hole boundary, driven by photospheric motions, are investigated in the chapters below.

Figure 1.8 from *Antiochos et al.* (2011) shows an analytic solution similar to the sketch in Figure 1.7 using the Potential Field Source Surface (PFSS) (*Altschuler and Newkirk*, 1969) model. The top and bottom panels show the same system viewed from different angles. In Figure 1.8 the coronal holes are shown in dark gray while the white regions are closed field. The three groupings of contours in the closed-field regions show the radial component of the magnetic field. These three regions of concentrated flux are placed on top of a background global dipole, which together create the setup shown here. Starting with a background dipole creates a polar coronal hole and a region of closed flux around the equator. The large concentration of flux which is then added near the equator forces the coronal hole to extend down towards the equator. The elephant trunk shape of the coronal hole corridor is then created by placing two concentrates of opposite polarity flux on either side of the lower latitude extension, effectively squeezing it into the this shape. The green magnetic field lines which are plotted here show how the field lines from the open field corridor trace out an S-Web arc in the heliosphere. This magnetic configuration was used in Chapter **??** to numerically model the effect of photospheric driving on an S-Web corridor.

These S-Web arcs must exist in the heliosphere by virtue of the lower latitude coronal holes often observed on the Sun. Figure 1.9 from *Antiochos et al.* (2011) shows the result of a steady-state simulation, performed by Predictive Science, Inc., which uses an observed distribution of magnetic field on the photosphere as the lower boundary condition. Panel a shows this distribution of flux, while Panel b shows the locations of the coronal for this simulation. The colors indicate polarity. It is obvious that apart from the two polar coronal holes, there are also many coronal holes near the equator for this time period. Many narrow corridors of open flux are also visible here, as well as several coronal holes which appear to be disconnected from their polar counterparts. However, these seemingly disconnected coronal holes must be connected to the polar coronal holes by singular linkages (*Titov et al.*, 2011) because the coronal hole boundary must remain continuous. As described in *Antiochos et al.* (2007), there can be only one coronal hole per polarity region without creating large current sheets in the corona, which are not observed. These singular coronal hole corridors map to high latitudes in the same manner as the corridors of finite width, creating a "web of separatrices" (i.e. the "S-Web") in the heliosphere. Recall that the width of the corridor does not affect its location in the heliosphere. Even a singular corridor would result in the release of plasma due to reconnection, since it is the scale of the driving rather than the width of the corridor that is important. This will be further addressed later on.

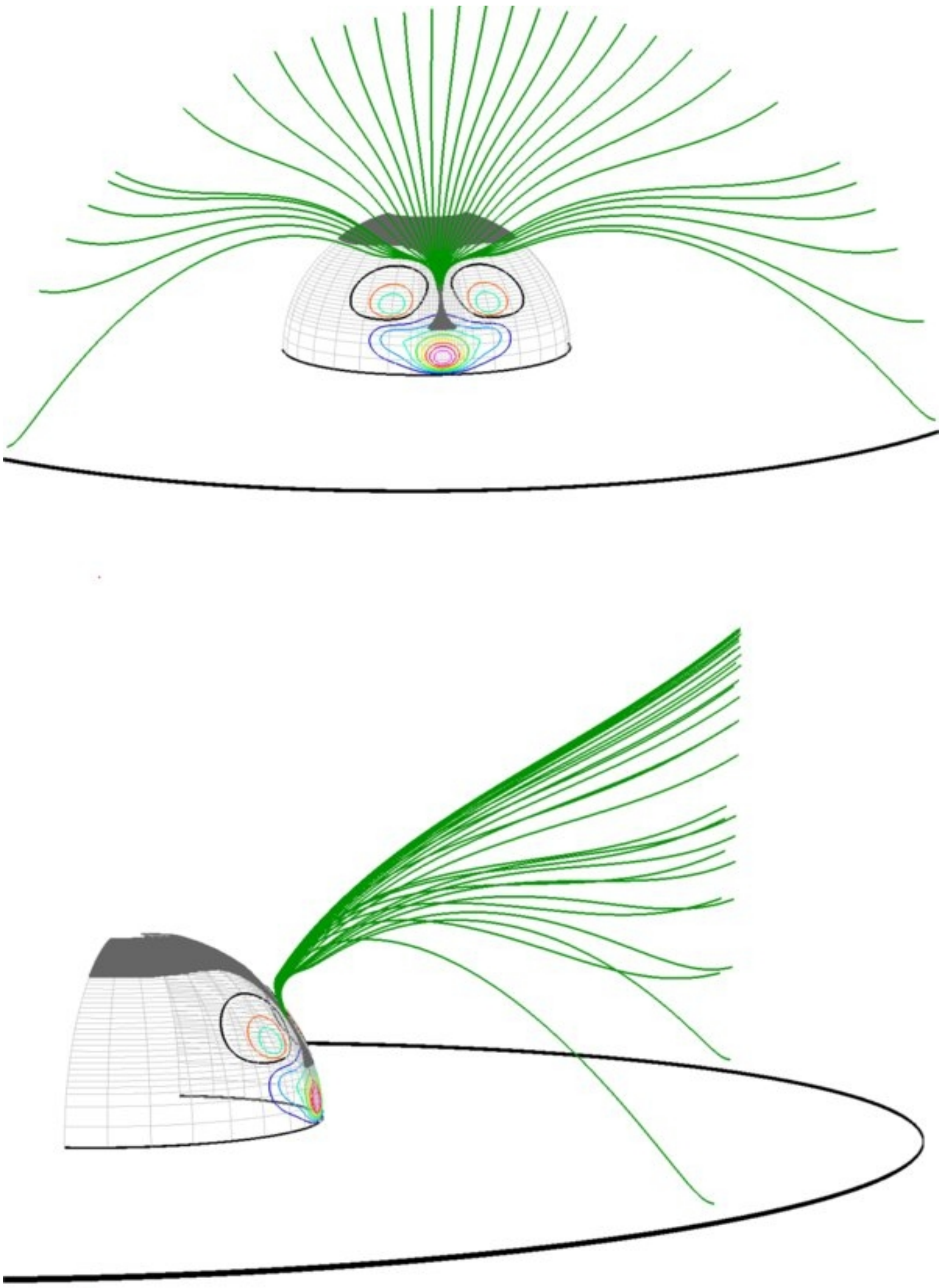

Figure 1.8: Top: open field lines (green) traced from photospheric footpoints along a line segment spanning the narrowest part of the corridor. The lines clearly extend to high latitude above the HCS. Bottom: close-up near the solar surface showing the photospheric footpoints of the corridor field lines. Taken from *Antiochos et al.* (2011).

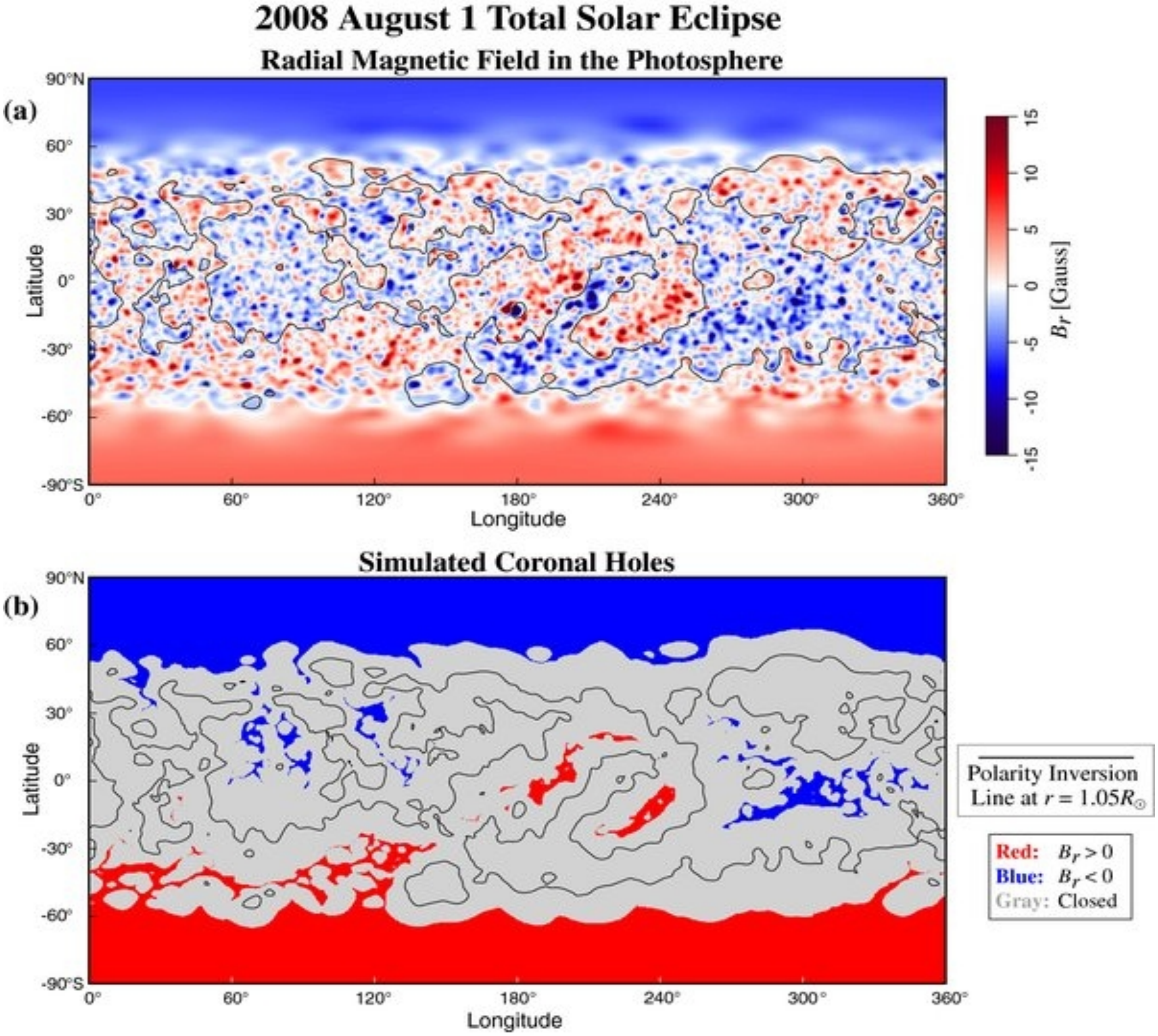

Figure 1.9: (a) Distribution of the radial component of the magnetic field in the photosphere that was used in the MHD simulation to predict the structure of the corona for the 2008 August 1 eclipse, as deduced from MDI measurements. (b) The open- and closed-field regions in the photosphere as determined from the MHD solution. The polarity inversion line ($Br = 0$) at a height $r = 1.05R$ is superimposed on these images to aid in identifying the polarity of the large-scale magnetic flux. Taken from *Antiochos et al.* (2011).

To visualize the "web of separatrices" comprising the S-Web, we turn the the topological quantity Q, the squashing factor. The squashing factor is defined as:

$$Q = \frac{N^2}{|\Delta|} \tag{1.2}$$

where N represents the norm of the mapping of a set of field lines between two surfaces, and Δ is the determinant of the Jacobian matrix describing that mapping. (For a rigorous derivation the reader is referred to *Titov et al.* (2002).) The squashing factor quantifies the gradients that exist in the mapping of the magnetic field between those surfaces. In regions of high Q two magnetic field lines are found close together on one surface, but map to disparate locations on the other surface. The greater the difference in the mapping, the larger the value of Q. Places of high Q are known to be locations where magnetic reconnection is likely to take place (*Lau and Finn*, 1990; *Priest and Titov*, 1996; *Longcope*, 2001; *Parnell et al.*, 2010; *Titov et al.*, 2011) and the S-Web theory predicts that this effect will be amplified by photospheric motions.

Figure 1.10 shows the Q-map corresponding to Figure 1.9. The largest value of Q is at the heliospheric current sheet, shown as the black line. Here, field lines on either side map back to different polarity coronal holes on the Sun, separated by large regions of closed field. The dark red arcs of high Q are from the corridors of open field which are shown in Figure 1.9. Theses are regions where, as can be seen in the shape of the green field lines in Figure 1.8, field lines which have foot points very close together on the photosphere (in the corridors) map to a very large region in the heliosphere, with a wide latitudinal and longitudinal extent. Together, this S-Web and the HCS show regions where reconnection is likely to take place and where the slow solar wind will be released via magnetic reconnection at the coronal-hole boundary. Notice that the S-Web Theory encompasses and extends the streamer top model, predicting that slow solar wind should be present all along the HCS, as well as at high latitudes.

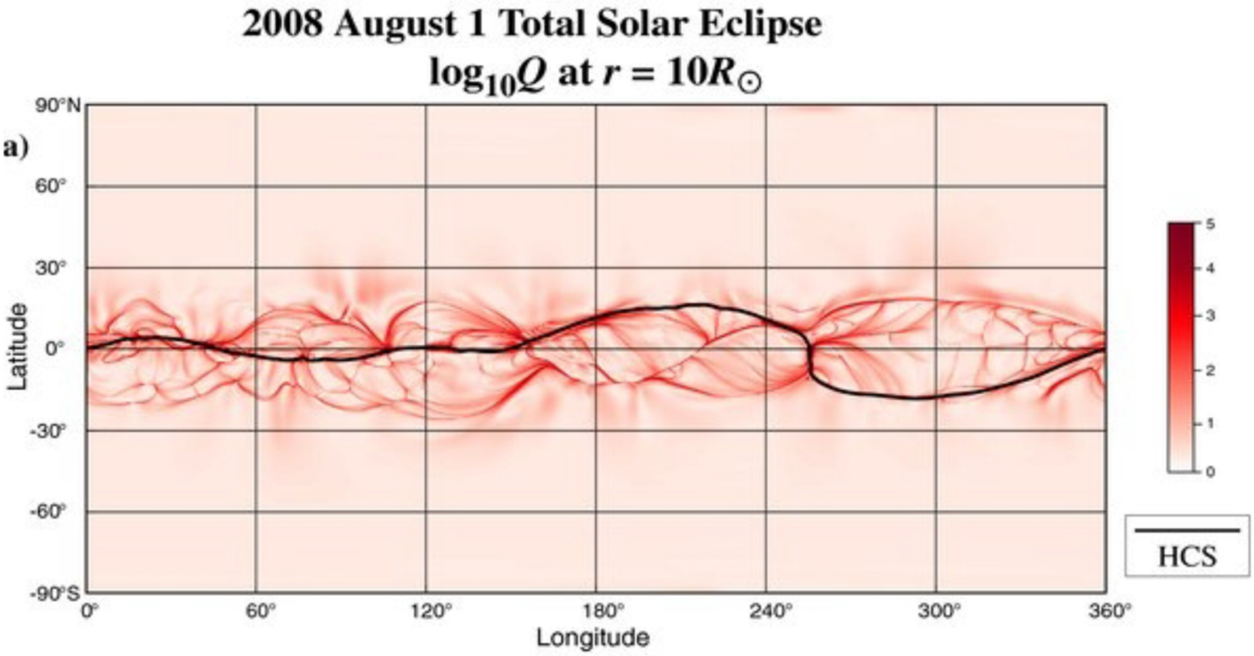

Figure 1.10: Plot of the squashing factor Q in the spherical surface r = 10R on a logarithmic scale vs. longitude and latitude. The HCS (i.e., the location of Br = 0) is superimposed on this image as a thick black line. The complex structure in Q in the vicinity of the HCS is produced by the S-web. Taken from (*Antiochos et al.*, 2011).

The S-Web shown in Figure 1.10 shows a steady-state solution for the photospheric flux distribution shown in Figure 1.9. If this S-Web was not dynamic, but only evolved slowly with the emergence and submergence of new flux regions on the Sun, then it could not be responsible for the bulk of the slow solar wind observed. The widths of these high-Q arcs as shown are too singular. While Figure 1.10 shows the spatial distribution of a band of intermittent slow solar wind which can extend up to 30 degrees away from the heliospheric current sheet (as observed by Ulysses), the amount of solar wind that would be released by reconnection along these arcs would likely not be enough to account for observations. The key is the present of dynamics caused by photospheric driving on top of the S-Web. The S-Web theory predicts that supergranule-scale driving will broaden each of the S-Web arcs, resulting in the release of enough plasma to account for the slow solar wind. It is this dynamic aspect of the S-Web that is tested in this dissertation. Presented in the subsequent chapters are the first ever dynamic simulations of the S-Web and an evaluation of the effects on the solar wind and heliosphere. The next section describes three questions which guided the scope of this research.

1.4 Guiding Science Questions

1.4.1 Do motions at coronal-hole boundaries broaden the S-Web?

In order to account for the bulk of the slow solar wind, S-Web arcs must have a characteristic dynamic width larger than what can be described by steady-state models. This dynamic width should not depend on the width of the S-Web corridors themselves, but rather on the scale of the photospheric driving. Chapter 2 investigates the effect of photospheric driving on the width of the dynamic region of a simple coronal-hole boundary. It also investigates whether or not the nature of the dynamics due to this driving can result in the release of closed-field plasma into the solar wind.

1.4.2 Can the dynamics along the boundary of a coronal-hole corridor release slow solar wind plasma at high latitudes?

While Chapter 2 seeks to quantify the dynamics along a simple coronal-hole boundary, Chapter 3 presents numerical simulations of photospheric driving along an S-Web corridor. This work was performed in order to test the key hypotheses of the S-Web model and answer the questions: a) Can the dynamics along the boundary of a coronal-hole corridor release slow solar wind from closed-field regions? and b) Would this plasma be observed at high latitudes? The high-latitude observations are the hardest property of the slow solar wind to explain and are the motivating factor behind the development of the S-Web Theory.

1.4.3 What is the nature of these dynamics and what is their effect on the heliosphere?

The nature of the dynamics caused by photospheric motions on coronal-hole boundaries has an important effect on the magnetic field throughout the heliosphere, which can effect not just the solar wind but all manner of particle populations. For example, high-energy Solar Energetic Particles (SEPs) are often observed simultaneously over a broad range of longitudes and latitudes. This apparent diffusion has yet to be fully described, but it is highly likely that S-Web dynamics must play a role. In Chapter 4, we address how S-Web dynamics may account for these puzzling observations.

CHAPTER II

Dynamics of Coronal-Hole Boundaries

This chapter is taken from A. K. Higginson, S. K. Antiochos, C. R. DeVore, P. F. Wyper, and T. H. Zurbuchen (2016), Dynamics of coronal-hole boundaries, submitted to The Astrophysical Journal.

2.1 Abstract

Remote and in-situ observations suggest that the slow solar wind consists of plasma from the hot, closed-field corona that is released onto open magnetic field lines. The Separatrix-Web (S-Web) theory for the slow wind proposes that photospheric motions, at the scale of supergranules, are responsible for generating dynamics at coronal-hole boundaries, which result in the inferred necessary transfer of plasma from closed to open field lines. We use 3D magnetohydrodynamic (MHD) simulations to determine the effect of photospheric flows on the open and closed magnetic flux of a model corona with a dipole magnetic field and an isothermal solar wind. We find that a supergranular-scale photospheric motion at the boundary between the coronal hole and helmet streamer results in prolific and efficient interchange reconnection between open and closed flux. This reconnection acts to smooth the large- and small-scale structure introduced by the photospheric flows. Magnetic flux near the coronal-hole boundary experiences multiple interchange events, with some flux interchanging over fifty times in one day. Additionally, we find that this interchange reconnection occurs

all along the coronal-hole boundary, even producing a lasting change in magnetic-field connectivity in regions that were not driven by the applied photospheric motions. Our results imply that interchange reconnection is the dominant form of dynamics along open-closed boundaries and should be ubiquitous in the Sun and heliosphere. We discuss the implications of our simulations for understanding the observed properties of the slow solar wind, with particular focus on the global-scale consequences of interchange reconnection.

2.2 Introduction

Understanding how the plasma and magnetic field of the Sun's atmosphere – from the photosphere to the lower corona – extend outward to form the heliosphere has long been one of the central goals of Heliophysics. In his pioneering work, *Parker* (1958) gave the simplest model for this Sun-heliosphere connection. Parker proved that for a spherically symmetric atmosphere maintained at a roughly constant temperature by some coronal heating process, the plasma would expand outward to form a steady supersonic solar wind. Remote-sensing observations of the solar corona, however, such as the exquisite eclipse photographs of *Druckmüller* (2009) and the ultra-high resolution XUV images from *Hinode* and the *Solar Dynamics Observatory* (e.g. *Schrijver et al.*, 2013), show that the solar corona is very far from spherical symmetry due to the action of the Sun's magnetic field. The field adds both structure and dynamics to the basic picture proposed by Parker, affecting both its large-scale organization and also the thermal properties of the solar wind through small-scale dynamics.

The most fundamental structure introduced by the field is that it divides the corona into magnetically "closed" and "open" regions. In closed regions, the field lines have finite length and connect at two points down to the photosphere, confining the plasma. In open regions, the field lines do not connect back to the photosphere within the inner corona and stretch out indefinitely to form the heliosphere. Note that, for a truly steady state, the solar wind can originate only from the open-field regions.

These two types of coronal regions are readily apparent in X-ray/XUV images of the Sun, because of the differences in the properties of their plasma. In closed regions where the plasma is confined, both the density and temperature tend to be high, $N \sim 1 \times 10^9$ cm^{-3} and $T \sim 1$ MK (*Feldman et al.*, 1978; *Laming et al.*, 1997; *Warren and Brooks*, 2009), whereas in open regions, $N \sim 2 \times 10^8$ cm^{-3} and $T \sim 0.8$ MK (*Del Zanna and Bromage*, 1999; *Doschek et al.*, 1997; *Landi*, 2008). As a result, the open regions are often observed to be dark in X-ray images and are referred to as "coronal holes" (*Zirker*, 1977).

Due to this temperature difference, the plasmas in open and closed regions have different ionic charge-state composition, which is readily seen in spectroscopic observations of the corona (*Doschek and Feldman*, 1977; *Doschek et al.*, 1997). In addition, open and closed plasmas are observed to have very different elemental composition. A key result emphasized by *Meyer* (1985) in his pioneering studies is that the elemental abundances of coronal and heliospheric plasma are sensitive to the first ionization potential (FIP) of the particular element. Many studies have now shown conclusively that in open-field regions the coronal plasma has heavy-element abundances close to those of the photosphere. In closed regions, however, the low FIP elements such as Fe and Mg have an abundance relative to the photosphere that is 4–6 times larger than the abundances of high FIP elements, such as N and Ar (*Meyer*, 1985; *Feldman and Widing*, 2003; *Laming*, 2015; *von Steiger and Zurbuchen*, 2016).

This striking abundance variation also shows up in the plasma of the solar wind. It has long been known that the solar wind consists of two distinct types, the so-called fast wind with speeds > 500 km s^{-1}and the slow wind with speeds < 500 km s^{-1}. The fast wind is generally believed to originate in coronal holes. For example, the Ulysses measurements show that during solar minimum the wind at high latitudes that emanates from the polar coronal holes is all fast wind (*Zurbuchen*, 2007, and references therein; *McComas et al.* (2008)). Furthermore, this wind exhibits both elemental abundances and ionic charge states indicative of a source back near the Sun that is similar to coronal-hole plasma (*Geiss et al.*, 1995; *von Steiger et al.*, 2000). The fast wind is observed to show little variation in speed and composition. Consequently, it can be thought of as the quasi-steady wind predicted by *Parker* (1958), although with different physical processes as its source.

The slow wind, on the other hand, has very different properties and its source at the Sun is still an issue of intense debate. During solar minimum the slow wind is found only at low latitudes (*Manoharan*, 2012) and appears to be associated with streamers (*Raymond et al.*, 1997) and the heliospheric current sheet (HCS) emanating from the top of the closed-field region (*Gosling*, 1997; *Zhao et al.*, 2009). The HCS is always embedded in slow wind, never fast (*Burlaga et al.*, 2002). The location and composition of the slow wind suggest that it is somehow associated with the closed-field regions. Furthermore, the slow wind has elemental composition similar to that of closed-field plasma, and its ionic charge states indicate a source plasma with temperature similar to that of the closed corona rather than coronal holes (*von Steiger et al.*, 1997, 2001; *Zurbuchen et al.*, 1999, 2002). In fact, several authors now argue that plasma composition is a much better discriminator between the two types of wind than the flow speed (e.g. *Zhao et al.*, 2009).

The third major feature of the slow wind that distinguishes it from the fast is its variability. The slow wind exhibits continuous, strong variability in all plasma properties, especially composition and density (*Gosling*, 1997). This variability appears to be related to specific structures and not the consequences of simple Alfvénic turbulence observed in the fast wind. In fact, recent results by *Viall and Vourlidas* (2015) and *Kepko et al.* (2016) indicate that 85% or more of the slow wind consists of quasi-periodic structures that vary rapidly, on time scales of hours, in both density and plasma composition. Accompanying these plasma variations is strong variability in the magnetic field measured at 1 AU with clear signatures of plasmoids and disconnected flux (*Kepko et al.*, 2016). These authors conclude that magnetic reconnection in the streamer stalks that map down to the closed-field region is the fundamental process giving rise to the quasi-periodic structures.

As a result of the observations described above, especially the composition and variability measurements, many models postulate that slow wind is due to closed-field plasma that is released onto open field lines (*Antiochos et al.*, 2011; *Fisk*, 2003). This release is believed to occur as a result of the magnetic-field dynamics, specifically reconnection between open and closed flux – so-called interchange reconnection (*Fisk et al.*, 1999; *Crooker et al.*, 2002). There are two main types of magnetically driven dynamical models for the origin of the slow wind. In the interchange model proposed by Fisk and co-workers, open flux is postulated to diffuse throughout the closed regions, releasing closed-field plasma via interchange reconnection (*Fisk et al.*, 1998; *Fisk*, 2003; *Fisk and Zhao*, 2009). It should be noted, however, that the fundamental tenet of this model – open flux can diffuse deep into closed regions – has yet to be demonstrated by rigorous numerical simulations.

A more widely accepted model is the streamer-top model (*Suess et al.*, 1996; *Sheeley et al.*, 1997; *Endeve et al.*, 2004; *Rappazzo et al.*, 2005) and its extension, the Separatrix-Web (S-Web) model, in which the dynamics are localized at the boundary between open and closed flux (*Antiochos et al.*, 2007, 2011). The basic idea of the S-Web model is that the driving of the coronal magnetic field by continual photospheric motions must broaden any open-closed boundary, which for a steady state is a separatrix surface of zero width, into a finite-width dynamic boundary layer. Magnetic flux in this boundary layer constantly opens and closes as a result of interchange reconnection, with closed flux opening and open flux closing. This boundary layer extends out into the heliosphere to form the streamer stalks and embedded HCS.

It should be noted that the dynamical driving of the open-closed boundary has long been proposed to explain a number of observed phenomena. On global scales, the continual opening and closing of coronal-hole boundaries has been invoked (e.g. *Wang et al.*, 1996) as the mechanism that accounts for the apparent rigid rotation of some coronal holes (*Timothy et al.*, 1975; *Zirker*, 1977). On intermediate scales, interchange reconnection at the separatrices that define the tops of pseudostreamers (*Wang et al.*, 2007) is widely believed to be responsible for the bright plasma sheets in the heliosphere (*Hundhausen*, 1972) that define these structures. Finally, on small scales, reconnection at the open-closed boundary separating small closed-field bipoles from the open flux of polar coronal holes is generally accepted to be the mechanism underlying a broad range of activity including spicules, plumes, and jets (e.g. *Pariat et al.*, 2015).

Therefore, calculating and understanding the dynamics of the open-closed boundary driven by photospheric motions is essential for understanding a host of observed solar activity and is at the heart of the S-Web model for the slow wind. Since the photosphere is undergoing turbulent convection, its flows cover all spatial scales ranging from the solar radius down to the viscous dissipation scale, but for S-Web dynamics we can consider these flows to have three dominant scale regimes. For global motions such as the differential rotation or meridional flow that have time scales of many days, much longer than the typical time scale for setting up a steady wind ($\sim$ one day), the open-closed boundary evolution can be considered as quasi-steady. In the other extreme, the small-scale flows of granules and the magnetic carpet (*Schrijver et al.*, 1997), which are of order minutes, are much smaller than a day, so these are likely to produce only Alfvén wave "noise" at the boundary. This noise may play a critical role in heating the plasma and driving the wind, but we do not expect it to be important for releasing the closed-field plasma of the slow wind. The important motions for driving the open-closed boundary are likely to be the supergranular flows, which have time scales of order one day or so.

In this paper, we present the first detailed calculations of the dynamical response of a coronal-hole boundary to driving by supergranular-scale motions. To understand the overall topology and physical mechanisms, these first calculations use the simplest structure for the initial coronal magnetic field and the driving motions. We will show that, although the initial open-closed boundary is the simplest possible, the photospheric driving quickly induces three-dimensional (3D) structure resulting in complex reconnection dynamics between open and closed flux, lending support to S-Web-type models. We emphasize, however, that irrespective of the correct model for the slow solar wind, the results presented below must be a generic feature of corona-heliosphere coupling. Therefore, they must be considered in any analysis and interpretation of observations.

2.3 Method

2.3.1 MHD Model and Initial Conditions

Our calculations use the Adaptively Refined Magnetohydrodynamic Solver (ARMS), which uses Flux Corrected Transport methods to capture shocks and minimize diffusion (*DeVore*, 1991). Our numerical domain consists of a spherical wedge centered on the Sun, in which we solve the following ideal MHD equations:

$$\frac{\partial \rho}{\partial t} + \nabla \cdot (\rho \mathbf{u}) = 0, \tag{2.1}$$

$$\frac{\partial \rho \mathbf{u}}{\partial t} + \nabla \cdot (\rho \mathbf{u}\mathbf{u}) = \frac{1}{4\pi} (\nabla \times \mathbf{B}) \times \mathbf{B} - \nabla P + \rho \mathbf{g}, \tag{2.2}$$

$$\frac{\partial \mathbf{B}}{\partial t} - \nabla \times (\mathbf{u} \times \mathbf{B}) = 0, \tag{2.3}$$

where ρ is the plasma mass density, $\mathbf{u}$ is the plasma velocity, $\mathbf{B}$ is the magnetic field, P is the plasma pressure, and $\mathbf{g} = -GM_{\odot}\mathbf{r}/r^3$ is the gravitational acceleration. The plasma pressure is calculated from $P = 2(\rho/m_p)k_B T$, i.e. we assume the simplest solar atmosphere of a fully-ionized hydrogen gas at constant, uniform temperature, $T = 1$MK. ARMS stores the variables on a staggered grid to keep the divergence of the magnetic field fixed at zero to machine precision. It solves the equations using a second-order predictor/corrector in time and a fourth-order integrator in space. Together with the flux limiter, this ensures that magnetic reconnection via numerical diffusion takes place only in regions where the magnetic field develops structure down to the scale of the grid. In these locations, the effective numerical resistivity is determined by the flow speed and grid spacing. Since the main numerical challenge for our simulations is to resolve as much structure as possible with limited computational resources, we do not include an explicit resistivity.

The initial magnetic field is calculated using the Potential Field Source Surface (PFSS) model (*Altschuler and Newkirk*, 1969) for a dipole at Sun center. The dipole strength is chosen so that the magnetic field at 1 $R_\odot$ is equal to 10 G at the poles, which is a good estimate for the quiet-Sun magnetic field (*Long et al.*, 2013). The radius of the source surface, beyond which the initial magnetic field is assumed to be radial, is set at $R_S = 3R_\odot$ (*Schatten et al.*, 1969).

For the initial atmosphere, we use Parker's isothermal, transonic solar-wind solution (*Parker*, 1958). The velocity of the steady, isothermal solar wind is given by

$$\frac{v^2(r)}{c_s^2}\exp\left(1-\frac{v^2(r)}{c_s^2}\right)=\frac{r_s^4}{r^4}\exp\left(4-4\frac{r_s}{r}\right), \tag{2.4}$$

where $v(r)$ is the solar wind velocity, $c_s = 2k_BT_0/m_p$ is the sound speed, and $r_s = GM_\odot m_p/4k_BT_0$ is the sonic point. The plasma number density at the base of the atmosphere is a free parameter that we set to 3.6×10^9 cm^{-3} to yield densities of 10^8–10^9 cm^{-3} in the helmet streamer.

Figure 2.1 shows the spherical wedge domain, for which $R \in [1R_\odot, 30R_\odot]$, $\theta \in [11.25°, 78.75°]$, and $\phi \in [-22.5°, +22.5°]$. Shown on the radial surface is a map of B_r, with green contours drawn to mark the location of the driving (see §2.3.2). Pictured along a slice of constant longitude are the block boundaries, where each block contains $8 \times 8 \times 8$ grid cells. The grid is logarithmically stretched in R. We use an adaptive grid with the highest resolution along the entire coronal-hole boundary and the HCS, as well as a shallow layer of high-resolution cells at the base to capture the velocity gradients where the solar wind is accelerated and the foot point driving is imposed. The finest grid at the surface has $\sim$ 45 points per square degree. The coarsest grids are positioned in the corners of the wedge to save computational resources.

The radial inner boundary is set to be an effusing wall, which allows mass to flow into, but not out of, the system. Here we also line-tie the magnetic field by setting the tangential velocity everywhere on the surface to zero, except for the prescribed flow profile described

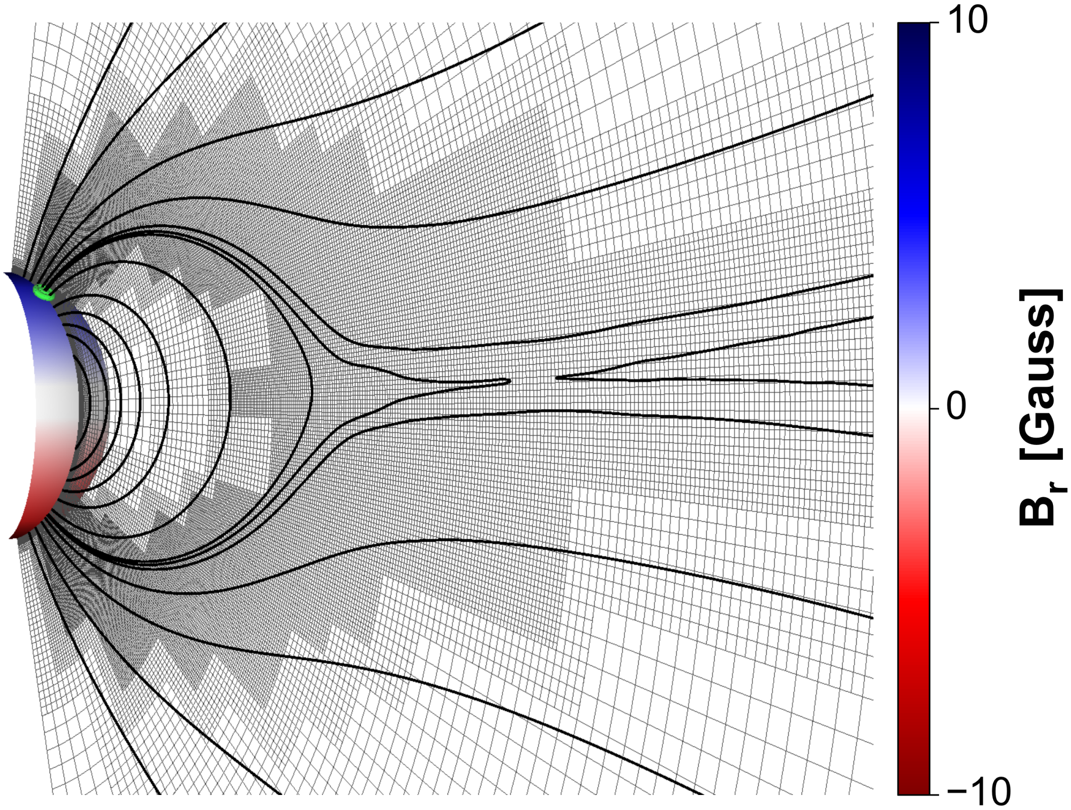

Figure 2.1: Snapshot of the domain after dynamic relaxation to a quasi-steady state. Grid blocks (thin black lines) are shown in the plane $\phi = 0$. Magnetic field lines (thick black curves) in this plane outline a dipolar magnetic field with two polar coronal holes and a helmet streamer that has recently pinched off at the top near the heliospheric current sheet. The solar surface is color-shaded according to the radial magnetic field component. Green contours in the northern hemisphere show the location of the driving-flow annulus straddling the coronal-hole boundary, and are drawn where the tangential velocity magnitude $|\mathbf{V}| = 4$ km s^{-1}.

below (§2.3.2). The three radial guard cells beneath the lower boundary are held fixed at their initial densities, and their velocities are set to zero. All other boundaries allow mass to flow through, with the density and magnetic fields extrapolated using zero-gradient conditions. The velocities at the radial outer boundary assume free-flow-through (zero gradient) for the normal component and semi-slip conditions (zero value outside the boundary) on the tangential components. At the four side walls, the velocities are set to semi-flow-through (zero value outside) for the normal component and free-slip (zero gradient) on the tangential components. These boundary conditions applied to the initial atmosphere produce a self-sustaining, isothermal solar wind throughout the domain, replenished from below in the open-field regions that have sustained upflows.

The initial magnetic field (determined from the PFSS solution) and solar wind are not in equilibrium. Consequently, the first part of our simulation is a relaxation phase where the solar-wind plasma and magnetic field evolve toward a new pressure balance. This relaxed condition is shown in Figure 2.1, where the thick black magnetic field lines outline the coronal holes at both poles, a stretched helmet streamer at the equator, and a dynamic heliospheric current sheet.

We find that this system never reaches a true time-independent steady state, because reconnection continually occurs in the HCS near the top of the helmet streamer. Due to the action of the solar wind, which stretches field lines out to infinity, the HCS continuously thins down until eventually its width reaches the grid scale. Reconnection at the HCS then forms a flux-rope-like structure – often referred to as a streamer blob (e.g. *Sheeley et al.*, 2009) – that is carried outward with the solar wind. In our simulation, the reconnection is determined by the effective numerical resistivity (i.e. the Lundquist number), which scales directly with the grid spacing. Consequently, the blobs become smaller and grow more slowly as the refinement increases. Scaling our results to solar Lundquist numbers, we expect that the blobs formed by this HCS non-equilibrium reconnection process would have no observable consequences in imaging data, at least. For our simulation, the blobs constitute the background dynamics over which we observe the effects of photospheric driving. We point out that the driving has a fixed scale set by observed supergranules and, hence, does not depend upon numerical refinement.

2.3.2 Boundary Driver

The base dynamics in the heliosphere must be determined by the never-ceasing, supergranular-scale, photospheric convection. The actual photospheric horizontal flows due to supergranules are highly complex, as convective cells appear and disappear randomly throughout the photosphere. Furthermore, the motions have both compressible and incompressible components, with the flows expanding out radially from cell centers and converging onto the network, where the misalignment of the flows and their random temporal dependence gives rise to incompressible vortical motions with typical flow speeds of order 1 km s^{-1}(*Brandt et al.*, 1988; *Duvall and Gizon*, 2000; *Gizon and Duvall*, 2003; *Komm et al.*, 2007; *Attie et al.*, 2009; *Seligman et al.*, 2014). For injecting stress into the coronal field, the most important motions are the rotational components. Therefore, for this first investigation of supergranular driving, we use a simple model for a single supergranular flow.

We impose a circular photospheric flow straddling the coronal-hole boundary (the location shown by the green contours on the radial surface in Figure 2.1). This flow lies in the θ,ϕ plane only and is constructed so as to preserve the normal component of the magnetic field during the evolution. In order to satisfy

$$\frac{\partial B_r}{\partial t} = -\nabla_\perp \cdot (\mathbf{v}_\perp B_r) = 0, \tag{2.5}$$

we choose $\mathbf{v}_\perp$ to be equal to the curl of a radial vector,

$$\mathbf{v}_\perp = \nabla_\perp \times (\psi, \mathbf{0}, \mathbf{0}) \,. \tag{2.6}$$

We define ψ as a function of θ, ϕ, and t,

$$\psi\left(\theta, \phi, t\right) \equiv V_0 f(t) g(\xi) h(\beta), \tag{2.7}$$

where

$$\begin{aligned} f(t) &= \frac{1}{2}\left[1 - \cos\left(2\pi k \frac{t - t_0}{t_2 - t_1}\right)\right], && (2.8)\\ g(\xi) &= \frac{(m + l + 1)}{(l + 1)}\left[1 - \xi^{2(l+1)}\right] - \left[1 - \xi^{2(m+l+1)}\right], && (2.9)\\ h(\beta) &= \frac{1}{2}\beta^2. && (2.10) \end{aligned}$$

In the equations above, the parameters k, t_0, t_1, t_2 are set to ramp up the flow to maximum velocity from zero and then from that velocity back to zero. This ensures that all disturbances are smooth. The equation for $g(\xi)$ defines an annulus in spatial coordinate ξ, where

$$\xi^2 \equiv 4\left(\frac{\theta - \theta_0}{\theta_2 - \theta_1}\right)^2 + 4\left(\frac{\phi - \phi_0}{\phi_2 - \phi_1}\right)^2. \tag{2.11}$$

The location of the flow annulus is determined by the limits θ_1, θ_2, and ϕ_1, ϕ_2, with coordinate (θ_0, ϕ_0) representing the center. The thickness and radial velocity profile of the flow annulus are defined by m and l. We set $m = l = 1$ to yield a thick annulus with a velocity peak at the center of the annulus. In the equation for $h(\beta)$, β is the magnetic field coordinate between minimum and maximum strengths, i.e.,

$$\beta \equiv \max\left(\min\left(B_r, B_2\right), B_1\right). \tag{2.12}$$

where we chose $B_1 = 0$ G and $B_2 = 10.0$ G so that $\beta = B_r$ everywhere in our flow region.

A contour map of tangential velocity on the surface is shown in Figure 2.2, where the green velocity contours from Figure 2.1 are shown for context. On the surface, $V_R \approx 0$ so that $|V|$ is essentially the tangential velocity only. The thin black lines show the block boundaries. The flow spans 40×120 grid points and has a diameter of about 1×10^5 km. By comparison, a typical supergranule cell has a diameter of 3×10^4 km (*Simon and Leighton*, 1964).

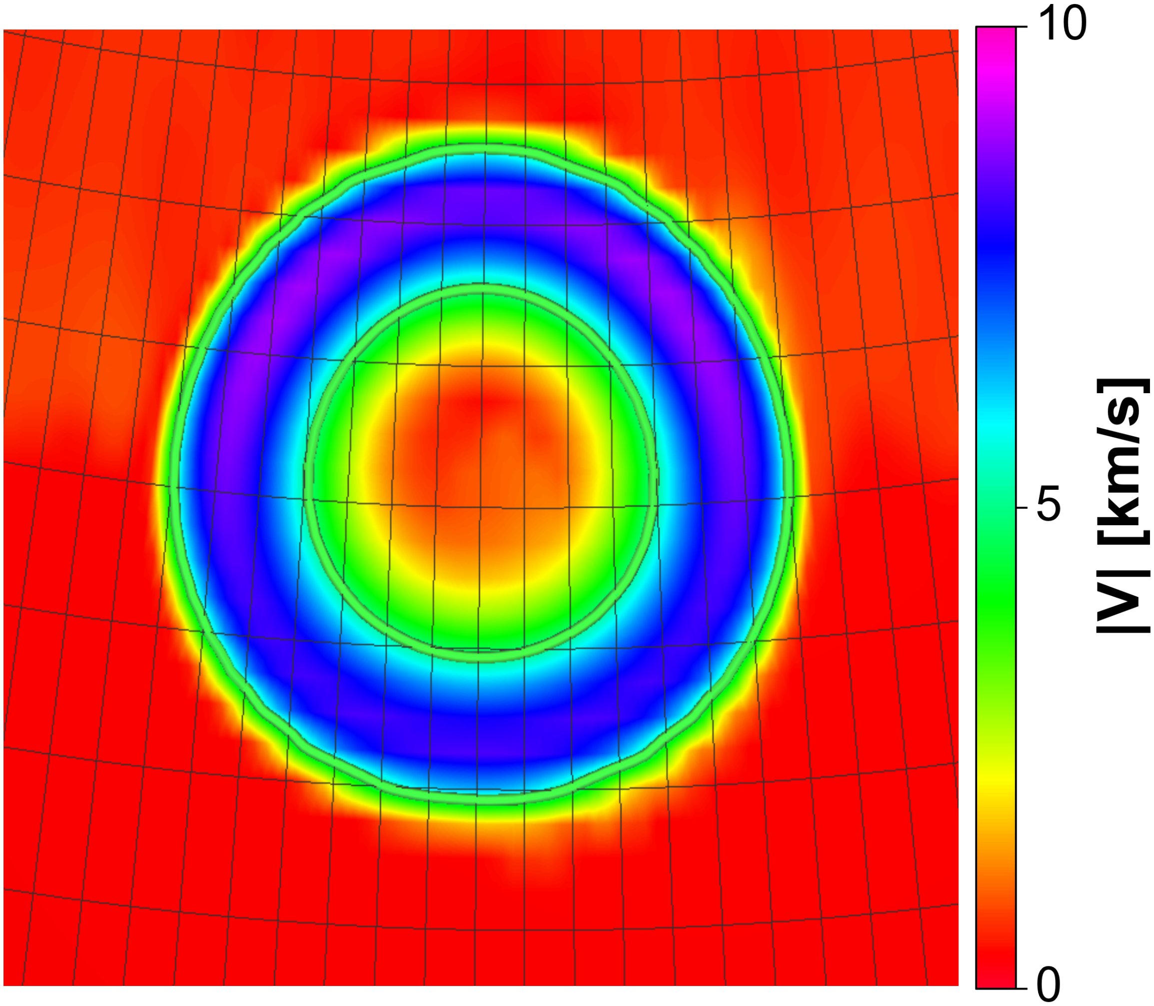

Figure 2.2: Zoom-in on the bottom radial boundary ($R = 1R_\odot$) showing tangential velocity magnitude at the peak of the driving in color shading. The green contours match the annuli shown in Figure 2.1. Block boundaries (thin black lines) also are shown.

We adopt the larger size in order to highly resolve the flow on our grid. The cell is centered at 54.5° above the equator on the coronal-hole boundary and at 0° longitude. The flow extends from 50.4° to 58.6°, for a total width of 8.2° in latitude. In longitude, it extends from $-7°$ to $+7°$, for a total width of 14° in longitude. The parameter V_0 in Equation A.6 is chosen so that the maximum flow speed is 9.1 km s^{-1}. We ramp the flow up from zero to this maximum speed, drive it steadily, and then ramp it back down to zero. The maximum speed, 9.1 km s^{-1}, is only 3% of the simulated Alfvén speed on the surface, which is of the same order of magnitude as for the Sun. By placing this flow so that it straddles the coronal-hole boundary, we displace both open and closed magnetic flux from their original equilibrium positions, just as the supergranular flows must distort coronal-hole boundaries on the Sun.

To gain physical insight into the open-closed dynamics, we simulated two cases that are presented below. On the Sun, both the southern and northern coronal-hole boundaries are driven continuously by random, out-of-phase motions. Our goal, however, is to understand in detail the fundamental dynamics of the boundary. Consequently, we designed the simulations so as to isolate the basic effect of the driving with minimal extraneous complexity. As will be evident below, even the simplest driver results in highly complex dynamics. In both cases, we displaced the coronal-hole boundary only in the northern hemisphere, using the flow pattern described above. In the first case, we twisted the field-line foot points through a maximum angle of $\pi/2$, i.e. a quarter rotation. The ramp-up and ramp-down of the driving lasted for 2.4 h. Afterwards, all tangential velocities on the surface were again set to zero, and the system was allowed to relax. This relaxation phase extended to $t = 30.3$ h, where $t = 0$ h marks the start time of the driving. This finite, but not extreme, distortion of the boundary allows us to examine in detail how the system evolves. Then, in the second case, to better simulate the complexity resulting from constant photospheric driving, we twisted the foot points through a maximum angle of 2π, i.e. a full rotation. This motion results in a very complex distortion of the initial boundary, more like the actual supergranular flow is expected to produce. The driving phase lasts 6.0 h, and the relaxation extends to $t = 75.6$ h. Below, we present the results of these two simulations.

2.4 Results

2.4.1 $\pi/2$ Displacement

Figures 2.3 and 2.4 show the shape of the coronal-hole boundary for the $\pi/2$ rotation at various times during the evolution. Here we show snapshots before driving at $t = -0.03$ h, immediately after driving at $t = 2.4$ h, and then at three additional times chosen to best illustrate the phases of evolution, at times $t = 11.6$ h, $t = 21.0$ h, and $t = 30.3$ h. (We strongly encourage the reader to watch the full, 5-minute-cadence movies that are available in Appendix B.) At each time, the coronal-hole boundary is shown in both the northern (left) and southern (right) hemispheres. Only the northern boundary is driven by the rotational flow. In these plots, white represents open magnetic field and black represents closed. The closed field in the north always connects to the closed field in the south.

To distinguish open and closed field, we traced a 1000×1818 grid of magnetic field lines distributed over $+35°$ to $+75°$ latitude and $-20°$ to $+20°$ longitude in the north, and $-75°$ to $-35°$ latitude and $-20°$ to $+20°$ longitude in the south. Open field is defined as those field lines that reach past $12R_\odot$, where the solar-wind speed becomes greater than the Alfvén speed. At this point, information cannot propagate back to the Sun. Even if a field line "closes" beyond $12R_\odot$, its apex inevitably will be convected outward by the solar wind to the outer domain boundary. Therefore, closed field is defined as those field lines with both foot points at $1R_\odot$ and an apex that does not reach $12R_\odot$.

As is evident in the top panels of Figure 2.3, the boundary before driving is undisturbed and straight in both the north and south, except for some small irregularities due to the solar wind and the dynamic state of the top of the helmet streamer. In the middle panels of Figure 2.3, the northern boundary has been twisted by the flow (see §2.3.2) by $\pi/2$, whereas the southern boundary, which was not driven, remains undisturbed from its initial state. By simply viewing Figure 2.3, we can conclude that the horizontal, nearly straight open-closed boundary of the top panel has been rotated by approximately $\pi/2$ in the middle

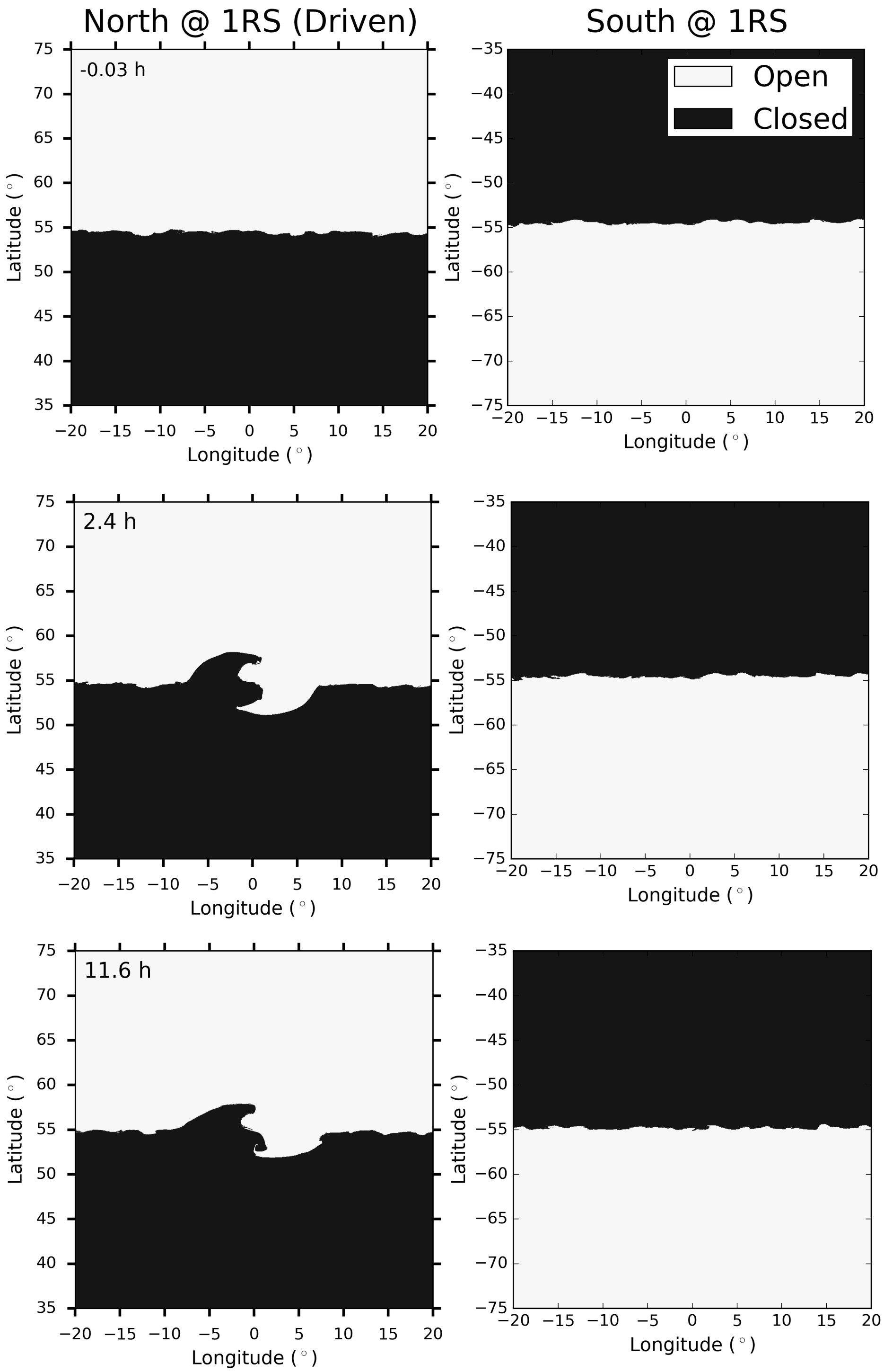

Figure 2.3: Coronal-hole boundary maps for a peak displacement of $\pi/2$, in the north (left) and south (right). White is open magnetic field, and black is closed. Top: Before driving, at $t = -0.03$ h. Middle: End of driving, at $t = 2.4$ h. Bottom: At $t = 11.6$ h. The full, 5-minute-cadence movie is available in Appendix B.

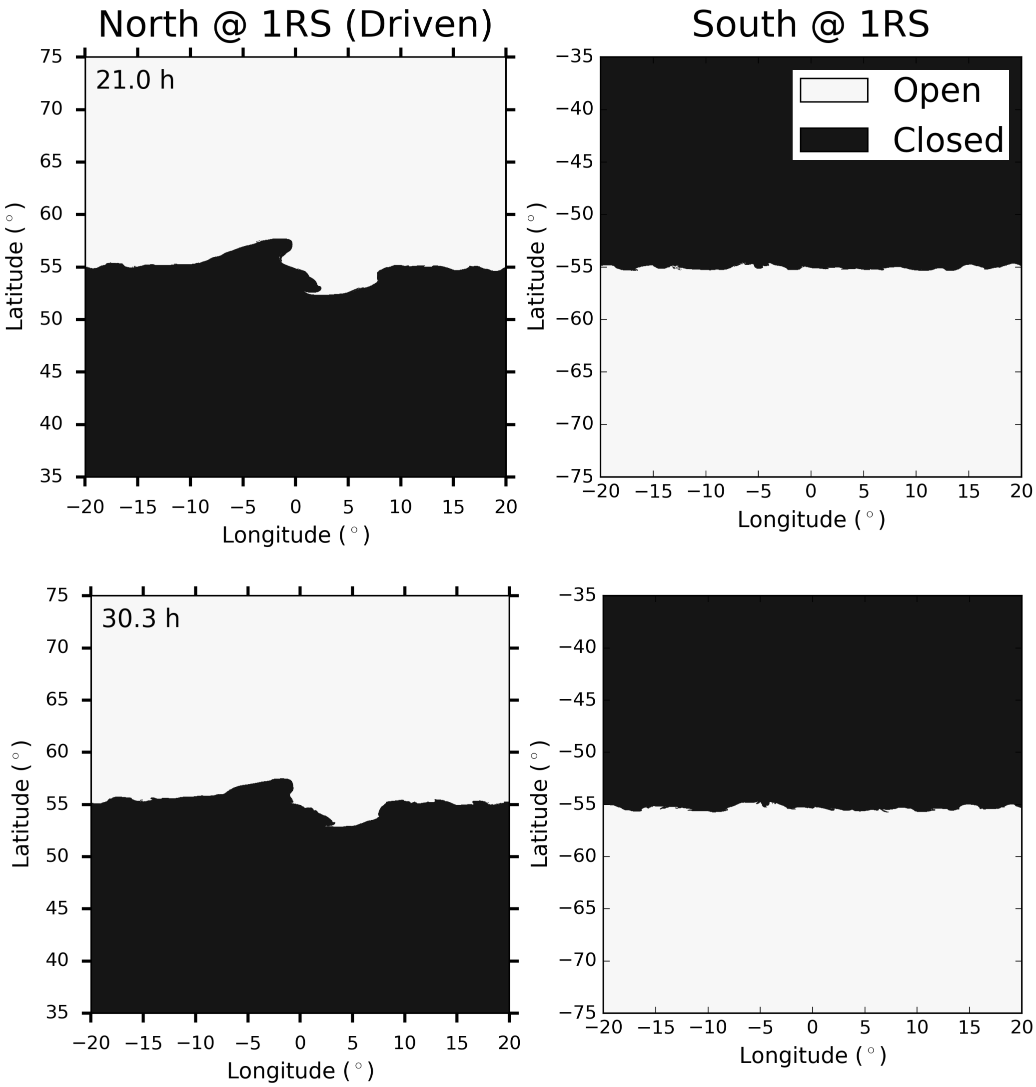

Figure 2.4: Continuation of Figure 2.3. Top: At t = 21.0 h. Bottom: At t = 30.3 h. The full, 5-minute-cadence movie is available in Appendix B.

panel. Moreover, the open-closed boundary appears to have undergone almost no relaxation during the 2.4 h of driving: it simply advects ideally with the photospheric flow. This is a key result with important implications for understanding the open-closed dynamics. The imposed photospheric flows produce a substantial deformation of the northern open-closed separatrix surface very early in the driving, and launch nonlinear Alfvén waves in both the open and closed fluxes. In principle, this could lead to the formation of current sheets and interchange reconnection along the separatrix or open-open reconnection once the wave reaches the HCS above the closed flux. However, we do not see any evidence for such reconnection. The southern coronal-hole boundary appears unchanged between the top and middle panels.

It appears, therefore, that a significant relaxation requires the buildup of a substantial deformation of the closed flux. This result validates our arguments above that only long-time-scale photospheric motions, such as supergranular flows, are important for driving the open-closed dynamics. For the parameters of our system, the typical length of the last closed field line is $\sim 10^6$ km, whereas the average Alfvén speed along this flux is ~ 100 km s^{-1}, so the Alfvén travel time is of order a few hours, longer than the 2.4 h driving time. Consistent with this estimate is the result that, in the simulation, electric currents due to the driving appear at the southern foot points of the rotated flux 3 h after the start of the driving. We expect, therefore, that the time scale for the decay of the boundary deformation will be, at least, 3 h. Any driving on time scales much shorter than this, such as granules or the magnetic carpet, will only add high-frequency noise to the coronal-hole boundary.

Figures 2.3 and 2.4 show this slow decay in detail. Because we do not allow slipping on the photospheric surface after the driving has ended, any change in the coronal-hole boundary is due to 1) opening of closed field, 2) closing of open field, or 3) interchange reconnection between the two. Opening of magnetic field lines would register as black changing to white in Figures 2.3 and 2.4, and corresponds to a closed field line rising up and moving past $R = 12R_{\odot}$. Closing of magnetic field lines would register as white changing to black, and corresponds to two open field lines reconnecting to form a closed field line and a u-loop disconnected field line, which would move with the solar wind and leave through the outer boundary at 30 $R_\odot$. Finally, interchange reconnection would register as either a black-to-white or white-to-black switch,foot points and occurs when one open and one closed field line reconnect and switch foot points. Such an interaction results in the same amount of open and closed flux, but changes the connectivity of the system, allowing material that was trapped on the closed field line to move outwards into the solar wind. Note that the connectivity shown in all of these plots is instantaneous: any opening of a closed field line shown in the north would also appear immediately as opening in the south.

The bottom panel of Figure 2.3 shows the coronal-hole boundaries at $t = 11.6$ h. By this time, the closed field has had sufficient time to deform substantially in response to the applied photospheric stress. The open-closed boundary in the north shows clear signs of activity, with an intrusion of open field cutting into the closed field near the location of the center of the flow. Sharp structure has also appeared on the boundary near the edge of the displaced region around 8° longitude. The southern boundary, in contrast, remains smooth with no discernible changes.

The top panels of Figure 2.4 show the system at $t = 21.0$ h. At this time, the Alfvén wave on the open field lines has left the system through the outer boundary at $30R_\odot$. The coronal-hole boundary has smoothed out somewhat and is beginning to show clear counter-rotation back towards its initial state. The bottom panels of Figure 2.4 show time $t = 30.3$ h, where the southern boundary remains largely unchanged. There is a small distortion near $-5°$ longitude due to the formation of a blob at the top of the helmet streamer. The coronal-hole boundary in the north, on the other hand, has continued to evolve, counter-rotating back towards its initial, smooth configuration.

The question now becomes: how is the previously displaced open magnetic field becoming closed again, and the displaced closed field becoming open? Any true opening or closing of the magnetic field would produce a signature in the south, yet the southern boundary remains largely unaltered. We must conclude, therefore, that interchange reconnection is responsible for the change in the northern boundary.

Figure 2.5 shows the amount of interchange reconnection experienced by the field lines traced in Figures 2.3 and 2.4 in the northern (red) and southern (blue) hemispheres, along with the amount of flux closing down (yellow) and opening up (green). Of course, the amounts of opening and closing are identical in the two hemispheres, but the interchange can be very different. Figure 2.5 begins at the end of the driving phase; consequently, any change in connectivity must be due to opening, closing, or reconnection. There is a continual, small, but measurable amount of closing throughout the simulation. This is due to an overall continual closing experienced by the system as it relaxes gradually from its initial PFSS state toward a steady configuration supported by the solar wind. In addition, a quasi-steady amount of interchange reconnection takes place in both hemispheres. This is due to the persistent restructuring of the HCS as it distends, then reconnects and retracts while releasing blobs, and at last resumes its outward distention. Over and above these two processes, a transient enhancement of interchange reconnection occurs principally in the northern hemisphere, where the rate reaches a maximum about 3 h after the end of the driving phase. This is consistent with our argument above that the relaxation is driven by the deformation of the closed flux and, hence, reflects its intrinsic time scale. The decay time for this interchange is also of order a few hours. There appears to be a rise in interchange reconnection in the south, as well, but this is far less clear than in the north. It may well be that the deformation of the closed flux drives interchange at foot points that were not driven by the flow.

Our result that interchange reconnection is the dominant relaxation process clarifies why a substantial deformation of the closed flux must build up in order for the relaxation to occur. Interchange reconnection cannot occur if the top of the helmet streamer maintains its classic 2D geometry, with a simple Y-type null and a current sheet only above the closed flux. This region must become strongly 3D, with current sheets forming between open and

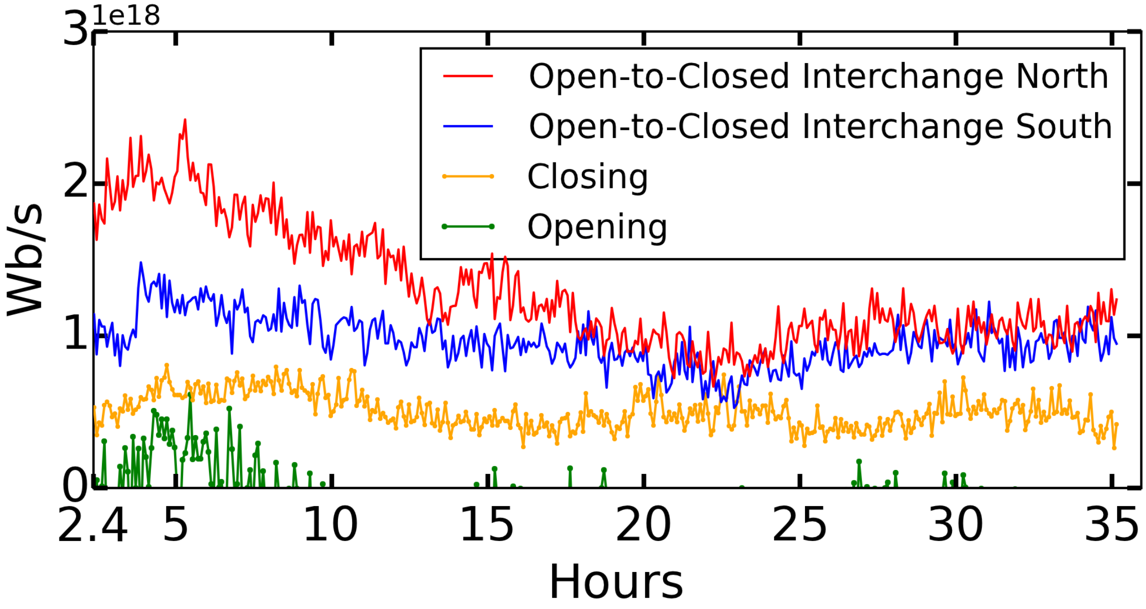

Figure 2.5: Rate of flux change for a peak displacement of $\pi/2$, where time $t = 2.4$ h corresponds to the end of the driving. Red and blue curves display the rate of flux change due to interchange reconnection in the north and south, respectively; yellow and green curves display the rate of flux change due to closing and opening, respectively. The rates of opening and closing are identical in the north and south.

closed flux (*Wang et al.*, 2000). Since any stress on the open flux will simply propagate away, it must be the deformation of the closed flux that leads to the current sheets and the ensuing interchange reconnection. A somewhat surprising result is the clear lack of significant field-line opening during the relaxation. There is some weak opening before and during the driving, but this is negligible. A seemingly obvious evolution for relaxing the field would be to open all the stressed closed flux and then simply close down all the flux that is not open in the original, pre-driven configuration. This would return the system back to its minimum-energy state. In spite of its effectiveness, however, we see no evidence for such evolution. A possible explanation is that closed field lines do expand outward and attempt to open, but then encounter open flux and interchange reconnect before reaching $12R_\odot$. In any case, our simulation clearly shows that a localized deformation of the open-closed boundary relaxes almost exclusively via interchange reconnection.

To better understand how interchange is able to produce a global relaxation of the boundary back toward its original shape, we track where the interchange is occurring. Figure 2.6 shows the instantaneous change in connectivity on the left, and the accumulated change in connectivity on the right at the final time, $t = 30.3$ h. (The full movie is available in Appendix B.) The plot on the left showing the instantaneous change is a binary plot, where field lines that changed either from closed to open or from open to closed between the current and previous times are represented by red circles. The right panel shows how many times each field line changed connectivity throughout the simulation, where only field lines that have interchanged twice or more are shown. This means that any change in connectivity due to closing or opening in the overall PFSS relaxation would not be shown.

The movie in Appendix B shows that, just as in the final frame shown here, there are changes in connectivity all along the coronal-hole boundary from $-20°$ to $+20°$ longitude, even though only the region within $\pm 7°$ was displaced. From the right panel in Figure 2.6, we can see that many field lines on the boundary interchange more than 5 times, while some field lines in the region near the center of the photospheric rotation interchange over 50

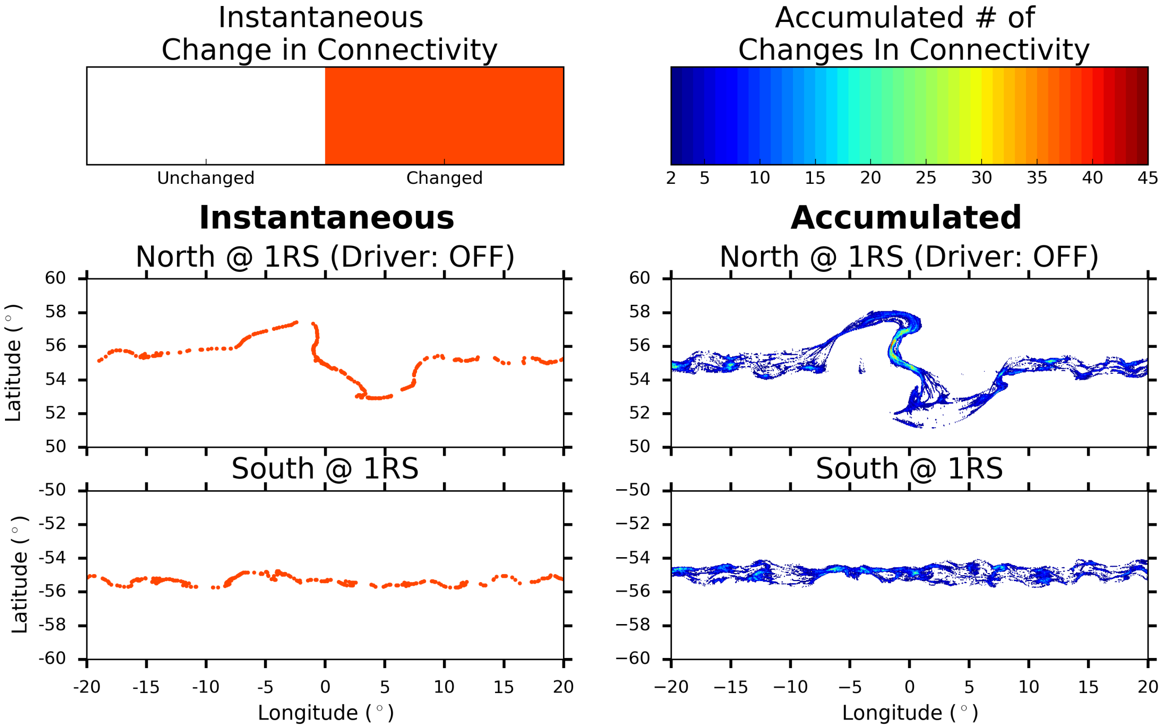

Figure 2.6: Left: Instantaneous change in connectivity for a peak displacement of $\pi/2$, in the north (top) and south (bottom). Red circles indicate the locations of field lines that have changed their connectivity between the previous and current snapshot. Shown here are the final maps at t = 30.3 h. Right: Contour plot of the number of times each field line has changed connectivity over the entire duration of the simulation, in the north (top) and south (bottom). Field lines that have changed connectivity only once are not shown. The full, 5-minute-cadence movie is available in Appendix B.

times. This result indicates that interchange reconnection must be the natural response to foot point stressing, and that it must be common in the solar corona and wind.

We find that, through this interchange process occurring everywhere along the boundary, locations far from the driven region are permanently changed. Figures 2.7 and 2.8 show the same closed field lines as displayed previously, except that here the field lines are colored by the locations of their southern foot points. Field lines with foot points between $-20°$ and $-10°$ longitude in the south are colored navy blue, those between $-10°$ and $0°$ are teal, those between $0°$ and $+10°$ are red, and those between $+10°$ and $+20°$ are yellow. In the initial field, these also correspond to the location of the northern foot points, since the field was potential with an axisymmetric mapping from south to north. Figures 2.7 and 2.8 allow us to observe clearly the change in the global mapping introduced by both the driver and the interchange reconnection. The top, middle, and bottom panels of Figure 2.7 display the boundary at $t = -0.03$ h before the driving, $t = 2.4$ h immediately after the driving, and $t = 7.0$ h, respectively. Figure 2.8 shows the late-time maps at $t = 16.3$ h and $t = 30.3$ h.

Our driver displaces field lines between $\pm 7°$ longitude (compare the top and middle panels of Figure 2.7). However, we see in the other three panels of Figures 2.7 and 2.8 that field outside of this region is affected. In the bottom panel of Figure 2.7, the boundaries at $\pm 10°$ have already begun to change, and still larger changes are evident in Figure 2.8. Most importantly, we see in the bottom panel of 2.8 that the closed, teal-shaded flux that was the most displaced between $-5°$ and $0°$ has migrated down and pushed out the closed-field boundary between $-13°$ and $-7°$. We also see that yellow flux from beyond $+10°$ has been displaced into the initially red region, even though this flux was not driven.

It is evident by comparing the first panel of Figure 2.7 to the last one in Figure 2.8 that the system cannot return back to its original state, even if allowed to relax indefinitely. Figure 2.5 shows that the amount of reconnection occurring at the end of the simulation has leveled off. Consequently, we conclude that by $t = 30.3$ h the system has reached a new quasi-steady state. This state differs from the original primarily in the presence of twist deep within the

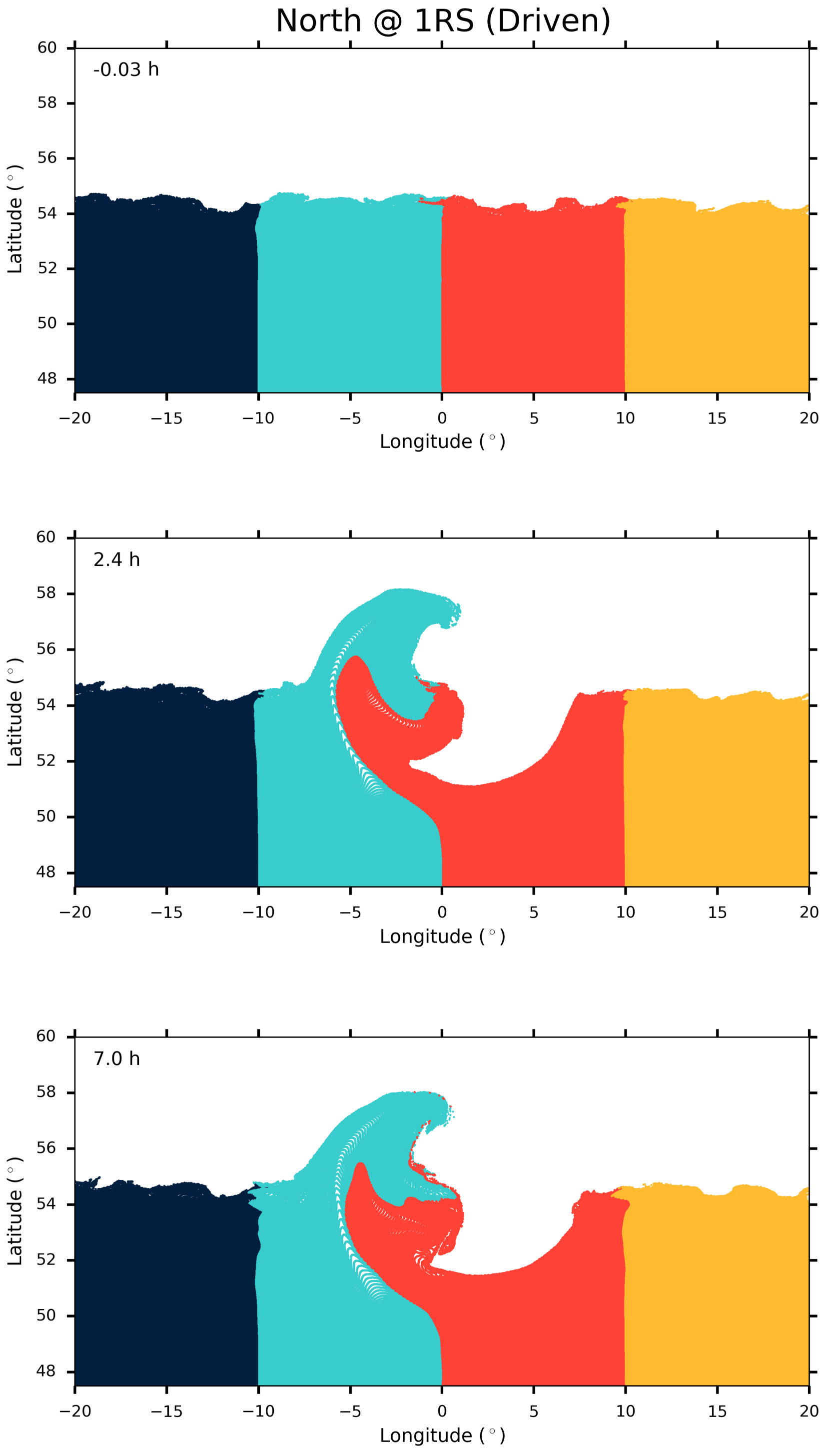

Figure 2.7: Closed field lines in the north for a peak displacement of $\pi/2$. Field lines are color-shaded based on the longitudes of their conjugate foot points in the southern hemisphere: navy blue between $-20°$ and $-10°$; teal between $-10°$ and $0°$; red between $0°$ and $+10°$; and yellow between $+10°$ and $+20°$. Top: Before driving at $t = -0.03$ h. Middle: End of driving at $t = 2.4$ h. Bottom: At $t = 7.0$ h. The full, 5-minute-cadence movie is available in Appendix B.

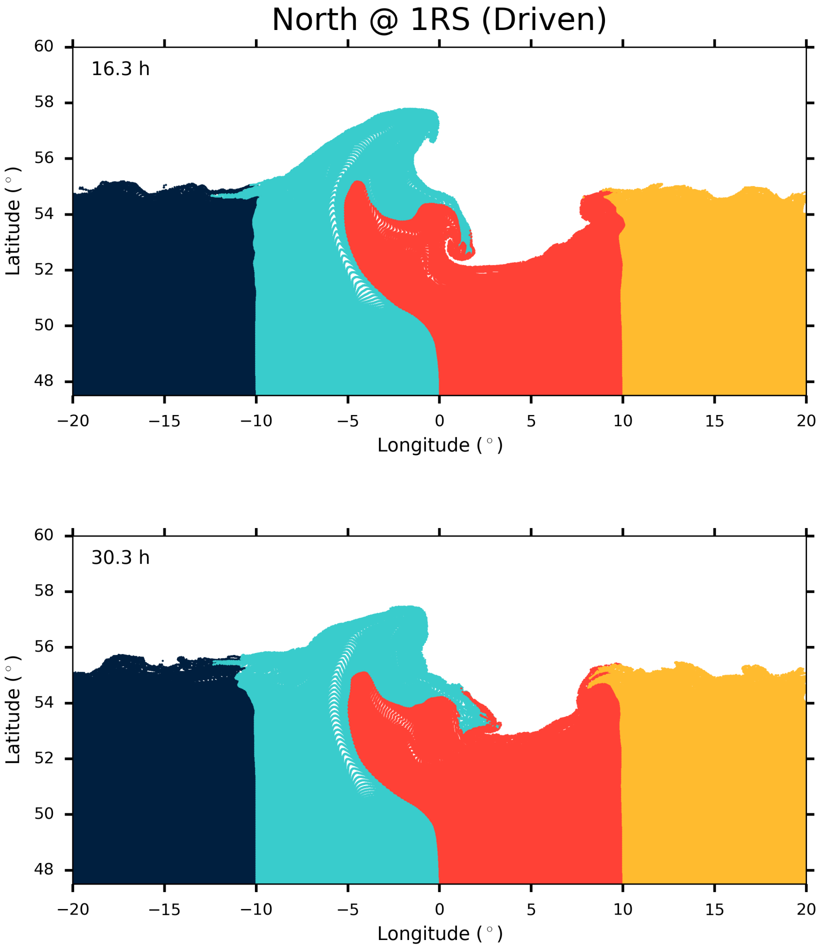

Figure 2.8: Continuation of Figure 2.7, using the same color scheme. Top: At t = 16.3 h. Bottom: At t = 30.3 h. The full, 5-minute-cadence movie is available in Appendix B.

closed-field region. Since this twist is large-scale and far from the open-closed boundary, it does not produce any current sheets and cannot relax via reconnection. Even if reconnection could easily occur in the closed region, it could not return the field to its original, unstressed state, due to helicity conservation (e.g. *Taylor*, 1974, 1986; *Antiochos*, 2013). Of course, on the Sun a coronal-hole boundary never relaxes to some unperturbed state, because it is being driven continuously by the random supergranular flows. The key conclusion from the results presented here is that the time scale for full relaxation via interchange reconnection is of order 10 h or so, which is comparable to the driving time. Therefore, solar coronal-hole boundaries are never quasi-steady, but are strongly dynamic.

2.4.2 2π Displacement

In order to determine the coronal-hole boundary dynamics for a strong, continuous driver, we performed and analyzed a simulation with a full 2π rotation, corresponding to the complete lifetime of a supergranule. We kept the maximum velocity the same as in the $\pi/2$ case and drove the system at this steady rate for a longer duration, in order to reach the specified displacement. Because the top of the helmet streamer becomes much more distorted in this case, the results presented below exhibit much more drastic dynamics than those above. On the Sun, convective cells appear and disappear randomly on the photosphere continuously. The results presented below, therefore, still represent a great simplification from the true complexity of solar coronal-hole boundary dynamics.

Figures 2.9 and 2.10 show the coronal-hole boundary throughout the rotation. As in Figures 2.3 and 2.4, open field is represented by white and closed field by black, with the northern hemisphere shown on the left and the southern on the right. The top panels of Figure 2.9 show the boundaries before onset of driving at $t = -0.03$ h, and the middle panels show the boundaries immediately after the driving has ceased at $t = 6.0$ h. The grid has sufficiently resolved one complete rotation of the coronal-hole boundary. While the boundary is strongly twisted in the north, there have been no changes to the southern boundary even though there has been sufficient time for the stress to propagate to the southern foot points. Note that the full 2π rotation induces an extreme deformation of the boundary, yielding much more fine structure than the $\pi/2$ case above. This is the reason for first analyzing and gaining insight from the case with a small rotation. Observe also that the structure of the boundary at $t = 6.0$ h is not due solely to ideal convection. There must have been considerable reconnection to form the detailed small-scale structure visible at the end of the driving phase. This is to be expected, given our finding above that the time scale for relaxation is 3 h or so.

In light of this fine-scale structuring, it may seem surprising that even with the extreme deformation of the northern boundary, there is no observable effect on the southern. One reason for this result is that, on the time scale of 6 h, any change in the south could be due only to interchange or closing. As noted previously, we define a field line to be open if it intersects the $R = 12R_\odot$ surface. Since it takes approximately 12 h or so in our simulation for a disturbance, whether mass flow or Alfvén wave, to propagate out to this surface, no opening can occur until later. The closing of field lines could, in principle, occur on the time scale of 6 h, but this is unlikely given that the addition of large magnetic stress into the corona should result in a net opening of flux rather than closing. Furthermore, it is unlikely that a large amount of interchange would occur in the south, because this would only deform the boundary away from its initial quasi-steady position.

The bottom panels of Figure 2.9 show the boundary at $t = 15.9$ h, while Figure 2.10 shows the boundaries at $t = 30.9$ h, $t = 50.9$ h, and $t = 75.6$ h. These frames were chosen to best illustrate the phases of evolution. At early times, comparing $t = 6.0$ h and $t = 15.9$ h, we observe rapid evolution in the regions that are displaced the most. The movie available in Appendix B shows the development and decay of fine-scale structure at the northern boundary throughout this process, just as in the $\pi/2$ case. Notice, however, that the evolution sometimes demonstrates the development of very fine corridors of both open and closed flux, but these corridors eventually disappear. The southern boundary, in

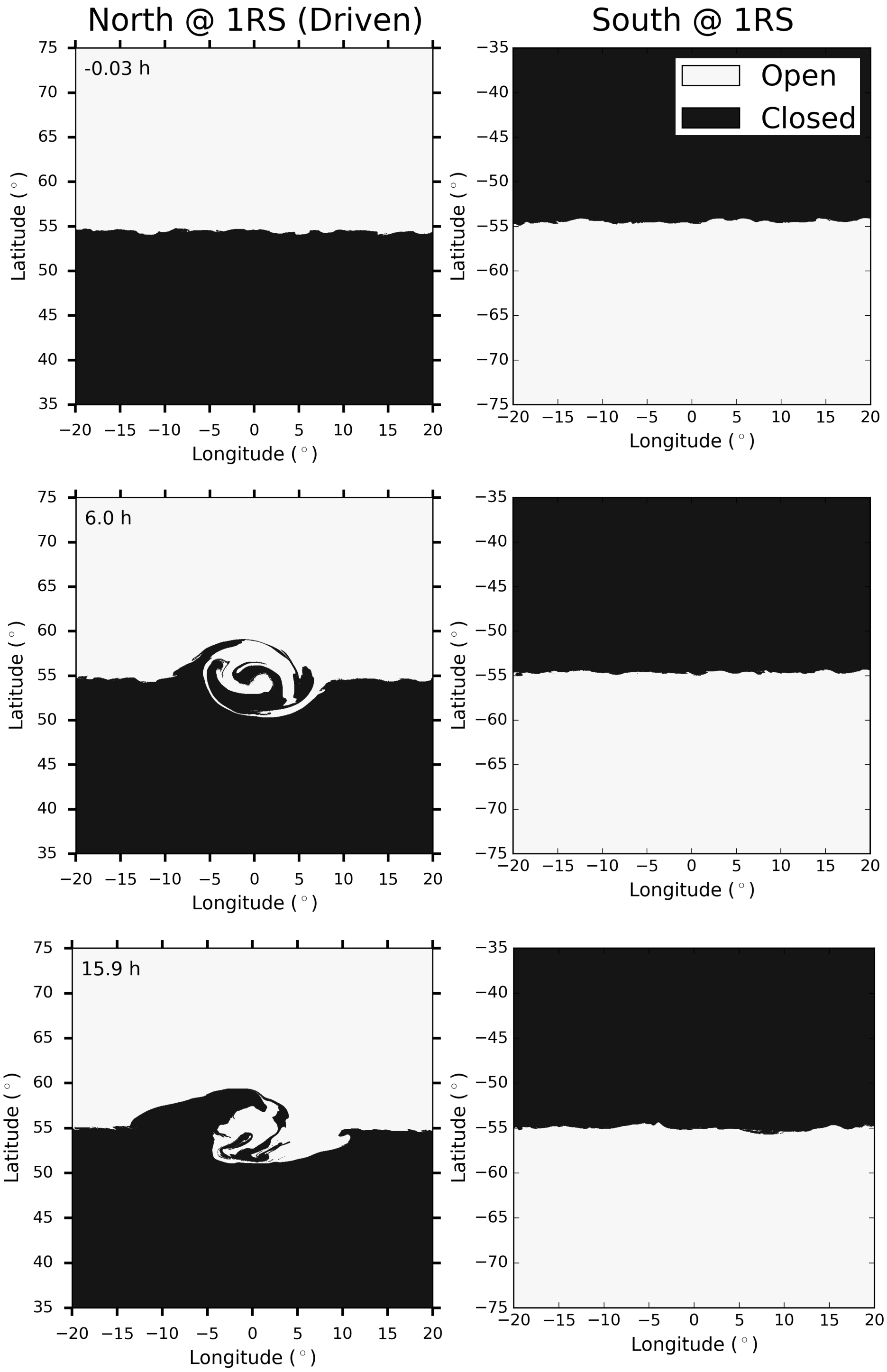

Figure 2.9: Coronal-hole boundary maps for a peak displacement of 2π, in the north (left) and south (right). White is open magnetic field, and black is closed. Top: Before driving, at $t = -0.03$ h. Middle: End of driving, at $t = 6.0$ h. Bottom: At $t = 15.9$ h. The full, 5-minute-cadence movie is available in Appendix B.

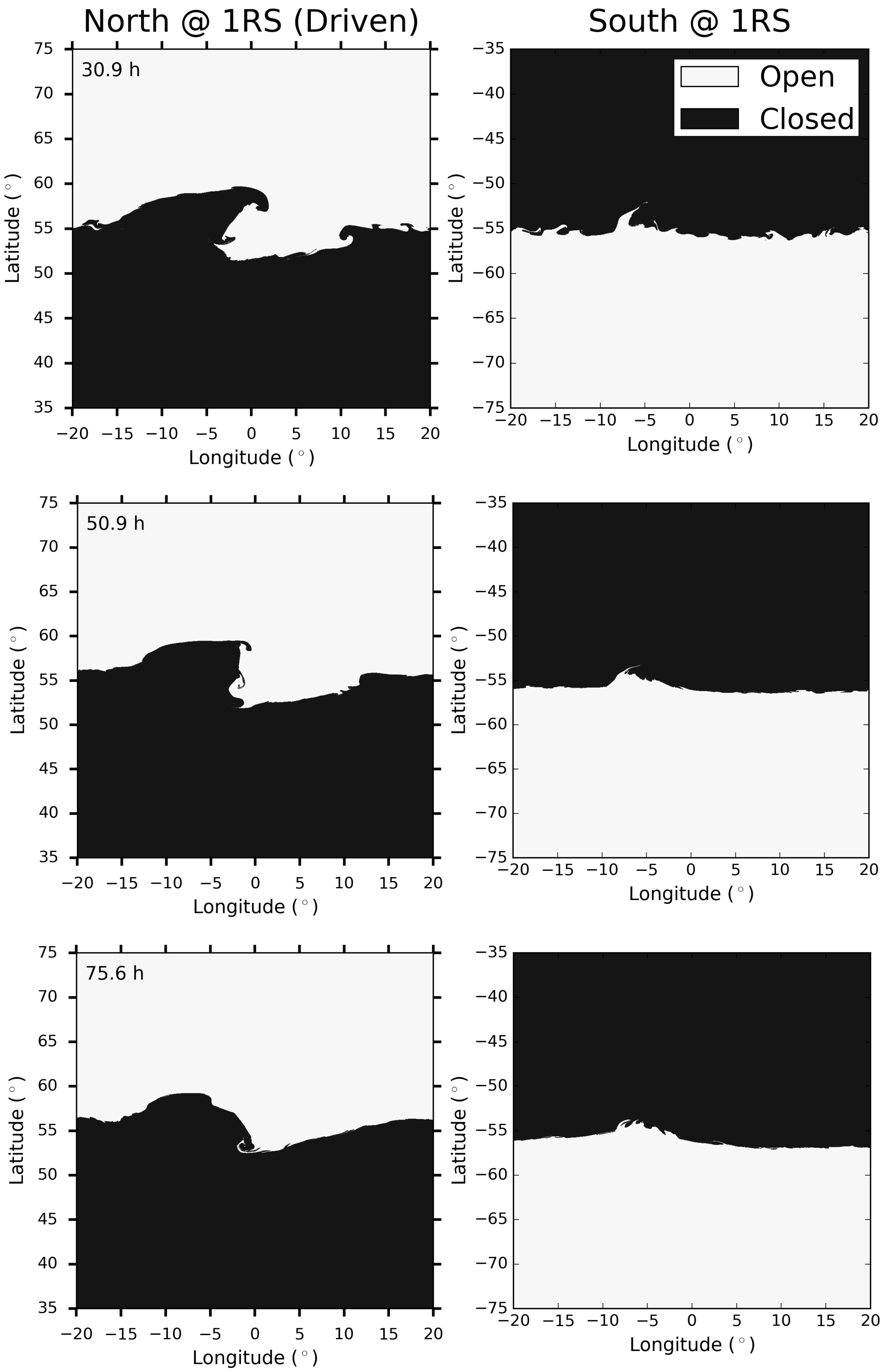

Figure 2.10: Continuation of Figure 2.9. Top: At $t = 30.9$ h. Middle: At $t = 50.9$ h. Bottom: At $t = 75.6$ h. The full, 5-minute-cadence movie is available in Appendix B.

contrast, remains unchanged during this time, despite the extreme dynamics in the north. By $t = 30.9$ h (top panels of Figure 2.10), the changes in the north have slowed as the finest-scale structure has been interchanged away. We continue to see slow changes in the northern hemisphere along the lines of the behavior of the $\pi/2$ case. However, now the southern boundary has begun to show changes. Note in particular the spike-like indentation of open flux into the southern closed-field region. This feature could be due to opening of flux that has reached the 12 $R_\odot$ surface, but we will show below that it is due to interchange. Additionally, we see a distinct corrugation of both the northern and southern boundaries. This is due to localized opening or closing of flux, which occurs on a smaller scale even without the driving, but here it is enhanced by the induced stresses. The corrugation disappears over the next 10 h or so. By the end of the simulation, which is nearly three days after the driving has stopped, the northern coronal-hole boundary has nearly, but not quite, returned to its initial state. The only significant change in the south, meanwhile, is that the spike of open flux has broadened into a smooth indentation, indicating that there has been a localized opening due to the stress that now resides permanently in the closed-field region.

Figure 2.11 shows the amount of interchange reconnection, closing, and opening that these field lines experience after the end of the driving, just as in Figure 2.5. As before, the red and blue curves indicate interchange reconnection in the north and south, and the yellow and green curves show the amount of closing and opening, respectively. Before the onset of driving, the amounts of interchange reconnection in the north and south match those found in the $\pi/2$ case. As the driving ceases, however, the interchange in the north increases rapidly, reaching a maximum rate approximately 3 h after the end of the driving. This time scale is the same as found in the $\pi/2$ case, but the amplitude is 6 times larger here for the larger displacement. As before, for this case also there is no noticeable increase in the interchange rate in the south, at least on the scale of the figure.

The interchange in the south subsequently does show a broad rise and attains a maximum, but only about 20 h after the end of the driving. In fact, the interchange rate in the south

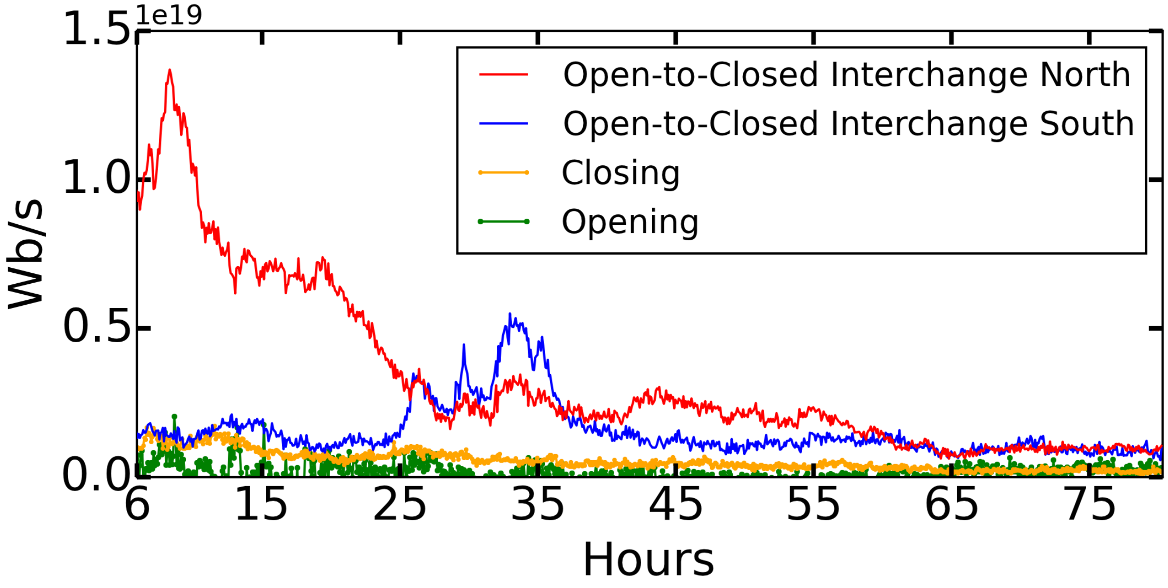

Figure 2.11: Rate of flux change for a peak displacement of 2π, where time $t = 6.0$ h corresponds to the end of the driving. Red and blue curves display the rate of flux change due to interchange reconnection in the north and south, respectively; yellow and green curves display the rate of flux change due to closing and opening, respectively. The rates of opening and closing are identical in the north and south.

surpasses that in the north during this period. Notice that after about 40 h or so, the interchange in the north again rises and eventually surpasses that in the south. It appears that there is a global oscillation in the interaction between open and closed flux during this relaxation. The stress in the closed field propagates quickly, at the Alfvén speed, and for a force-free field should equilibrate along field lines. We expect, therefore, that after 10 h or so, the closed flux should reach an equilibrium. At first, this equilibrium produces current sheets in the open flux only in the north, which has been deformed by the flow. The relaxation in the north by interchange is sufficiently fast, however, that eventually it throws the south out of balance. The south then begins to interchange rapidly as well, and surpasses that occurring in the north. This exchange occurs once more before the two rates decline to become almost identical by $t = 65$ h. Although interesting, this oscillation is not relevant to the Sun, where both the northern and southern boundaries would be driven simultaneously and continuously.

Figure 2.12 is the final frame of the available in Appendix B movie, which shows the instantaneous and accumulated changes in connectivity due principally to interchange reconnection. The left side shows that, as before, interchange reconnection is occurring along the entire coronal-hole boundary. The right shows that hot spots of connectivity changes exist in regions with the most structure, and that individual field lines interchange over 50 times, as observed earlier. Note that even in the south, where there is no photospheric driving, some locations show numerous interchanges taking place.

The long-term effect of this large amount of interchange on its surroundings is shown in Figures 2.13 and 2.14, in the same style as Figures 2.7 and 2.8. Closed field lines again are grouped into four regions, based on the locations of their southern foot points. The top panel of Figure 2.13 shows the corona-hole boundary and closed-field region before driving at $t = -0.03$ h, the middle immediately after driving at $t = 6.0$ h, and the bottom at $t = 15.9$ h. Figure 2.14 shows late-time snapshots at $t = 30.9$ h and $t = 75.6$ h. (The full movie is available in Appendix B.)

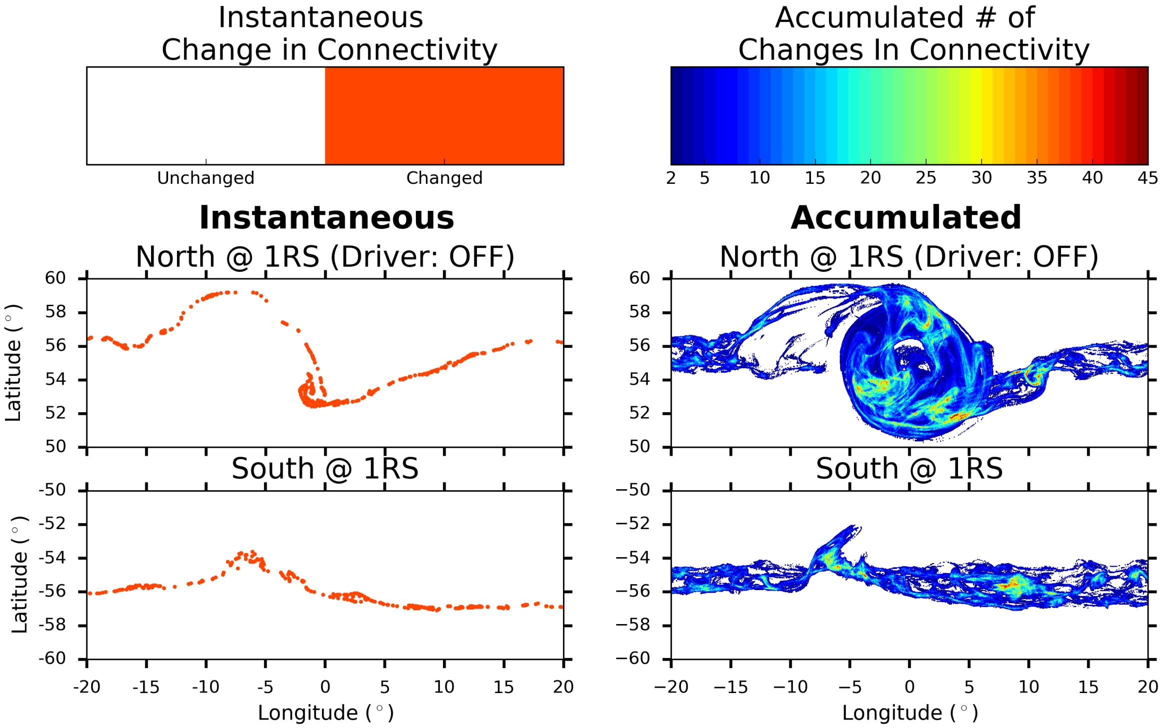

Figure 2.12: Left: Instantaneous change in connectivity for a peak displacement of 2π, in the north (top) and south (bottom). Red circles indicate the locations of field lines that have changed their connectivity between the previous and current snapshot. Shown here are the final maps at $t = 75.6$ h. Right: Contour plot of the number of times each field line has changed connectivity over the entire duration of the simulation, in the north (top) and south (bottom). Field lines that have changed connectivity only once are not shown. The full, 5-minute-cadence movie is available in Appendix B.

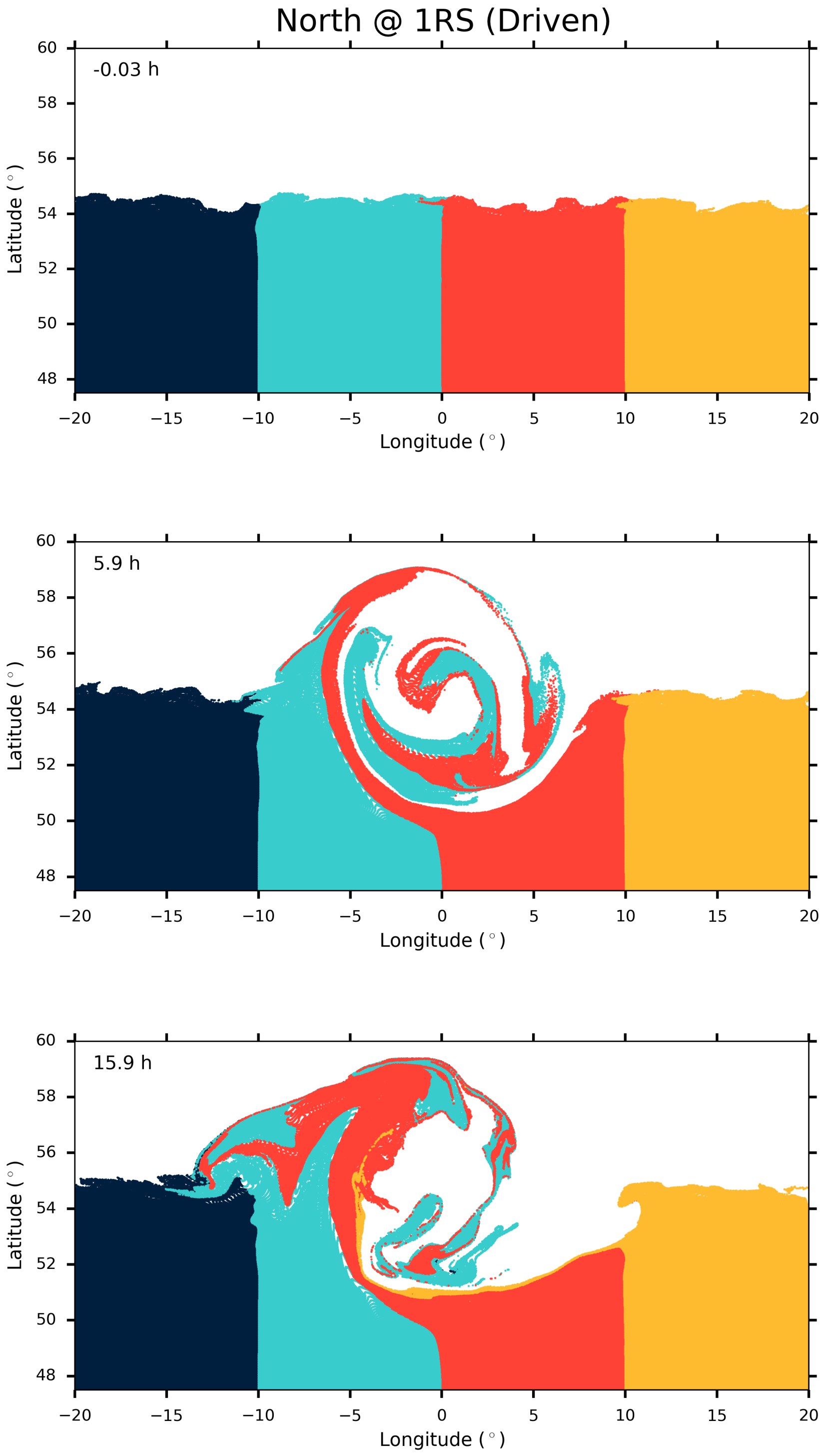

Figure 2.13: Closed field lines in the north for a peak displacement of 2π. Field lines are color-shaded based on the longitudes of their conjugate foot points in the southern hemisphere: navy blue between $-20°$ and $-10°$; teal between $-10°$ and $0°$; red between $0°$ and $+10°$; and yellow between $+10°$ and $+20°$. Top: Before driving at $t = -0.03$ h. Middle: End of driving at $t = 6.0$ h. Bottom: At $t = 15.9$ h. The full, 5-minute-cadence movie is available in Appendix B.

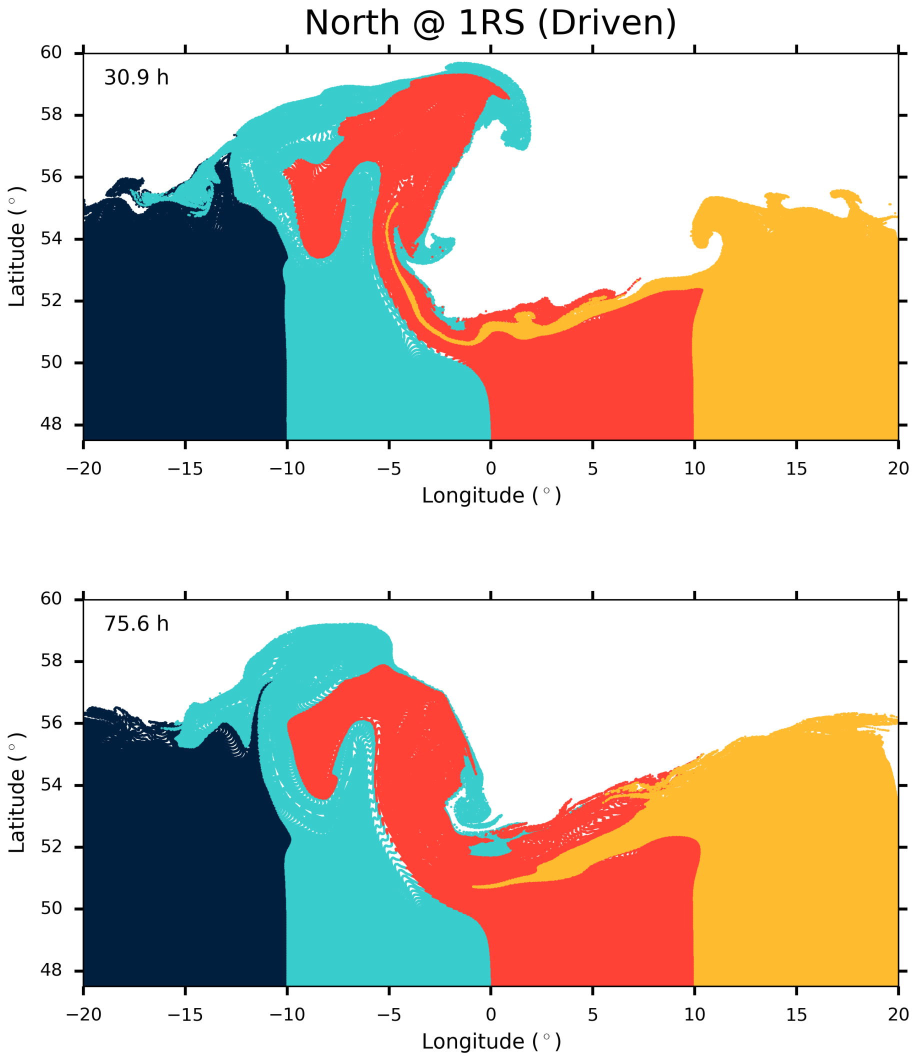

Figure 2.14: Continuation of Figure 2.13, using the same color scheme. Top: At $t = 30.9$ h. Bottom: At $t = 75.6$ h. The full, 5-minute-cadence movie is available in Appendix B.

The interchange reconnection works quickly at the beginning. At $t = 15.9$ h (bottom panel of Figure 2.13) field lines in the teal and red regions that were displaced can already be seen cascading along the boundary toward $-10°$ longitude. In the top panel of Figure 2.14, the interchange continues to push the boundary north around $-10°$ longitude. Also, a teal-shaded finger extends all of the way to $-15°$ longitude, 6° beyond the initial flow region, while field lines from the yellow-shaded region beyond $+10°$ longitude have interchanged their way along a large portion of the boundary, despite not having been driven. Notice also that there is clear evidence for reconnection within the closed-field region. A long yellow-shaded filament, which at one time extends far into the red region, retracts considerably back toward its original location. The bottom panel of Figure 2.14 at time $t = 75.6$ h, nearly three days after the end of the driving, shows that even though the boundary may appear smooth and close to its original configuration, the closed-field region remains quite far from its initial state. Of course, any such structure would not survive long on the Sun, because subsequent photospheric rotations would completely destroy it.

2.5 Discussion

The key result of our simulations is that interchange reconnection dominates the evolution of the open-closed boundary when driven by a photospheric rotation. Although some flux opening and closing does occur, it is far outweighed by interchange. As discussed above, this is somewhat unexpected, because flux opening is generally assumed to be the mechanism by which the corona sheds magnetic stress, certainly the large-scale magnetic shear evident in CMEs (e.g. *Lynch et al.*, 2016). Interchange reconnection is typically not expected to produce marked changes in coronal-hole boundaries, since interchange at any arbitrary location along a perturbed boundary is not guaranteed to help the boundary evolve back toward its lowest-energy state. In Figures 2.3 and 2.4, interchange would show up as a switching of a black and white point, so if this occurs across the boundary at the point of maximum displacement, the interchange actually could move the system farther from its preferred state. Instead, the tip of the displaced closed-field region interchanges with field lines along the boundary in a manner that broadens the closed-field region but smoothes the boundary. The result is displaced field lines pushing along the coronal-hole boundary in a manner that makes the zone of maximum displacement appear to be diffusing back into the closed-field region. This effect can be seen in Figure 2.8, where the teal-shaded region of field lines is pushing into the navy and red regions.

The key to understanding this evolution is that interchange reconnection usually acts to smooth out any sharp structure that forms along the boundary. We emphasize, however, that interchange does not always smooth out structure. The movies of the 2π case clearly show the transient formation of long, thin filaments of both closed and open field during the relaxation. Furthermore, the southern boundary often builds up fine-scale structure, even though this boundary was not driven. The structures due to interchange are fairly short-lived, but they do show that interchange cannot be thought of as a purely diffusive process. For the most part, however, interchange reconnection evolves the entire boundary, not just where the displacement occurs, so as to smooth out any sharp features. Our simulations show that localized photospheric driving produces a permanent change in the open-closed boundary, even far from the driven region.

A heuristic picture of the effects of interchange reconnection is shown in Figure 2.15. Panels a, b, and c show how the coronal-hole boundary (solid black line) changes with time. The closed-field region is represented by the entire solid-shaded gray, red, blue, orange, and green regions beneath the solid black line. The striped regions above the solid black line are open-field regions. Between panels a and b, interchange reconnection occurs between the closed-field region 1 and open-field region 2, and between the closed-field region 3 and open-field region 4. The pattern repeats on the left side, with like-colored regions interchanging. The new boundary that results from this interchange is shown as the yellow line in panel a and becomes the new coronal-hole boundary shown in black in panel b. The process then continues, resulting in the black coronal-hole boundary shown in panel c. The original boundary is shown in gray, over the top of the new one in black, in panel c. The overall effect is to shrink the height of the region while broadening it and preserving its area. A large fraction (though not all) of the evolution seen in our simulations is simply the cumulative effect of this process.

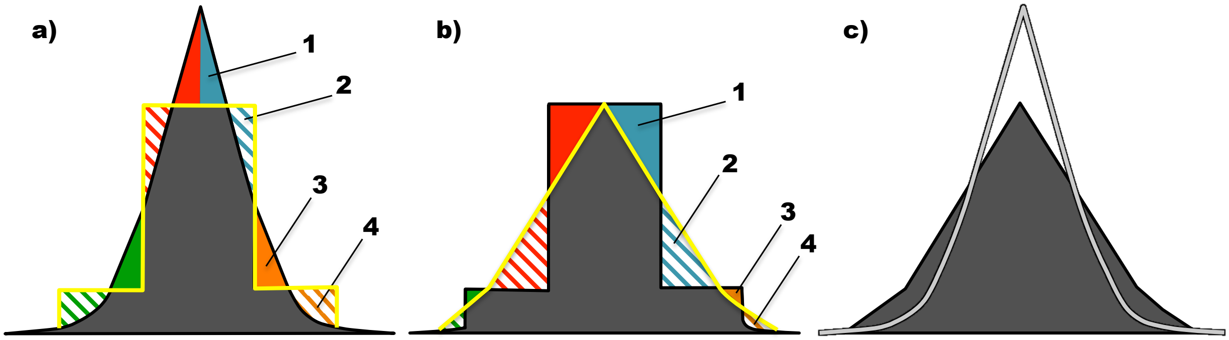

Figure 2.15: Cartoon schematic of interchange reconnection changing the boundary of a closed-field region. See text for details. Thick black lines: old coronal-hole boundary. Thick yellow line: new coronal-hole boundary. Thick gray line: original corona-hole boundary. Solid-shaded gray, red, blue, green and orange areas represent closed-field regions. Striped red, blue, green, and orange areas represent open-field regions. Panels a, b, and c illustrate the evolution over time.

Two important aspects of the evolution of our system are implied by Figure 2.15, but may not be immediately apparent. First, if we were to repeat the process shown in panels a and b on the black triangle of panel c, then a section of the closed-field region lower down along each side, which previously was open, would re-open. Some of this section could close again in a subsequent set of interchanges. This explains the result of Figure 2.9, which shows that some locations undergo numerous interchange reconnections. Second, note that the center of photospheric rotation is likely to be a location of many interchanges. The interchange process illustrated in Figure 2.15, occurring about the center of the boundary deformation for the $\pi/2$ case of Figure 2.3, would act very much like a counter-rotation of the boundary. It is especially advantageous for interchange to occur here and, thereby, to bring the system back to its original state. Figure 2.6 demonstrates that, in fact, interchange occurs around this location over 50 times in 30 h.

Figure 2.16 presents an example of interchange reconnection that occurs within our system at approximately $t = 13$ h. It shows a set of field lines drawn from fixed locations in the northern hemisphere at two different times, five minutes apart, during the 2π simulation. The field line in red is traced from exactly the same location in both images. In the top panel, the red field line is closed, and in the bottom, it is open. The interchange-reconnection point is at the sharp kink shown in the bottom panel, separating the old part of the field line, which obviously has not changed as it is traced back towards the Sun, from the new part of the field line with its open end. This kink verifies that the interchange reconnection is occurring principally at the top of the helmet streamer. The fact that the interchange takes place on high is not surprising because, for a force-free field, any magnetic twist or stress is expected to propagate to the region of weakest field (*Parker*, 1979). In our case, this corresponds to the top of the helmet streamer. It also happens to be the location of a pre-existing current sheet, the HCS, enabling the formation and enhancement of current sheets. Plasma distributed along the field line from the point of the kink down to the surface is now free to flow outwards into the solar wind, after residing in the hot corona on a closed field line.

Our result that a single field line can interchange over 50 times implies that a spacecraft sampling along a single field line could, in fact, sample plasma from regions that are remote from each other on the Sun. This would have the effect of spreading plasma from closed field lines out into the heliosphere, with the interchange reconnection acting as a kind of diffusion. The S-Web model (*Antiochos et al.*, 2011) predicts that photospheric motions broaden the regions where reconnection is likely to occur and increase the width of the source regions of slow solar wind in the heliosphere. Figure 2.17 shows the width of the dynamic slow-wind region in our simulation along the HCS. On the left, at time $t = -0.03$ h, line-tied field lines exhibit the dipolar shape of the magnetic structure before onset of driving, while field lines plotted within the HCS show the tangled magnetic fields of blobs, which are formed by the

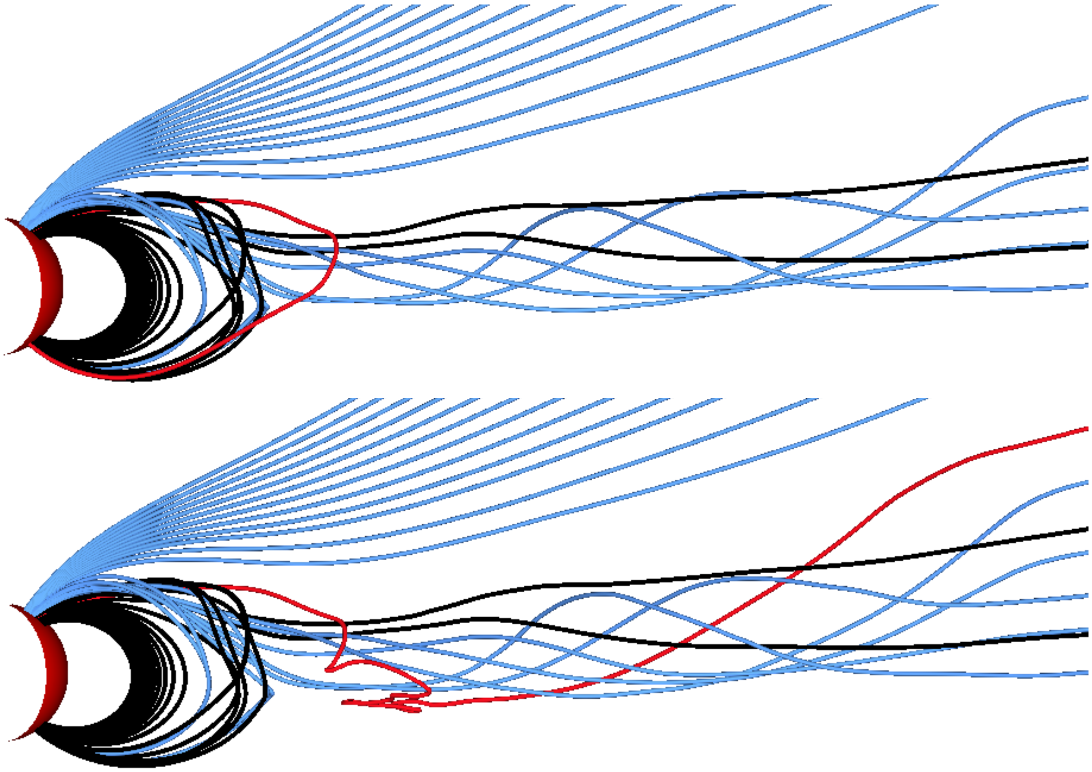

Figure 2.16: Example of an individual interchange event from the 2π displacement case. Blue field lines were originally open; black field lines were originally closed; red field line interchange-reconnects from closed to open between the top and bottom panels, which are 5 minutes apart. See text for details.

pinching off of the helmet streamer and convected out with the solar wind. In our case, the dynamic region near the HCS is due to blobs formed by numerical reconnection, so that the width of this dynamic region is determined by the grid. On the right, at time $t = 29.9$ h, the same blue line-tied field lines are plotted along with open field lines traced from within the flow region on the surface. Whereas on the left the dynamic region consists only of a narrow, 5°-wide region where the numerical resistivity causes the formation of blobs, on the right the width of the dynamic region is much broader, about 15°. Open field lines within this region trace outwards as far as 15°, but they also wrap into the HCS, mixing plasma from these two very different sources.

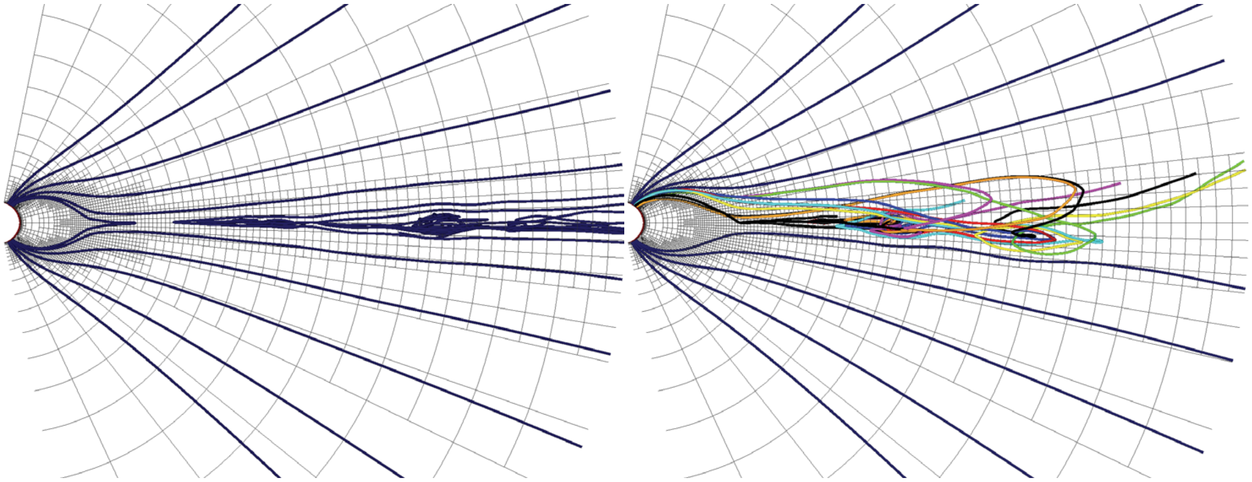

Figure 2.17: Change in width of the dynamic slow-wind region for the 2π displacement case. Left: Blue field lines in dynamic equilibrium show a narrow, $\sim 5°$ width of the slow solar wind. Right: Multi-colored field lines extend to much higher latitudes due to interchange reconnection driven by the photospheric flow, showing a broad, $\sim 15°$ width of the slow solar wind.

2.6 Conclusions

The simulations presented in this paper reveal several important new properties of the open-closed field boundary in the solar corona and heliosphere. The first is that, on the Sun, the magnetic field near this boundary responds to photospheric driving primarily via interchange reconnection. This result holds for the flows that are likely to be the most important drivers of the boundary: the quasi-random twisting and shearing, on time scales of a day or so, induced by the ever-present supergranular convection. Although we certainly see closed flux opening and open flux closing in our simulations, these processes are minor compared to the interchange reconnection. In fact, since interchange reconnection is so efficient, we expect that it also dominates the coronal-hole boundary evolution due to other driving motions, such as differential rotation or meridional flow, which have much larger spatial and temporal scales.

We conjecture that interchange will always dominate if the photospheric driving is fully 3D and if it involves mainly the displacement of existing photospheric flux, rather than a change in the amount of flux. If a large amount of new flux emerges so that the total unsigned flux at the photosphere increases significantly, then we expect that the amount of open flux must increase as well. Flux emergence, therefore, will result in closed flux opening, although there may also be some interchange. Conversely, photospheric flux disappearance will result in open flux closing. Large changes in the amount of photospheric flux, however, occur on the time scale of the solar cycle, of order years, whereas the time scale for flux evolution due to supergranular motions is only of order a day. We conclude, therefore, that interchange reconnection almost always dominates the dynamics at coronal-hole boundaries.

Another important finding from our simulations is that the time scale for boundary relaxation by interchange reconnection is commensurate with supergranular driving. It is evident from our 2π case that at an average speed of ~ 9 km s^{-1}, the photospheric motion induces a strong, nearly ideal, deformation of the coronal-hole boundary. Some relaxation occurred over the 6 h duration of our driver, but the interchange dynamics peaked several hours after the end of the driving and were significant for at least 30 h. If we were to reduce the driver speed by a factor of 5, so as to more closely match the solar photosphere, we expect that the boundary deformation would be smaller, but there would still be a pronounced deformation of the boundary and copious interchange reconnection. A possible caveat to this conclusion is that the effective Lundquist number for our simulation, which we estimate to be $\sim 10^4$, is orders of magnitude smaller than the actual solar value, $\sim 10^{12}$. In principle, this could result in much slower reconnection than is produced by our simulation and, thereby, alter the balance between interchange versus opening and closing. However, there are compelling arguments against this possibility. A key point is that our system has a large-scale separatrix surface, the open-closed boundary, with a null line and an initial current sheet, the HCS. A large number of simulations, by ourselves and many others, of systems with such pre-existing separatrices and null points show that stressing such topologies leads to the formation of current sheets at the separatrices on ideal-MHD time scales (*Priest and Forbes*, 2000). Furthermore, the rate of interchange reconnection need not be fast, but must merely keep pace with the slow photospheric driving. In our simulations, the reconnection rate is of order a few percent of the Alfvén speed, and there is no evidence of explosive reconnection. We expect, therefore, that on the Sun, where the driving is continuous and slow, the interchange reconnection would achieve a quasi-steady balance with the photospheric motions (e.g. *Edmondson et al.*, 2010a).

Our results also have important implications for understanding the topology of the open and closed flux in the corona. Careful examination of the movie for the 2π case reveals that, in spite of the extremely fine structure that develops during the evolution, both the closed- and open-flux regions remain simply connected. There is no evidence for disconnected open-flux patches within the closed-field region, even though the system is fully dynamic and includes numerous current sheets. This agrees with other simulations of coronal-hole boundary evolution (*Edmondson et al.*, 2010b; *Linker et al.*, 2011) and supports the coronal-hole uniqueness hypothesis of *Antiochos et al.* (2007). This result also provides indirect support for the S-Web model for slow-wind origin (*Antiochos et al.*, 2011), in contrast to the interchange model of Fisk and co-workers, which postulates that open flux can diffuse throughout the closed-field region (*Fisk et al.*, 1998; *Fisk*, 2003).

For understanding in-situ measurements of the slow wind, the most important conclusion from our simulations is that magnetic flux near the open-closed boundary is constantly undergoing cycles of opening and closing via interchange, on time scales of approximately 30 h. This implies that closed-loop plasma that has been in the corona for a day or more is continuously being released into the solar wind. Such plasma could well explain the observed characteristics of the slow wind, a charge-state abundance indicative of the closed corona, and significant FIP enhancements (*Zurbuchen*, 2007). We emphasize that the time scale of 30 h is critical, because it takes roughly a day for coronal loops to build up an elemental abundance that differs significantly from the photosphere (*Feldman and Widing*, 2002). Our results also can explain the observation that most of the slow wind does not exhibit bi-directional heat fluxes, which are evidence of flux opening, or heat-flux dropouts, which are evidence of flux closing (*Gosling*, 1990; *Lin and Kahler*, 1992). For remote-sensing observations of the corona, our calculations predict that the boundaries of coronal holes should have highly irregular structure, on scales considerably smaller than supergranules, and should exhibit a slow, quasi-cyclic evolution. It may be possible to identify such an evolution from high-resolution images of coronal holes.

It must be noted, however, that the Sun exhibits several features that are not included in our simulations and are likely to have strong effects on any observations of the corona and wind. In particular, the photosphere displays persistent emergence and cancellation of magnetic flux at both small and large scales. We expect this to drive systematic evolution of coronal-hole boundaries, including large-scale opening and closing, while small-scale emergence/cancellation will produce a constant background of brightening and dimming in coronal images. Even more important, the flux distribution at the photosphere is never that of a simple dipole. As a result, the distribution of coronal holes is almost never that of two simple polar holes, as in our simulation. The coronal-hole structure as inferred by either source-surface or MHD models (*Titov et al.*, 2011) generally is intricately organized, with multiple coronal-hole extensions reaching low solar latitudes. According to the S-web model, such a complex coronal-hole topology is essential for understanding the observations that slow wind can be found far from the HCS (*Antiochos et al.*, 2007, 2011). Future simulations with much higher numerical resolution will be required to understand the dynamical response of such a complex open-closed boundary to photospheric driving and to determine whether the ensuing dynamics can explain the slow solar wind.

CHAPTER III

Slow Solar Wind Arcs in the Heliosphere

This chapter is taken from A. K. Higginson, S. K. Antiochos, C. R. DeVore, P. F. Wyper, and T. H. Zurbuchen (2016), The Formation of Solar Wind Arches in the Solar System, manuscript in prep.

3.1 Abstract

A major challenge is to understand how highly localized regions at the Sun, with angular width $<$ 10-20 degrees, can be the source of solar wind near Earth with angular width $>$ 20 degrees. The Sun's atmosphere is divided into "open" regions, known as "coronal holes", where the plasma streams out freely as a wind that fills the solar system and "closed" regions where the plasma is confined to the corona by the strong solar magnetic field. The boundary between these regions extends outwards as the heliospheric current sheet (HCS). Measurements of plasma composition imply that the wind near the HCS originates in the closed regions, but mysteriously this type of wind is sometimes seen far from the HCS, which thus far remains unexplained. In Chapter 2 we calculated the dynamics a coronal-hole boundary due to photospheric motions for a simple dipole. Here we calculate the dynamics of a magnetic configuration in which a coronal hole has the geometry of a very narrow corridor flanked by closed field. We find that these dynamics result in the formation of giant arches of closed field plasma spanning tens of degrees in latitude and longitude at

Earth. The arches extend far from the HCS, thereby, accounting for the observations.

3.2 Introduction

The actions of the Sun's powerful and complex magnetic field create both the hot (1-2 MK) solar corona and the supersonic wind that forms the heliosphere (*Parker*, 1958). In regions where magnetic field lines start and end at the Sun's surface, the photosphere, plasma is confined to form the bright EUV loop structures of the so-called "closed" corona (*Orrall*, 1981). In "open" regions, however, field lines start on the Sun but extend out into the solar system allowing plasma to flow out freely as the solar wind. These regions appear dark in EUV, because the energy injected into the corona by the magnetic field is balanced by the energy carried away by the wind rather than by EUV emission; consequently open regions are generally referred to as "coronal holes" (*Zirker*, 1977). The combination of remote sensing observations of the Sun with in situ measurements near Earth has established that coronal holes are the sources of so-called fast wind, which usually has speeds > 500 km/s. In situ measurements, however, have shown that there is another major and clearly distinct component to the wind, the so-called slow wind, with speeds invariably < 500 km/s (*Schwenn*, 1990). Compositional studies of the two winds indicate that the slow originates back at the Sun from regions with temperature and elemental abundances that much more closely match the properties of the hot, closed corona than coronal holes (*Zurbuchen*, 2007).

These observations strongly imply that slow wind plasma originates in the closed field regions, but then somehow escapes onto open field lines and propagates into the heliosphere. Given the low electric resistivity of the corona, cross-field diffusion is expected to be negligible; consequently the only process by which closed field plasma can escape requires magnetic field dynamics. There are two such processes: either the rapid opening of closed field or the magnetic reconnection of open and closed flux resulting in the rapid transition of a field line section from closed to open (*Crooker et al.*, 2002). Since both processes are inherently dynamic, they imply that the slow wind should exhibit non-steady dynamics and, indeed, recent observations have confirmed that the slow wind has a distinct, dynamic structure (*Kepko et al.*, 2016). The observed location of the slow wind in the heliosphere also suggests that it is associated with closed field regions. Both dynamic processes above occur only at the boundary between open and closed flux in the corona. This boundary extends into the heliosphere as the so-called heliospheric current sheet (HCS) that separates outwardly directed from inwardly directed open field lines (*Smith*, 2001). We expect that slow wind would be preferentially located near the HCS and, in fact, observations show that the HCS is always imbedded in slow wind, never fast (*Burlaga et al.*, 2002). The longstanding problem, however, is that observations also show that slow wind is frequently located far from the HCS.

Figure 3.1A shows the Aug. 1 2008 eclipse as imaged from the ground (*Rušin et al.*, 2010). The magnetic structure of the solar corona is clearly visible. Near the poles, open-field rays extend outward. These regions are coronal holes, the source of the fast solar wind. At lower latitudes, streamer structures show the extent of the closed-field corona. These are the regions where slow solar wind is presumed to originate. Figure 3.1B shows the location of each type of solar wind in the heliosphere using interplanetary scintillation (*Tokumaru et al.*, 2010). Time is along the horizontal axis (where a Carrington rotation (CR) represents one full rotation of the Sun, with lower number CRs preceding higher), and latitude along the vertical axis.

In Figure 3.1B, the black line is the approximate location of the HCS, as extrapolated from measurements of the photospheric magnetic field (*Tokumaru et al.*, 2010). In 2008, a solar minimum year, we see from Figure 1B that the fast solar wind (blue and green) is generally concentrated near the poles, as expected. Furthermore, the slow solar wind (red and yellow) is generally concentrated about the HCS, also as expected. Completely unexpected, however, is the detection of slow solar wind far from the HCS, and at high latitudes in the heliosphere. In particular, we see that between CR 2073 - CR 2074 and CR 2071 - CR 2070 this slow wind can sometimes reach latitudes of thirty degrees or more and

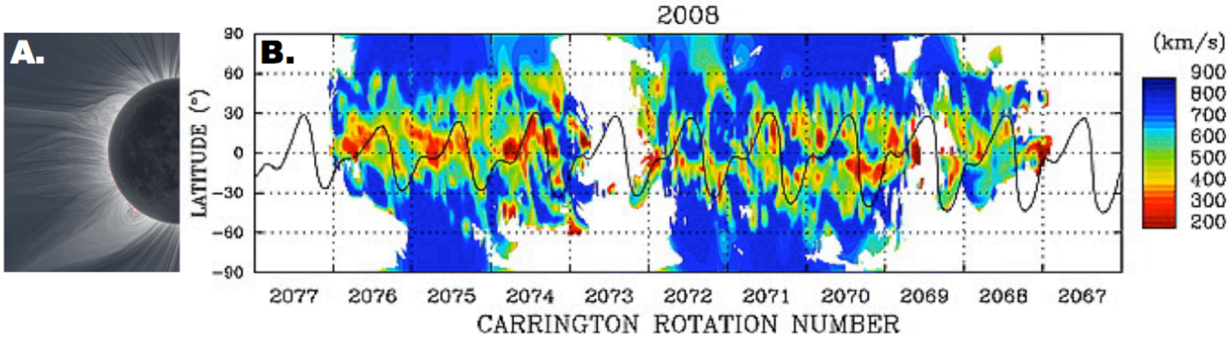

Figure 3.1: A. An image of the Aug. 1 2008 eclipse adapted from *Rušin et al.* (2010). The brightest regions are closed magnetic field, while the sharp rays over the poles are open magnetic field. (http://www.zam.fme.vutbr.cz/ druck/Eclipse/Index.htm) B. Solar wind speed for 2008 as determined from interplanetary scintillation measurements, adapted from *Tokumaru et al.* (2010). The black line is the estimated location of the heliospheric current sheet.

be nowhere near the HCS. In fact, there can even be fast solar wind between the two regions of slow solar wind, one near the HCS and the other at high latitudes. This surprising trend is also well documented in in-situ observations (*Zurbuchen*, 2007). The observation of slow wind far from the HCS poses a major conundrum. How can slow wind originate at or very near the HCS at the Sun, but then be found very far from the HCS in the heliosphere, and with no cross-field diffusion?

3.3 S-Web Model

The recently proposed Separatrix Web (S-Web) model offers a possible resolution to this long-standing conundrum (*Antiochos et al.*, 2011). The underlying idea of the model is that if the open field region in the corona has a particular geometry, then the mapping of the open flux into the heliosphere can be quasi-singular with flux very near the open-closed boundary mapping to locations far from the HCS. Although such geometry for the open field may appear contrived, in fact, it occurs frequently on the Sun.

Figure 3.2A shows such a case in an EUV image taken by the Solar Dynamics Observatory. Here, coronal holes appear darker than the surrounding corona due to their cooler

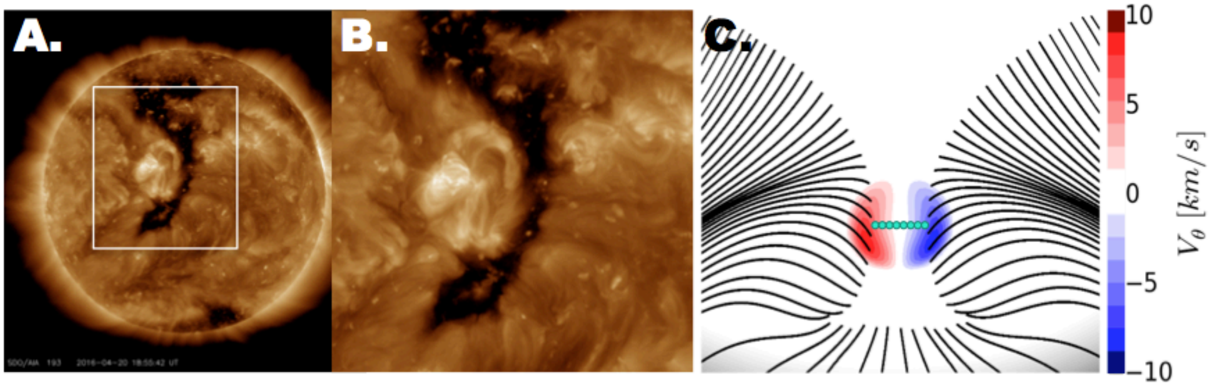

Figure 3.2: A. An EUV image of the Sun taken by the Solar Dynamics Observatory (SDO). A coronal hole appears dim relative to the hot corona. B. A zoom-in of the white box from A. The coronal hole extends from the pole down to low latitudes and the two regions are connected by a narrow open-field corridor. C. Our simulated S-Web corridor. The black magnetic field lines outline the location of the open field corridor and lower latitude coronal hole on the surface. The colored contours represent the maximum theta velocity applied by the driver.

temperature. Figure 3.2B is a zoom-in of the white box in Figure 3.2A, showing a lower-latitude coronal hole connected to the polar coronal hole by a narrow corridor. In order to determine how the open flux in a corridor maps to the heliosphere, we calculated a numerical model shown in Figure 3.2C for a coronal hole configuration that is geometrically very similar to that in Figure 3.2B. This model calculates a quasi-steady MHD solution for the corona and wind, and is described in more detail below. The black magnetic field lines in Fig. 3.2C outline the coronal-hole boundary, indicating the presence of a corridor connecting the polar coronal hole to a low latitude hole. This ”elephant trunk” configuration invariably forms whenever low latitude active regions appear at the solar surface (*Zirker*, 1977).

From the numerical model, we can determine exactly how the magnetic field maps from the open field corridor into the heliosphere, Figure 3.3. Here, the yellow sphere is the solar surface at 1 solar radius. The current density in the ecliptic plane (gray contours) is also shown to highlight the location of the HCS, the boundary between the open field that originates in the north and south. Fig. 3.2C shows a line of blue dots drawn on the solar surface and across the narrowest part of the corridor. The blue magnetic field lines in Fig. 3.3 are traced from this line. Although the line of dots in Fig. 3.2C is very short, its magnetic mapping into the heliospheric forms a giant arch covering tens of degrees in latitude and longitude. Note also, that the flux from the polar coronal hole maps to everywhere above this blue arch and the flux from the lower-latitude coronal hole maps to the region between the arch and the heliospheric current sheet. As long as the fluxes in polar and low-latitude holes stay relatively constant, then the blue arch in the heliosphere maintains its large angular extent irrespective of how narrow the corridor becomes. This result is the primary motivation for the S-Web model.

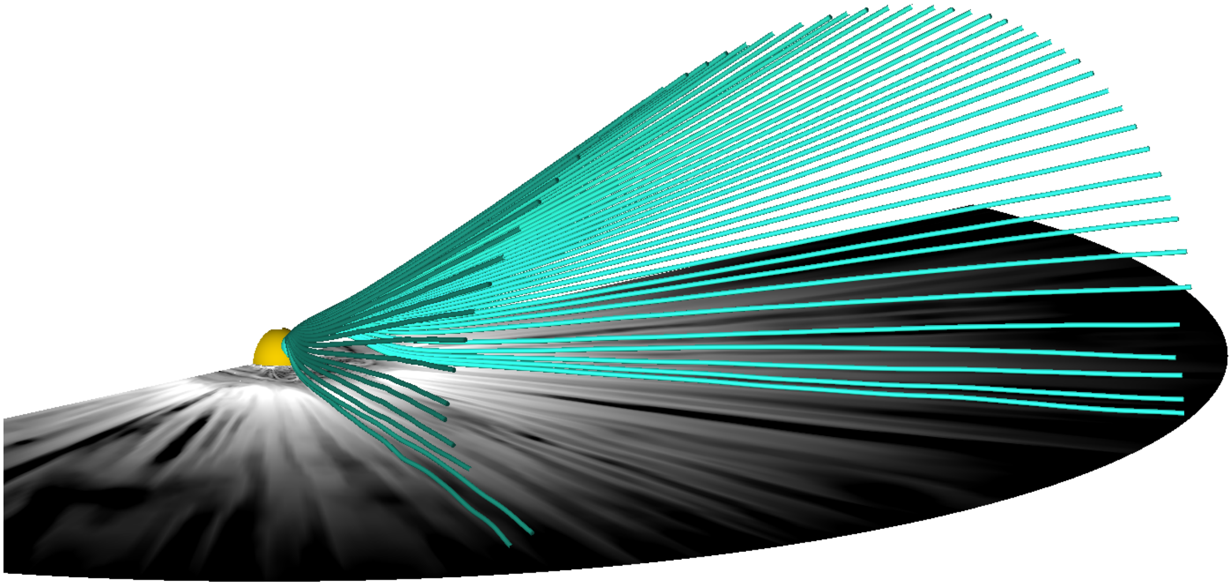

Figure 3.3: The initial S-Web arch in our numerical simulation. The yellow surface is drawn at 1 solar radius, the blue magnetic field lines start in the coronal-hole corridor at the blue line shown in Fig. 3.2C and end at 30 solar radii, and contours on the plane at zero degrees latitude show the varying current density within the HCS.

Of course in a purely steady-state model, as in Fig. 3.3, then all the closed field lines remain closed and there is no slow wind plasma anywhere. The coronal magnetic field, however, is being constantly stirred by convective motions, in particular, by the large cells known as supergranules, which are ever present at the solar surface. Supergranules have a size scale of 30,000 km, lifetimes of 30 hours or so, and typical horizontal velocities of 1 km/s (*Bray and Loughhead*, 1967). The key conjecture of the S-Web model is that supergranular driving of the magnetic field at open-field corridors results in the release of closed field plasma all along an arch as in Fig. 3.3. If correct, then this would naturally account for the observation of slow wind far from the HCS, but it is not at all clear how the model can be correct. The magnetic field dynamics are simply the processes of closed flux opening and open-closed reconnection (so-called interchange reconnection) described above, and these must occur at the open-closed boundary, in other words, where the blue arch intersects the HCS. It is far from clear whether these dynamics can release closed field plasma at the center of the blue arch, for example, which can be tens of degrees in angular separation from the HCS. In order to answer this question, we perform the first numerical simulations of an open field corridor driven by photospheric motions and determine whether the resulting dynamics can resolve the slow wind conundrum.

3.4 Numerical Model

For our simulations we use the Adaptively Refined Magnetohydrodynamic Solver (ARMS), which solves the 3D, ideal MHD equations. The atmosphere is a single isothermal fluid (held at T = 1 MK) that is initialized using the transonic solar-wind equation from *Parker* (1958). Combined with our boundary conditions, this results in a self-sustaining solar wind. The initial magnetic field distribution is taken from *Antiochos et al.* (2011), which uses the source surface model (*Altschuler and Newkirk*, 1969) to create of a polar coronal hole with a low latitude hole and an open field corridor connecting them. Once the atmosphere and the magnetic field are initialized we allow the model to relax so that the two come into the steady MHD equilibrium shown in Figure 3.3.

To simulate supergranular driving of this field, we apply a large rotational velocity on the surface that spans the corridor. For accurate numerical resolution the scale of the corridor and, hence, of the flow is larger than actual supergranules, but as discussed above, these can be scaled down to solar values with no change in the essential magnetic structure. The theta components of the velocity are shown in Figure 3.2C. The maximum velocity is 9 km/s, which is larger than observed photospheric motions, but still far smaller than the coronal Alfvén speed of approximately 1,000 km/s. The flow is turned on long enough to move field lines from one side of the corridor to the other, a rotation of 180 degrees. We then turn off the flow and allow the system to relax for roughly one day. Of course, the actual supergranular flows are much more complex than a simple half turn, but if this simple driving can account for the slow wind then as discussed below, the quasi-chaotic driving of the supergranular flows will be even more effective. For further model details, see Appendix **??**.

3.5 Results

The photospheric driving has three main effects on the coronal magnetic field. In open regions it launches an Alfvén wave that propagates outward and rapidly relaxes the open flux back to its lowest energy state. In closed regions, however, the driving induces a large-scale twist to the flux, which cannot be easily dissipated. As will be shown below, the driving also strongly distorts the open-closed boundary leading to the formation of current sheets there and to efficient interchange reconnection between open and closed flux. This interchange reconnection has profound consequences for understanding the slow solar wind.

Figure 3.4 shows the striking effects of this interchange reconnection on the corona and heliosphere. Plotted are six field lines traced from fixed foot points at the solar surface and at three different times. Figure 3.4A shows these field lines at the end of the driving, at t = 9.5h. The field lines are all closed at this time. Figure 3.4B shows the field lines traced from the same foot points only 5 minutes after Figure 3.4A, and Figure 3.4C shows them 10 minutes after Figure 3.4A. Also shown are the same yellow radial surface at 1 solar radius and the plane of current density from Figure 3.3, except that now the system is viewed edge on. The field lines are drawn from foot points in the northern hemisphere and the coronal-hole corridor is at the center of the Sun from the perspective of the viewer. The edge of the box is at about 15 solar radii.

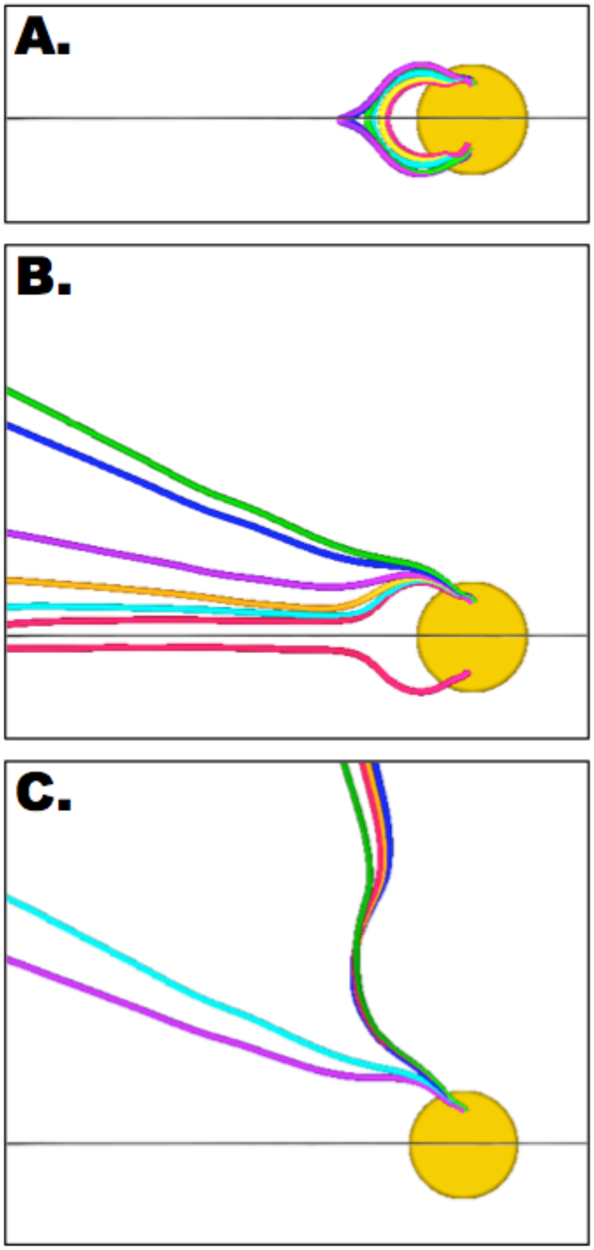

Figure 3.4: Six magnetic field lines traced from the same foot points at the edge of the coronal hole corridor in the northern hemisphere. A. Immediately after the driving on the surface has stopped at t = 9.5 h, all the field lines are closed. B. Five minutes after A, five of the six field lines are open. C. Five minutes after B, all field lines are open, several reaching above 30 degrees.

The field line "dynamics" shown in Fig. 3.4 are the main result of our simulation. They resolve the slow wind conundrum. First, note that all the foot points at the solar surface are held fixed during the 10 minutes of the Figure; consequently, any changes in the field lines must be due to evolution in the corona and heliosphere. Furthermore, the solar wind flow speed near the top of the closed field region is small, < 100 km/s, so that in the time span of 5 minutes, closed field lines can move only about 10,000 km or so, which is an imperceptible distance on the scale of the figure. All the changes, therefore, must be due to rapid reconnection and not actual plasma dynamics. Even the change in the red field line that remains closed in going from Fig. 3.4A to 3.4B must be due to reconnection. Note also the curve in the highest field lines in Figure 3.4C. This curve is due to the Alfvén wave launched in the open flux by our initial motion. The propagation of this wave has reached only 12 solar radii by this time, further demonstrating that the change to an open connectivity is due to reconnection and not propagation of disturbances in the magnetic field.

The striking result shown by Fig. 3.4 is that in the space of only five minutes, five of the closed "field lines" in 3.4A have become open, 3.4B, and not only are they open, but they connect to high latitude, 15 degrees or so above the HCS. After another five minutes the red field line has also opened and the five open ones have reconnected again to reach even higher latitudes, > 30 degrees or so above the HCS. This second (or possibly more) reconnection occurs between open field lines. It is not the well-known open-open reconnection across the HCS that produces disconnected flux citepcrooker02, but the recently discovered solar wind reconnection at finite shear angle (*Gosling and Phan*, 2013). Examination of the field line structure reveals that the reconnections responsible for the apparent evolution in Fig. 3.4 occur high in the corona, near the HCS, where open and closed fluxes diverge.

It is worth emphasizing again that the changes seen in Fig. 3.4 are only an apparent evolution. They do not reflect any actual motion of the field or plasma, but only a change in field line connectivity. These connectivity changes are so fast that the closed field plasma in the coronal sections of the six field lines has barely time to move. The key point is that at the time of Fig. 3.4C, the field line sections in the corona contain closed field plasma, which is now free to move out along the open field line section to form a piece of slow solar wind. We conclude, therefore, that the photospherically driven dynamics of an open field corridor does result in the release of closed field plasma far from the HCS, as required to explain the observations.

To understand the overall evolution of the corridor magnetic field throughout the relaxation period after the flow, we trace field lines from a grid of foot points on the surface spanning the coronal hole corridor and encompassing part of the closed and open field to either side. This grid spans between $-/+15$ degrees longitude and 15-45 degrees latitude in the northern hemisphere. Figure 3.5 shows the location in latitude and longitude on a surface at 12 solar radii of every field line that connects to a foot point, which changed from closed to open. The locations on this surface of each of these newly open foot points are tracked and continued to be plotted. This allows us to measure any further reconnection of the field lines from these foot points. If the foot point becomes closed again, it is no longer shown. To keep track of the length of time that has passed since each foot point became open, we color the points on the 12 solar radii surface by age, where yellow indicates foot points that have only just become open, and purple indicates points that have been open for nearly a day. Figure 3.5 is shown at the very end of the simulation, at time t = 32.2h, 22.7 hours after the end of the driving. A movie version of Figure 3.5 showing the entire simulation is available in Appendix B.

The first important conclusion from the figure is that newly opened field lines cover almost the complete S-web arch of Fig. 3.3. There does appear to be a gap near the arch apex, but this is likely due to the fact that Fig. 3.5 substantially underestimates the flux that has transitioned from closed to open. There is a considerable amount of interchange reconnection during the driving phase itself that is not captured in Fig. 3.5. But even without this flux, it is clear that a substantial amount of flux that used to be closed, has

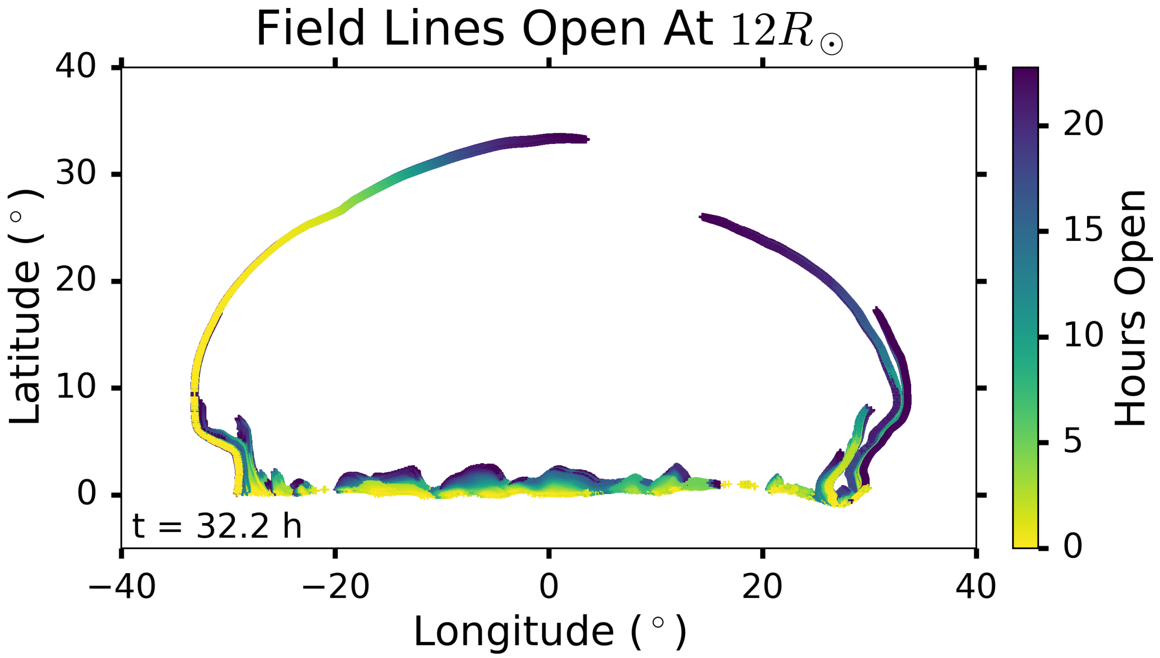

Figure 3.5: The location of field lines on a surface at 12 solar radii. Only field lines that opened after the driver stops are shown. The color scale represents how long they have been open. Shown at the end of our simulation at t = 32.2 h, almost one day after the driving ends. The movie for the full simulation can be found in Appendix B.

opened high above the HCS.

Another important conclusion is that foot points continue to open throughout the evolution; almost a full day after the driving has stopped. The movie, available in Appendix B, shows that in the yellow locations along the left side of the arch up to 30 degrees and along the HCS, field lines are constantly opening throughout the simulation. These are locations where coronal plasma forming the slow solar wind would be released continuously. The purple field lines at the top of the left leg of the arch, above 30 degrees latitude, opened soon after the end of the driving and then remained open for the rest of the simulation. The connectivity at these locations changed more rapidly than solar wind plasma could flow out to 12 solar radii, consequently, these are locations where closed field plasma could be observed by spacecraft. In fact, we expect that closed field plasma indicative of the slow wind would eventually show up along the whole arch.

The right leg of the arch in Figure 3.5 and the movie also consists mainly of field lines that connect to photospheric points, which changed from closed to open early in the evolution and remained open. It is important to note that none of the purple points at high latitudes, between 10 and 25 degrees latitude, first appeared there. All these points first became open down near the HCS, and then moved quickly up to their higher latitudes. For this to be a real motion of the magnetic field and plasma would require velocities of $\sim$ 35 km/s $<$ V_θ $< \sim$ 500 km/s. We measured the plasma velocities in the region, and these are only on the order of $V_\theta \sim$ 2 km/s. This result demonstrates again that the connectivity at high latitudes is changing via rapid open open reconnection. This rapid transport of open field lines along the S-Web arch would have the same effect as immediate opening throughout this region. Figure 5, therefore shows that even a simple and relatively short-lived distortion of the coronal-hole boundary can release slow wind plasma all along the blue solar wind arch of Figure 3.3.

The rapid transport of flux along the S-Web arch is the most important, but perhaps, least intuitive result of our simulation. This rapid transport is essential for obtaining closed field plasma far from the HCS. Figure 3.6 clarifies how the mapping of the magnetic field in the coronal hole from the surface to the heliosphere enables this transport. The contours are on the solar surface, and are colored by field line connectivity. The black and gray regions are closed. The black regions correspond to foot points of field lines that map from the northern to the southern hemispheres, while the gray regions are points where the field lines map into the active regions located on either side of the coronal-hole corridor. These gray regions correspond to short loops, while the black regions contain loops on the order of a solar radius. The white to purple contours correspond to open flux, with the lighter regions mapping closer to the HCS, and the darker regions mapping to higher latitudes. Here in Figure 3.6 we show just two panels of the full movie available in Appendix B.

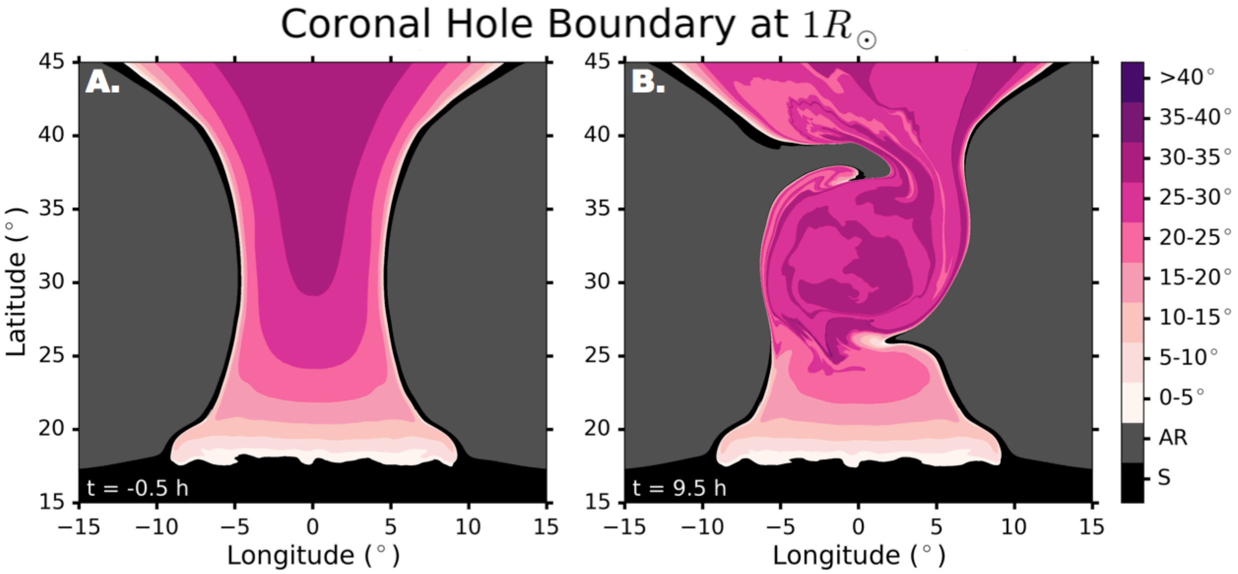

Figure 3.6: Color contours show how the magnetic field from the surface at 1 solar radius maps to the surface at 12 solar radii. Black regions show where closed field lines connect from the northern to the southern hemisphere (labeled S). Gray regions show where closed field lines connect to nearby active regions in the north (labeled AR). The pink to purple contours show how the latitude to which the open field lines in the corridor map. A. Before the driving. B. After the driving. The full movie is available in Appendix B.

Figure 3.6A shows that before the photospheric driving, the field line mapping is smooth and well resolved by our numerical grid. The S-Web corridor as shown in Figure 3.2C is cleanly distinguished. The edges of the coronal hole corridor are light in color, and the gradient from the edges, which map to the HCS, and the center of the coronal hole, which maps to high latitudes is smooth, stepping through each successive contour (as shown in by the foot points in Figure 3.2C and the field lines in Figure 3.3. For this magnetic topology reconnection between an open and closed field line is possible only for a field line from the black region, which closes to the south, and a field line from the white region which maps to fairly low latitude, between 0 and 5 degrees. Furthermore, the smoothness of the mapping in the open flux region indicates that any open - open reconnection would result in a negligible change in field line latitude. For the topology of Fig. 3.6A, we expect that all opening and, consequently, all slow wind would be constrained to occur very near the HCS. This is the usual situation.

Figure 3.6B, however, which shows the same contours at the end of the driving, implies a very different scenario. The coronal-hole boundary has been distorted by the photospheric driving, with a closed-field region extending deep into the open-field corridor. The colored contours in the open-field region have also been distorted far beyond what would be expected from just a simple rotational motion. Open field flux that maps to between 20 and 30 degrees latitude is now directly adjacent to closed flux. Since the mapping between the edges and center of the coronal hole is not smooth, interchange reconnection is indeed possible between a closed field line and one that maps to high latitudes. Furthermore, the mapping within the open field region has become quasi-singular so that open open reconnection can rapidly change the latitudes of field lines. This quasi-singular field line mapping of the flux in the vicinity of open field corridor when driven by photospheric motions is the underlying reason that closed field plasma can appear all along the arch of S-Web arch.

It should be noted that for the Sun, the field line mapping is certain to be even more singular than that shown in Fig. 3.6A, because convective cells appear and disappear randomly over the whole solar surface. Moreover, the magnetic field distribution on the Sun often generally shows much more complexity than the simple single corridor of Fig. 3.2. Observed solar photospheric flux distributions generally produce many coronal holes existing in many locations and at many scales. Such a network of coronal holes creates an equally complex network of solar wind arches, which are capable of covering a wide band surrounding the HCS (*Antiochos et al.*, 2011; *Crooker et al.*, 2012). Our simulations prove that the dynamics along these S-Web arches can indeed release slow solar wind plasma from the closed-field corona to high latitudes in the solar system, possibly to an even greater extent than predicted. We conclude, therefore, that the giant arches of slow solar wind implied by Fig. 3.3 are likely to be a fundamental and pervasive feature of the solar atmosphere and heliosphere.

CHAPTER IV

S-Web Dynamics and Solar Energetic Particles

4.1 Introduction

The S-Web topology is a large-scale feature of the Sun's magnetic field, consequently the role of its dynamics throughout the heliosphere must be considered. Previous chapters have established the effect of the S-Web on the distribution of slow solar wind. It is likely that the S-Web plays a large role in determining the distribution of impulsive solar energetic particle (SEP) events as well. Impulsive SEP events are composed of energetic electrons (10-100 keV) (*van Allen and Krimigis*, 1965; *Lin*, 1970a,b), which often produce type-III radio bursts (*Wild et al.*, 1963) and enhancements in ^{3}He (e.g. *Reames et al.*, 1985). These SEPs are associated with soft x-rays (*Pallavicini et al.*, 1977) and are believed to be accelerated near the site of solar flares (*Reames*, 1999, 2013, and references therein). This in contrast to the much larger "gradual" SEP events, which are linked to shock acceleration associated with CMEs, in which ^{3}He is not enhanced above coronal values (*Kahler et al.*, 1978; *Reames et al.*, 1988; *Cliver et al.*, 2004).

Although it was expected that gradual SEP events would have a wide spread in heliosphere, due to the expansion of the driving CME, it was long thought that in order to observe impulsive SEP events the viewer needed to be magnetically connected to the flare source on the sun (*Reames*, 1999). However, the launch of the two Solar TErrestrial RElations Observatory (STEREO) spacecraft in 2006 have since enabled observation of the full-sun simultaneously, and many impulsive SEP events with surprisingly large longitudinal spreads ($> 100°$) have been recorded (*Wiedenbeck et al.*, 2013). Interestingly, not all of the impulsive SEP events observed by the two STEREO spacecraft have this large extent. Some have the expected narrow width in the heliosphere, meaning that it was not just the lack of 3D observations of the Sun that mischaracterized the impulsive events. As stated by *Cohen* (2016), "Since not all ^{3}He-rich events are wide, yet the wide events are not rare, the process(es) involved must be neither ubiquitous nor uncommon."

There have been many attempts to model this spread of impulsive SEP event particles using particle diffusion (e.g. *Giacalone and Jokipii*, 2012). The problem with pure diffusion, however, is that somehow this diffusion must also be selective. During an SEP event, a single spacecraft can experience sudden "dropout" events, which are believed to be a result of flux tubes that do not contain energetic particles sweeping past the instrument (*Mazur et al.*, 2000; *Chollet and Giacalone*, 2011; *Giacalone et al.*, 2000).

These energetic particles act as fast tracers of the magnetic field, reaching 1 AU in a fraction of an hour. Therefore, in order to understand their motion, it is necessary to understand the structure of the magnetic field in the heliosphere and its connectivity to source regions on the Sun. The S-Web theory predicts that the spread of an SEP event should depend on the structure of nearby coronal holes and their fluxes relative to the entire coronal-hole system on the Sun. In other words, it depends on what the S-Web looks like and how well a particular flare region is connected to it. If a flare site is close to a coronal-hole corridor for example, the nearby field lines will map to the resulting large S-Web arc, distributing energetic flare particles along its length. This could explain why some SEP events have a large longitudinal extent and others do not. Additionally, because the spreading mechanism of the S-Web does not depend on pure diffusion of the particles across the magnetic field (although it may be thought of as an "effective diffusion"), this would allow for the observation of dropouts, as the S-Web predicts steep gradients in the mapping of fluxes within the open field (see Chapter 3).

There is one impulsive SEP event in particular that has been studied extensively (*Wiedenbeck*, 2011; *Wiedenbeck et al.*, 2013; *Giacalone and Jokipii*, 2012; *Dröge et al.*, 2014). Our numerical simulation from Chapter 3 is a good approximation of the overall structure of the coronal-hole boundary at that time, and so we present below a preliminary analysis of S-Web magnetic field dynamics in the context of impulsive energetic particle propagation.

4.2 Observations

An M-class flare on 7 February 2010 produced energetic particles that were observed by the STEREO-A, STEREO-B, and Advanced Composition Explorer (ACE) spacecraft. The location of the flare is shown in the EUV image in Figure 4.1 recorded by the Extreme Ultraviolet Imaging Telescope (EIT) on the SOlar and Heliospheric Observatory (SOHO) spacecraft. A Carrington map including this time in Figure 1.2 shows the magnetogram measured by the Global Oscillation Network Group (GONG). The star marks the location of the flare, which is near a large active region. Plotted on top of the magnetogram is the HCS (white line) and the magnetic connectivity of the ecliptic plane back to the Sun as estimated by a PFSS model (green and red). The location of STEREO-B, ACE, and STEREO-A is also shown. According to this model, STEREO-B is magnetically connected to a region close to the flare site, while ACE and STEREO-A seem to be connected to regions farther away.

The locations of the STEREO-A, STEREO-B, and ACE spacecraft relative to the Earth-Sun line are shown in Figure 4.3, where the green dotted line shows the estimated magnetic connectivity of the flare region. ACE orbits about the L1 Lagrange point and so is always near the heliographic longitude 0. STEREO-A was 65° ahead of Earth and STEREO-B was 71° behind, giving a full observed spread of 136° in the heliosphere.

Figure 4.4, taken from *Wiedenbeck et al.* (2013), shows the data recorded by the three spacecraft. Panel a shows the ^{3}He intensity for each spacecraft, Panel b the intensity of electrons with energies between 70-100 keV, and Panel c shows the x-ray flare intensity with

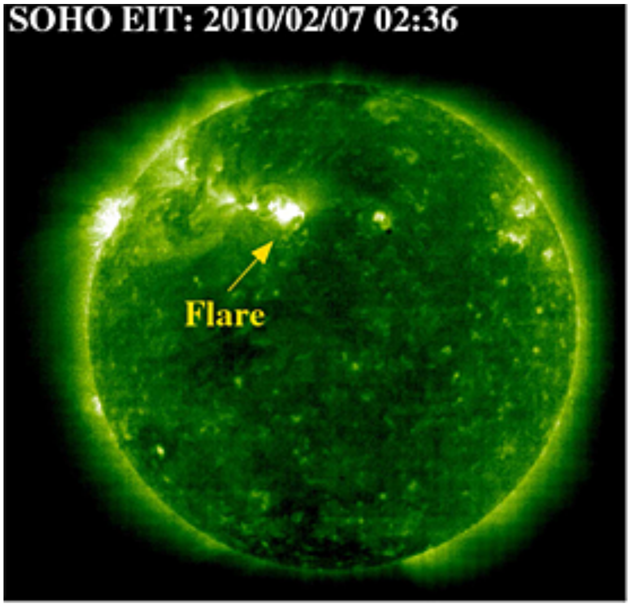

Figure 4.1: Observations of the SOHO Extreme Ultraviolet Imaging Telescope (EIT) during the flare maximum on 7 February 2010 at 02:36 UT. The location of the flare is indicated by the arrow. Taken from *Dröge et al.* (2014).

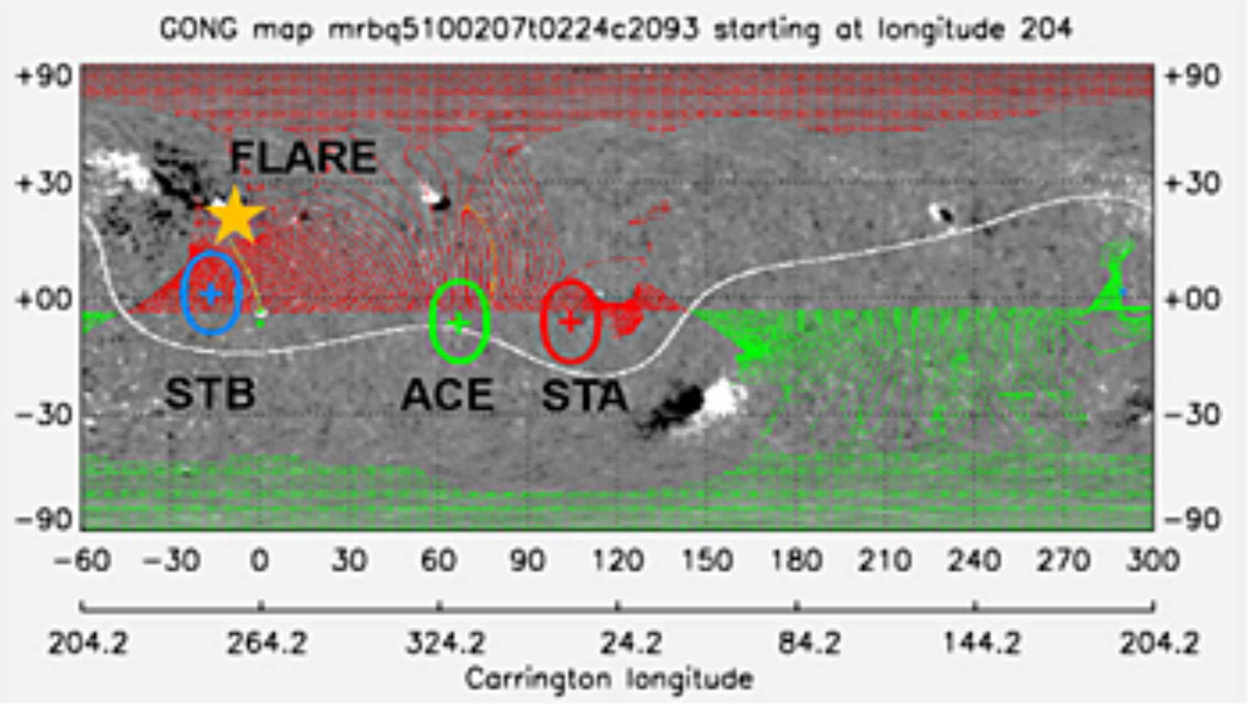

Figure 4.2: Synoptic Ecliptic Plane Field Plot overlying a magnetogram map by the Global Oscillation Network Group (GONG) for Carrington rotation 2093. Also marked are the estimated positions of the magnetic foot points of the three spacecraft and the position of the flare. Taken from *Dröge et al.* (2014).

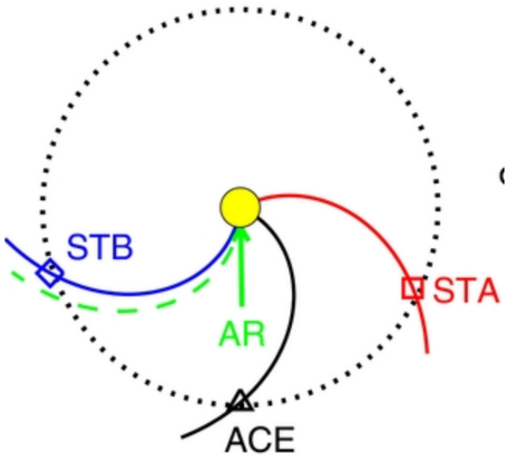

Figure 4.3: Geometrical arrangement of the STEREO-B, ACE, and STEREO-A spacecraft and the flaring active region at the time of the 2010 February 7 ^{3}He-rich event. The dotted circle corresponds to a radius of 1 AU. Taken from *Wiedenbeck et al.* (2013).

time. The colored arrows in Panel a indicate the onset time of the event at each spacecraft. STEREO-B observed the ^{3}He particles first and observed the largest intensity, followed by ACE and then STEREO-A. Comparing Panels a and b it appears that the the largest peaks in ^{3}He are associated with the smaller peaks in electron intensity which followed the large event on 7 February 2010.

Using the fluence of 2.3-3.3 MeV ^{3}He measured by STEREO-A and STEREO-B, *Wiedenbeck et al.* (2013) was able to estimate to estimate the fluence at ACE (whose measurements fell below and above this range) and the resulting comparison between the three spacecraft is shown in Figure 4.5. Here, the fluence is plotted against the heliographic longitude of the three spacecraft and fit with a Gaussian. This Gaussian, with a standard deviation of $\sigma = 48°$, describes the fit quite well and the authors note that this is quite suggestive of a diffusive process from a point source. It may be possible, however, that rather than diffusion, these fluxes depend on the distance away from the flare site along an S-Web arc.

To check if field line spreading could be responsible for the 136° spread of these observations, *Wiedenbeck et al.* (2013) also performed an analysis of daily PFSS maps over a 14 year period. For each map, field lines grouped in patches of varying radii were traced and the

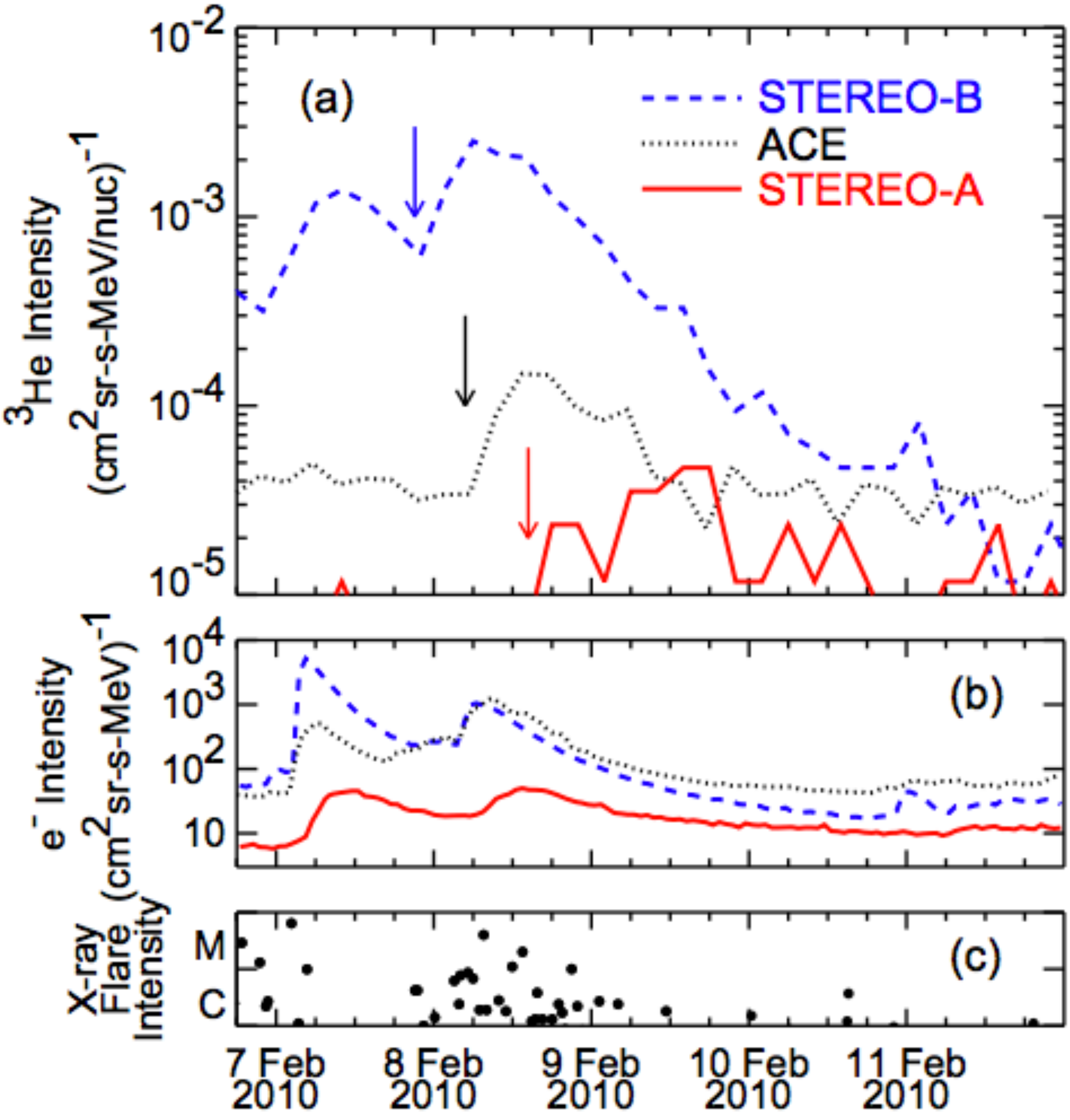

Figure 4.4: (a) Intensity of 3He vs. time measured at the three spacecraft. STEREO data are LET measurements at energies of 2.33.3 MeV/nucleon. ACE data are SIS measurements covering 4.616.3 MeV/nucleon. Arrows indicate the approximate times of the event onsets. (b) Intensity of 0.070.1 MeV electrons vs. time at the three spacecraft. The STEREO data are from the SEPT instruments and the ACE data are from the EPAM instrument. (c) X-ray intensity vs. time for identified solar flares of GOES class C1.0 or greater. Taken from *Wiedenbeck et al.* (2013).

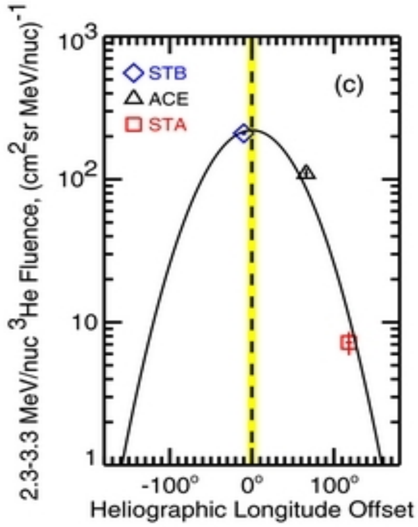

Figure 4.5: Dependence of measured fluence in the 2.3-3.3 MeV nucleon^{-1} energy interval on heliographic longitude. The abscissa is the longitudinal offset of the spacecraft locations from the 1 AU longitude of the Parker spiral field line that originates at the active region. Shading (yellow) about the dashed vertical line indicates the approximate $\pm 1\sigma$ uncertainty in the source location. Taken from *Wiedenbeck et al.* (2013).

largest spreads for each day were recorded. They found that even for field lines originating within a 10° radius of each other, which is the size of several supergranules on the surface, the probability of these field lines ever having a spread of 136° was so rare as to state that it would be impossible for field line spreading to account for the observations. Our results suggest, however, that these PFSS maps do a poor job of reflecting the spread of field lines in the heliosphere. The mapping in the open field can be far from smooth, especially in complex coronal holes, and PFSS maps by their nature can never account for dynamic processes.

4.3 Methodology

The SEP event from 7 February 2010 is an excellent candidate for comparison with the numerical simulation described in Chapter 3. Figure 4.6 shows the same magnetogram as Figure 4.2 except now the red and green represent the estimated locations of coronal holes. The blue lines are the last closed field line at the top of the helmet streamer and trace out the location of the HCS. Figure 4.7 shows these coronal holes and the helmet streamer on a spherical surface, highlighting the large tilt of the HCS. Comparing the location of the flare, marked in Figure 4.2, with Figure 4.6 we see that the flare site and associated active region were at the edge of a coronal hole corridor. The numerical simulation from Chapter 3 involved a coronal hole corridor flanked on either side by large active regions (see Figures 1.8 and 3.2) and so, while the complexity of the coronal hole distribution is not captured by our simulation, the set up is still a reasonable simplification.

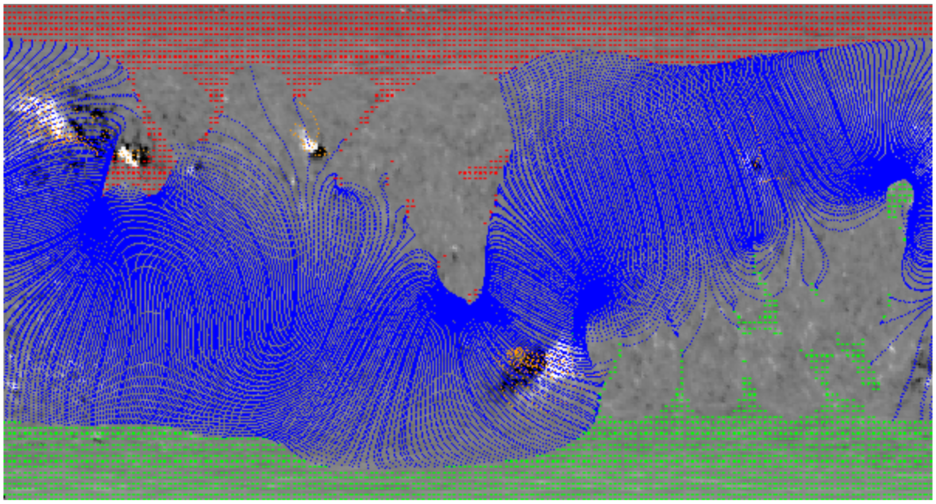

Figure 4.6: A PFSS approximation of magnetic field distribution and coronal hole location (using a source surface of r = 2.5 $R_\odot$) plotted on top of a GONG synoptic magnetogram for Carrington rotation 2093. Here, open positive field is green, open negative flux is red, and the tallest closed field lines are shown in blue. The magnetic flux density on the surface is indicated by a gray scale from white (positive) to black (negative). (http://gong.nso.edu/data/magmap/mod3.html)

To study the magnetic field dynamics in our simulation as they relate to SEP event particle propagation, we traced magnetic field lines from 2000 x 2000 stationary points on the surface at 1$R_\odot$ to 12$R_\odot$ in three locations. Each of these grids are 10° x 10°, as shown by the boxes in Figure 4.8. Each box extends from -10° to 0° in longitude. The red box extends from 25° to 35° in latitude, the blue box from 30° to 40°, and the yellow box from 35° to 45°. The four panels in Figure 4.8 show the coronal-hole boundary in the same manner as previous chapters, where white regions are open field, and black regions are closed-field.

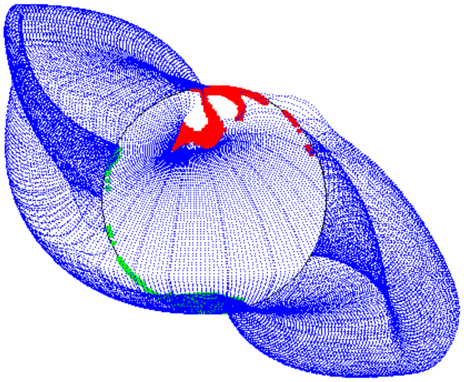

Figure 4.7: The coronal holes and tallest closed field lines (see Figure 4.6) for Carrington rotation 2093 are plotted in spherical coordinates and viewed from the Sun-Earth line. (http://gong.nso.edu/data/magmap/gmodel.html)

The time since the start of the driving phase for the simulation is shown in the bottom left corner of each panel. The top left panel shows the coronal-hole boundary before driving, the top right at its time of maximum displacement, the bottom left at a time near the end of the driving, and the bottom right at the end of the simulation after an undriven relaxation period. The boxes were chosen to cover the left coronal-hole boundary during the simulation since it is this side which exhibits the largest deformation. However, because of the differences in transport mechanism on each side of the simulated S-Web arc (as discussed in Section 3.5), interesting dynamics from the right side should not be ruled out and warrant further investigation.

4.4 Results

For each of the three 10° by 10° grids of field lines, we tracked both the instantaneous and accumulated areas covered in latitude and longitude by open field lines. We refer to this area as A with the subscripts θ, ϕ, I, and A, where I and A refer to instantaneous and accumulated respectively. These areas were found by dividing the heliosphere into latitude and longitude bins with widths of 1°. The number of occupied bins at each time throughout

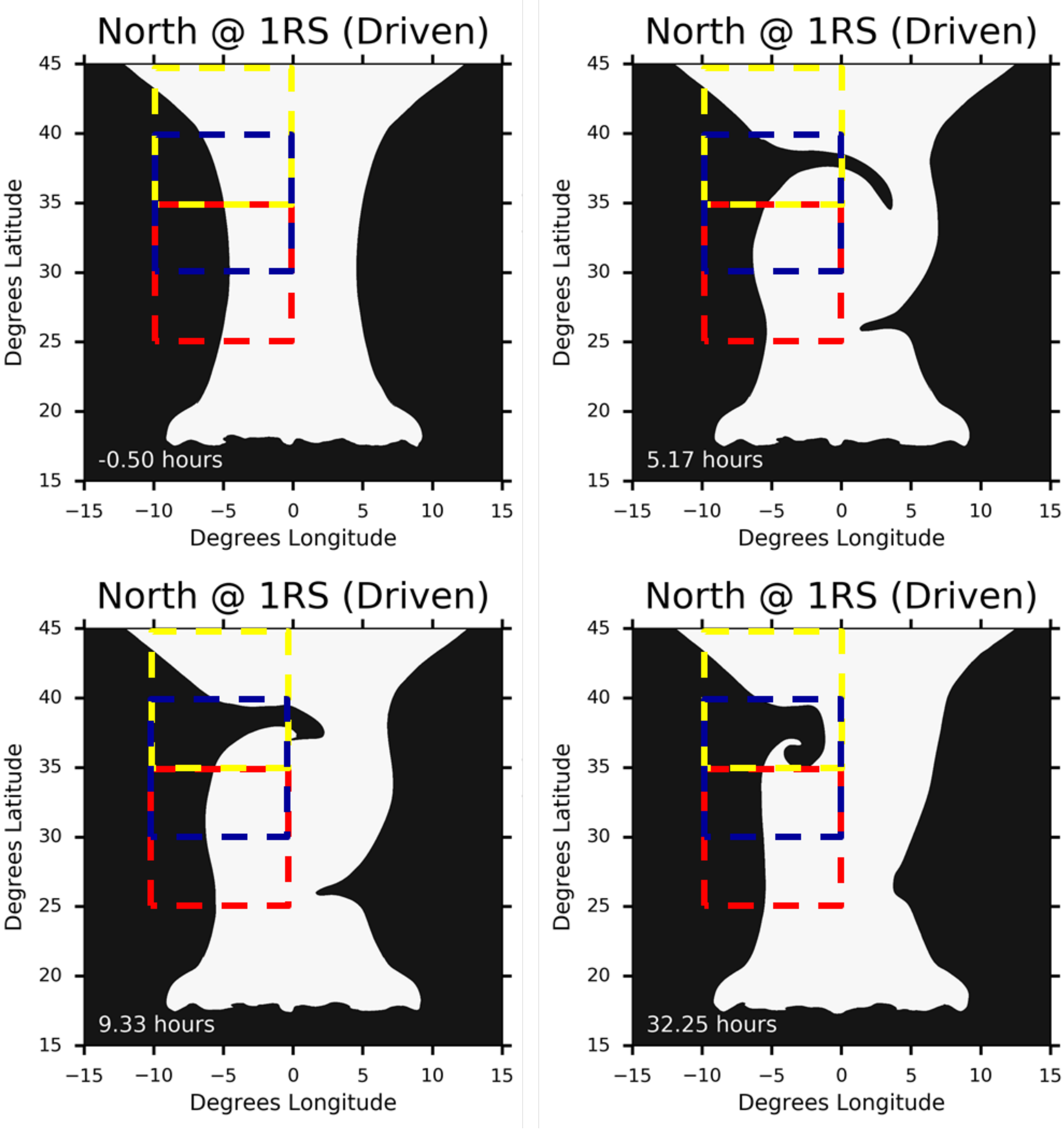

Figure 4.8: The coronal-hole boundary from the numerical simulation described in Chapter 3 at four key time periods. (Top left) Before the driving. (Top right) At the time of maximum displacement of the coronal hole boundary during the driving. (Bottom left) Near the end of the driving. (Bottom right) At the end of the simulation. In all panels the red, blue, and yellow boxes indicate the three regions from which field lines were traced for this analysis.

the simulation was then multiplied by the size of the bins. For the accumulated value, once a bin was found to contain one or more field lines, it was then counted for the duration of the simulation. In this manner, the accumulated value provides an estimate for the total area of the heliosphere that was affected by the S-Web dynamics over the course of the entire simulation.

These results are shown in Figure 4.9 for the red box, Figure 4.10 for the blue box, and Figure 4.11 for the yellow box. In all three figures the start and end times for the driving are demarcated and labeled. The yellow lines show the longitudinal areas and the blue lines show the latitudinal areas. The instantaneous and accumulated areas are plotted with dashed and solid lines, respectively.

Figure 4.9 shows the area covered by the field lines plotted from inside the red box in Figure 4.8. At the beginning of the simulation before the driving, the mapping is smooth, and the field lines, which are plotted up to half-way into the corridor, trace out half of the S-Web arc. Both $A_{I\phi}$ and $A_{A\phi}$ start at 30° but grow quickly once the driving is switched on. $A_{I\phi}$ then levels off for the remainder of the driving period, and begins to decrease again once the driving has ended, exhibiting a long relaxation phase. $A_{A\phi}$ continues to grow to more than 65° during the driving phase where it appears to saturate. Of course, the accumulated area can never decrease, so it remains at this value for the rest of the simulation. $A_{I\theta}$ and $A_{A\theta}$ both start at 30° as well. While $A_{A\theta}$ does rise to near 40° by the end of the simulation, the slow growth is illustrative of the fact that at the start of the simulation the field lines already cover the majority of the area in θ to which they can map. This is expected since at the beginning the center of the corridor maps to the apex of the S-Web arc. Between the center of the corridor and the coronal hole boundary, the field lines must sweep out half of the S-Web arc, covering the whole range of θ between the apex and the HCS. The value for $A_{I\theta}$ exhibits no real trend, falling to near 20° before rising and then falling again. This suggests that while the field lines were evenly distributed along the S-Web arc at the beginning, they quickly loose their symmetry and never reach an even distribution again. In

Figure 4.10, we see that the field lines from the blue box exhibit similar trends as those in Figure 4.9 although their areas grow to fill slightly smaller regions.

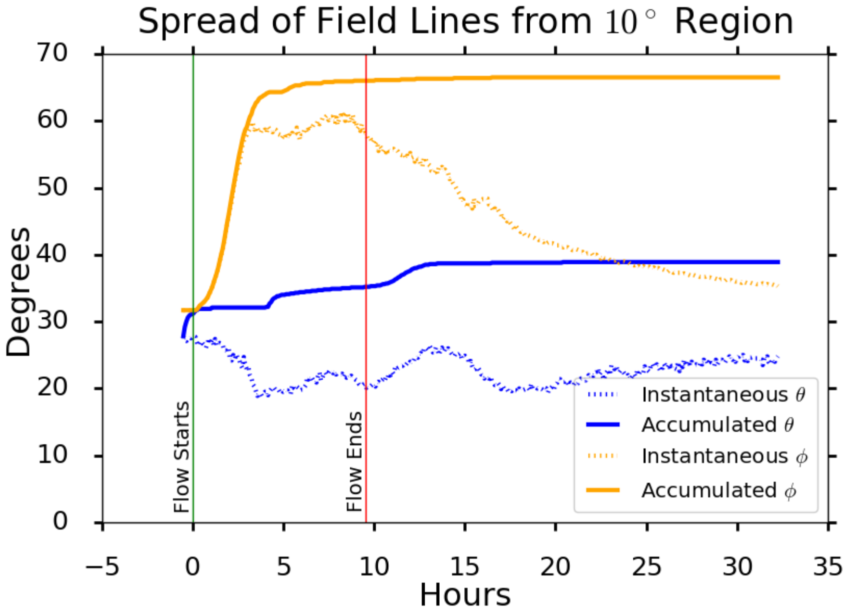

Figure 4.9: The change in instantaneous and accumulated areas in θ and ϕ with time covered by magnetic field lines traced from a box extending from -10° to 0° in longitude and 25° to 35° in latitude.

In Figure 4.11 we see that $A_{I\theta}$ remains flat throughout most of the simulation except for one disturbance which bumps up $A_{A\theta}$ as well. This is due to the fact that, as seen in Figure 4.8, the yellow box is much farther from the disturbance of the driving flow, and the majority of the open field lines are not immediately affected. This is also why $A_{I\phi}$ and $A_{A\phi}$ do not peak until the end of the driving. Additionally, in this region the coronal-hole boundary is experiencing the accumulated results of interchange reconnection, which, just as the ”melting” distortion from Figure 2.8, create a disturbance where there was originally none. This effect takes some time to build up and would not begin contributing to the increased values for $A_{I\phi}$ and $A_{A\phi}$ immediately.

Another way to look at these field lines is to watch the history of a given individual field line over time. We did this for all 8 million field lines traced in the three boxes above. Figures

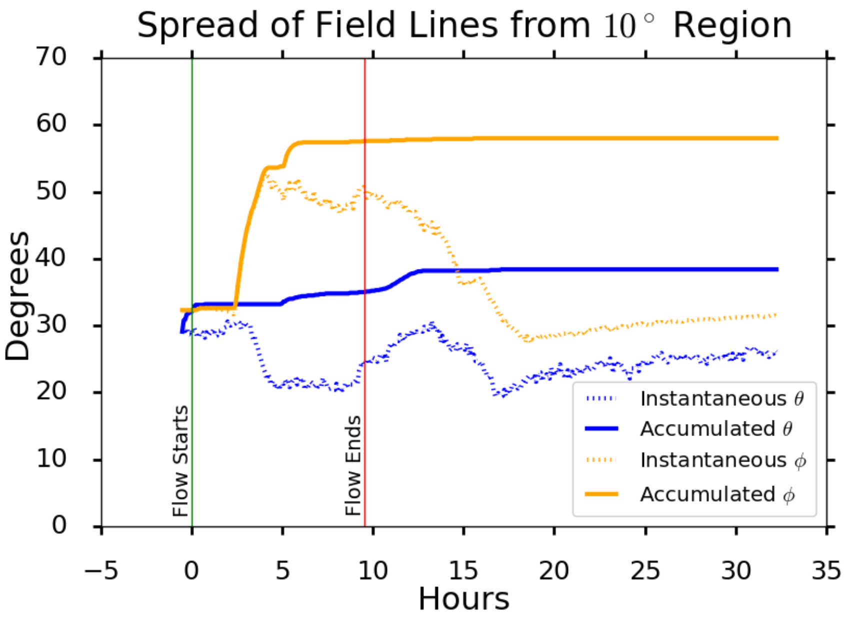

Figure 4.10: The change in instantaneous and accumulated areas in θ and ϕ with time covered by magnetic field lines traced from a box extending from -10° to 0° in longitude and 30° to 40° in latitude.

4.12 - 4.15 show a 2D histogram of the locations of a single field line on a radial surface at $12R_\odot$ over the course of the entire simulation. The 1D histograms shown along the axes are for latitude alone on the right and longitude alone on the top. The average location of the field line is calculated, along with the standard deviation in latitude and longitude. The three ellipses show the widths 1σ, 2σ, and 3σ away from the mean. The four histograms shown here demonstrate just a few characteristic patterns observed. It should be noted that the patterns in Figures 4.12 - 4.15 exist in all possible combinations in the field lines not shown here [1]. The locations varied greatly over time for many individual field lines. The ranges over which they varied was also drastically different between individual field lines. For all 8 million field lines, the average standard deviation was 3.4° in latitude and 8.7° in longitude. The standard deviations ranged from 0.4° to 11.6° in latitude and from 0.2° to 19.3° in longitude.

---

[1] IDIC: Infinite Diversity in Infinite Combinations

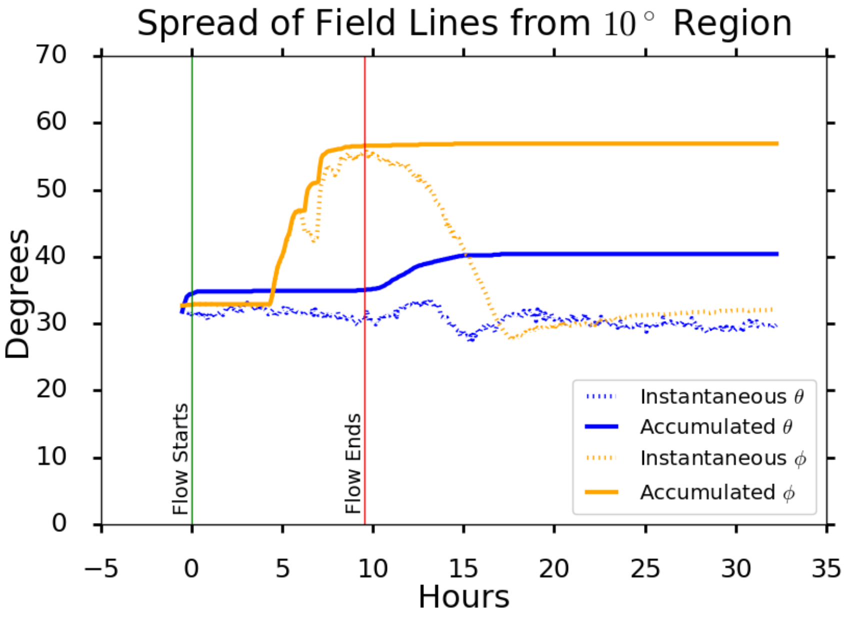

Figure 4.11: The change in instantaneous and accumulated areas in θ and ϕ with time covered by magnetic field lines traced from a box extending from -10° to 0° in longitude and 35° to 45° in latitude.

The first field line in Figure 4.12 is an example of how field lines can reconnect and jump all along the length of the S-Web arc (see Chapter 3). The second field line in Figure 4.13 also traverses a large portion of the S-Web arc, though it stays confined to the left side. In Figures 4.14 and 4.15 we see that not all field lines show this large spread though, with the field line staying confined to a particular latitude along the top of the S-Web arc, or even confined to an $\sim 10^\circ$ region near the HCS.

4.5 Discussion

The most important thing to note from this analysis is the difference between the static and the dynamic spread of the field lines. The driven state at the end of our driving period is the constant state for the Sun. The field lines traced from the same region on the Sun doubled the area of longitudes over which they were spread between the start and end of the driving. This is because as the driving moves the field on the surface it creates sharper

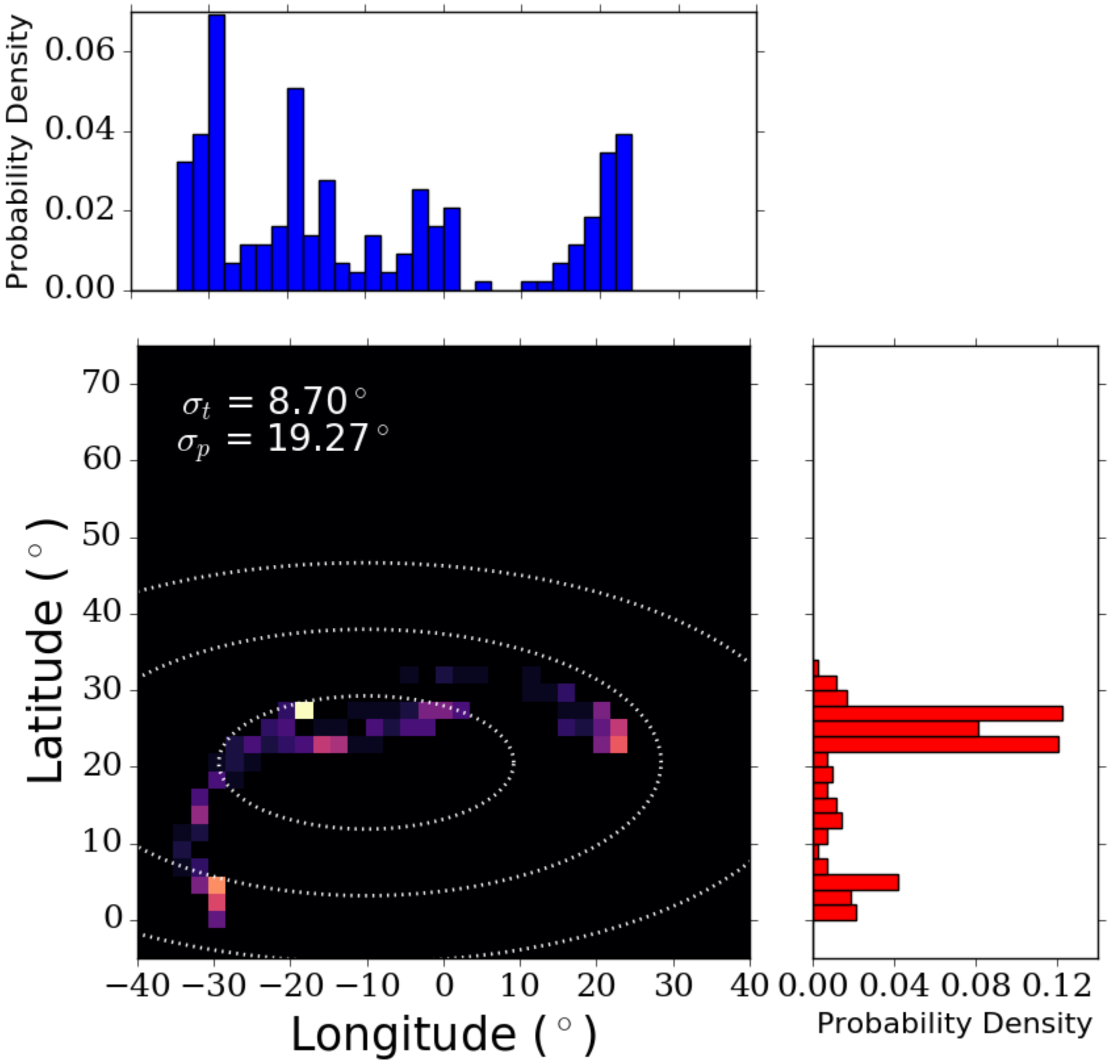

Figure 4.12: 2D histogram and it's components for a field line's location over the entire simulation. The ellipses show the first, second, and third standard deviations away from the mean location. This field line exhibited the largest spread in longitude, with a standard deviation close to 20°.

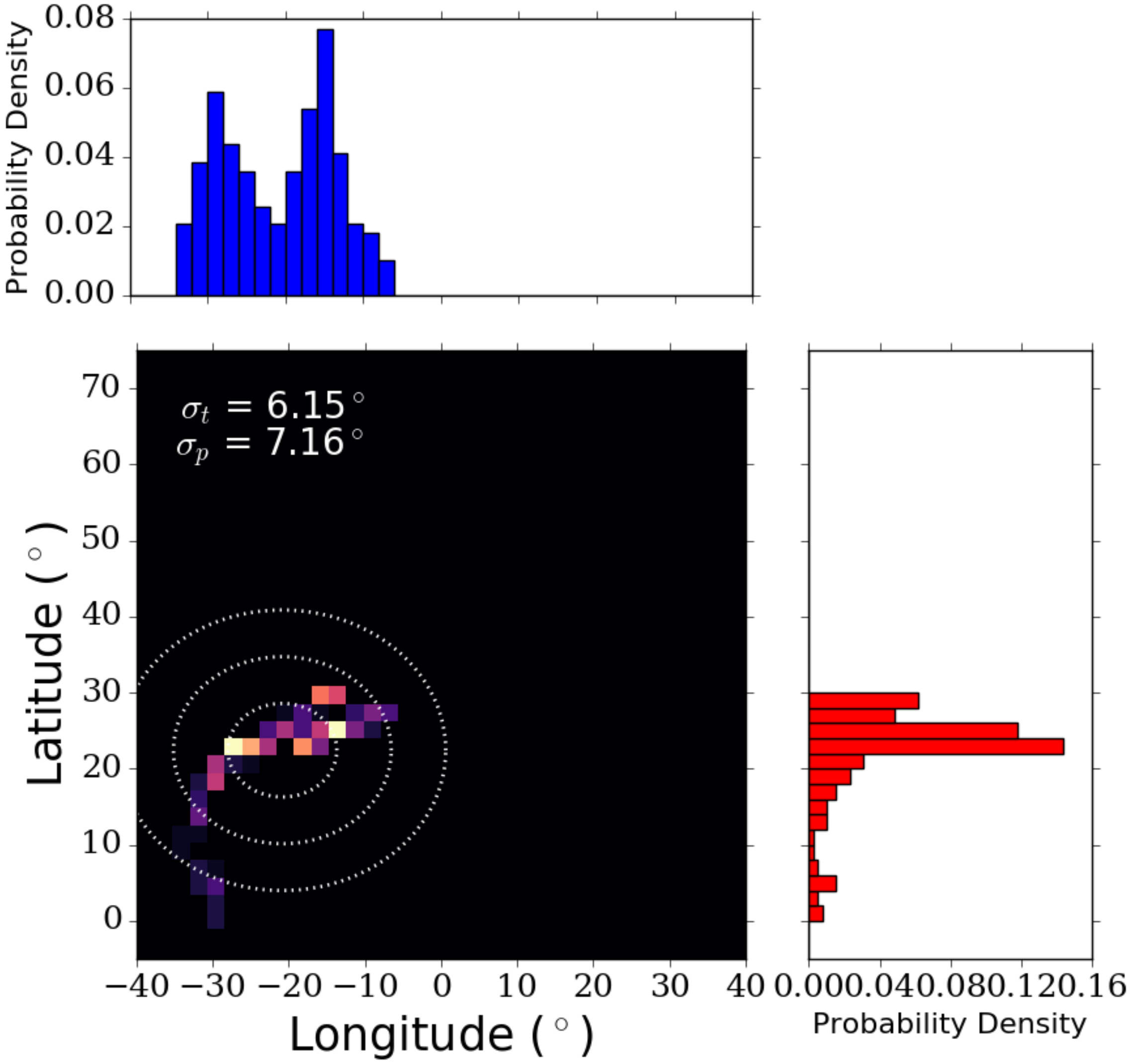

Figure 4.13: 2D histogram and it's components for a field line's location over the entire simulation. The ellipses show the first, second, and third standard deviations away from the mean location. This field line has a large spread in longitude, but is confined to a small range of latitudes.

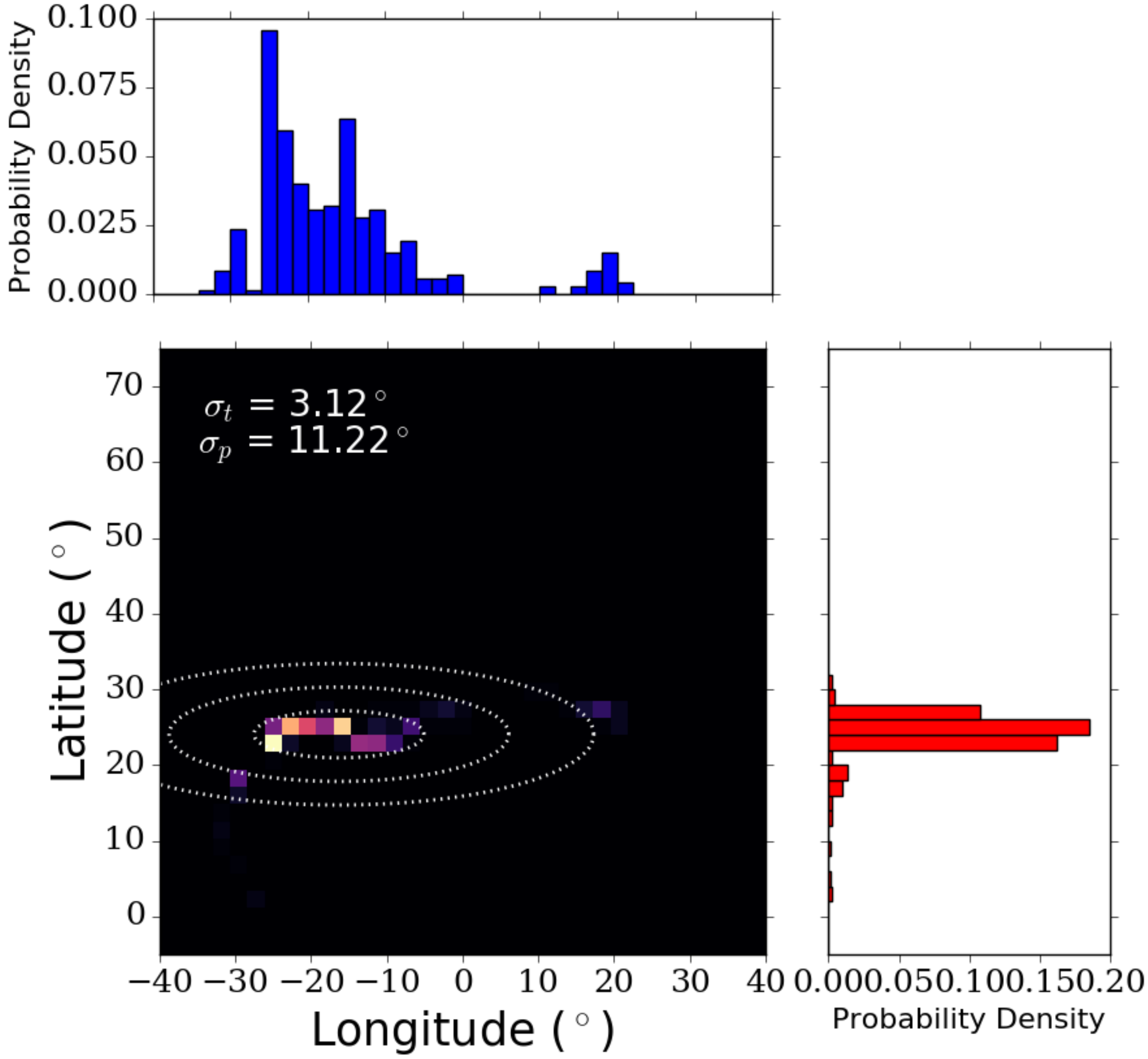

Figure 4.14: 2D histogram and it's components for a field line's location over the entire simulation. The ellipses show the first, second, and third standard deviations away from the mean location. This field line covered a wide range of latitudes and longitudes along half of the S-Web arc.

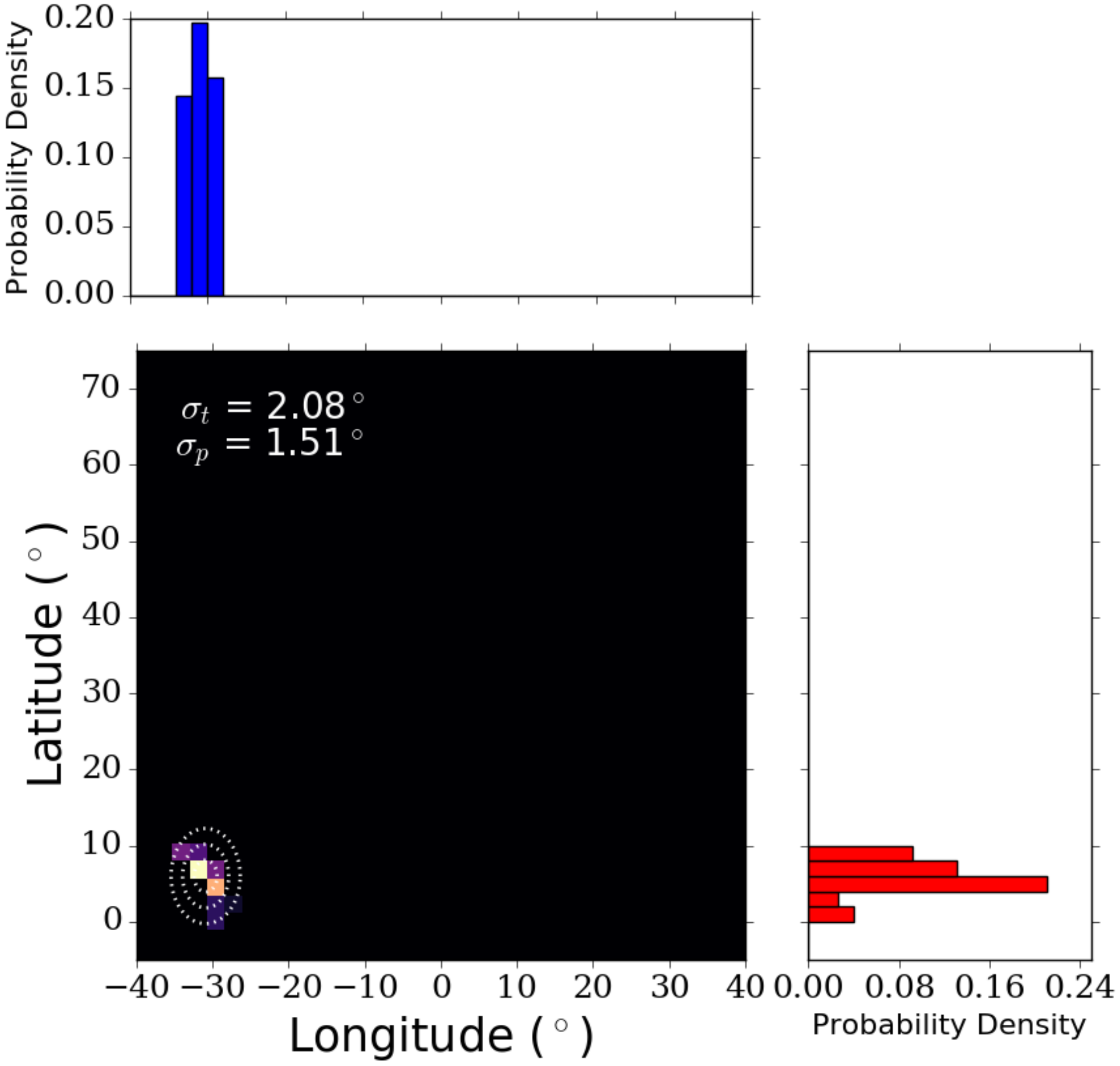

Figure 4.15: 2D histogram and it's components for a field line's location over the entire simulation. The ellipses show the first, second, and third standard deviations away from the mean location. Not all field lines showed a large spread. This field line stayed confined to within 10° of the HCS.

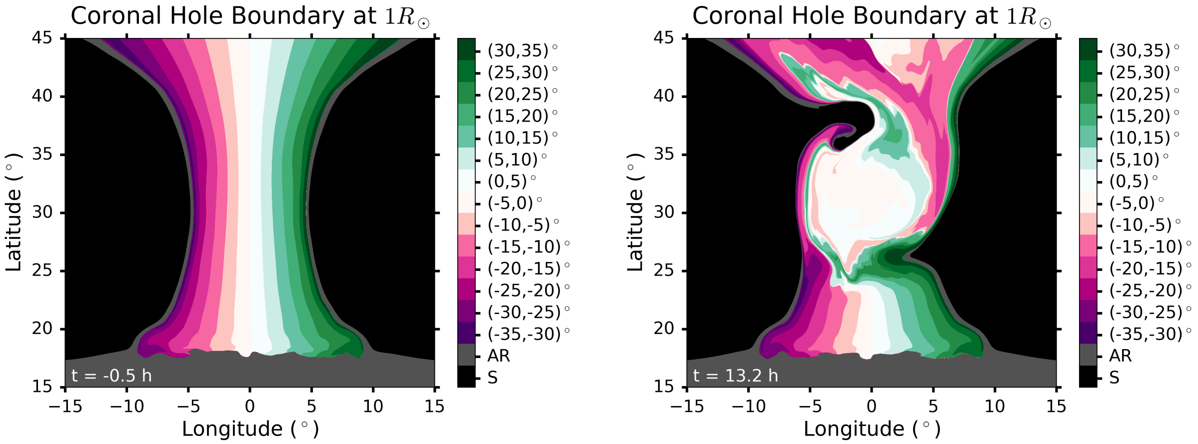

Figure 4.16: A map of the coronal hole boundary before driving and nearly four hours after driving. The field is colored by connectivity. Black regions map to closed field in the dipole in the northern hemisphere, while gray field

gradients in the mapping. This can be seen in the map of latitudes to which field lines in the corridor reach in Figure 3.6 and in the analogous map in Figure 4.16 showing the longitudes. Here we have colored all the open field lines in the coronal hole corridor based on their longitudes at $12R_\odot$. Just as in Figure 3.6 we see that before the driving (shown on the left in Figure 4.16) the mapping is smooth. On the right is that same map nearly four hours after the end of the driving. The flow has twisted the field (which launches an Alfvén wave) such that field lines which map to 60° apart in the heliosphere are next to each other on the photosphere. A large gradient in the mapping already existed across the S-Web corridor before the driving, but the structure and complexity of this gradient grows rapidly after being stirred in even this simple manner. Studies looking to identify field line spreading in the heliosphere using PFSS models grossly underestimate this spread of field lines because they assume the the smoothest possible potential field. It is the complex, dynamic state of the magnetic field which matters most.

It is tempting to consider the amount of time a field line spends connected to a flare region as proportional to the amount of flux observed along it, possibly reproducing the distribution in Figure 4.5. However, these particles paint out a picture of the magnetic field almost instantaneously as compared to the many-hour time scales for the dynamics observed in the simulation. Only if the time scale of the flare is sufficiently large compared to the time-scale over which field lines that are originally closed can become open and spread out along the S-Web arc, could it be possible to inject flare particles over an even larger region. Whether or not the rapid transport mechanisms observed in Chapter 3 and the tremendous amount of interchange reconnection observed in Chapter 2 are as important as the complex mapping within an open-field corridor must still be investigated.

Finally, these simulation results can easily explain the observation of energetic particle dropouts. With the development of the sharp gradients shown in Figures 3.6 and 4.16 as well as the tendency of the field lines to jump around the S-Web arc, it is easy to see how flux tubes that are not connected to the flaring region can become mixed in with flux tubes that are magnetically connected to the flare region.

4.6 Conclusions

We have demonstrated that the dynamic S-Web can easily double the field line spreading predicted by PFSS models, especially in regions such as coronal-hole corridors. While the largest spread of field lines in our simulation was only 60° in longitude, which is less than the observed 136° spread observed in-situ, our simulation was a simplification of the real-Sun. Factors such as the distribution of coronal-hole flux, and the size, duration, and complexity of the driver play a large role in the dynamics of the magnetic field. For example, one easy way to alter this simulation to achieve a larger spread than 60° would be to increase the size of the equatorial coronal-hole, which would change the location of the S-Web arc. The potential of the S-Web to explain SEP observations is especially strong given that sometimes impulsive SEPs have a large spread and sometimes they do not. This aspect is easily explained by the flare proximity to an S-Web arc as well as the structure of the S-Web itself. It is clear that the effects of the dynamic S-Web must be considered when evaluating the causes of wide-spread SEPs.

Co-authors for future publication of this chapter include S. K. Antiochos, C. R. DeVore, T. H. Zurbuchen, and P. F. Wyper. I would also like to acknowledge B. J. Lynch and D. J. Gershman for their helpful discussions.

CHAPTER V

Conclusions

5.1 Summary of Guiding Science Questions

5.1.1 Do motions at coronal-hole boundaries broaden the S-Web?

In Chapter 2 we presented a numerical simulation in which a photospheric driver was applied to a coronal-hole boundary to simulate supergranular rotation. We found that this driver increased the dynamic width around the HCS as predicted by the S-Web Theory. We also found that interchange reconnection along the coronal-hole boundary is the likely mechanism for the release of slow solar wind, allowing plasma from originally closed loops to escape onto open field lines. The large amount of interchange reconnection that was observed during the simulation, even though the driver was simple and of short duration, implies that this process could likely release the bulk of the slow solar wind that is observed in-situ. We also found that the manner in which this interchange reconnection moves the coronal-hole boundary can result in magnetic field some distance away from the driver being affected.

5.1.2 Can the dynamics along the boundary of a coronal-hole corridor release slow solar wind plasma at high latitudes?

In Chapter 3 we presented a numerical simulation in which a photospheric driver was applied, not to the coronal-hole boundary of a simple dipole, but to an S-Web corridor. We proved that photospheric motions across an S-Web corridor will result in the release of slow solar wind plasma at high-latitudes, thus explaining long-puzzling observations. Moreover, we showed that the original prediction of the S-Web theory underestimated the effects of photospheric driving. The S-Web theory originally predicted that coronal-hole corridors needed to be of very narrow width for supergranular rotation to result in the kind of magnetic reconnection which would release slow solar wind at high latitudes. We have shown that the effects of even a simple driver on the entire width of a fat S-Web corridor result in a mapping of the open field in lower-latitude coronal holes to the heliosphere that is far from smooth. This likely means that even large coronal-hole corridors can release slow solar wind at high latitudes.

5.1.3 What is the nature of these dynamics and what is their effect on the heliosphere?

In Chapter 4 we investigated the effects of photospheric driving on a coronal-hole corridor as they pertain to the large longitudinal spread of SEPs in the heliosphere. We found that S-Web dynamics dramatically increase the range of field line spreading over that predicted by static PFSS models. Additionally, the large gradients which develop in the mapping in open-field corridors are consistent with the observations of SEP dropouts. We also note that the S-Web theory can account for the variation of longitudinal spread between SEP events. It is possible that observations of impulsive SEPs depend on both the configuration of coronal-hole flux in the heliosphere and the position of the spacecraft relative to the S-Web. We conclude that the application of the S-Web to energetic particle observations is promising and warrants further study.

5.2 Suggestions for Future Work

The conclusions of the first numerical simulations of the dynamic S-Web are exciting and lead naturally to further study both observationally and numerically. Observationally, we are able to make predictions for the upcoming Solar Orbiter and Solar Probe Plus missions. One of the main discoveries of this dissertation is that the slow solar wind propagates outwards on field lines that can easily change their connectivity, resulting in many closed-field source regions. If this plasma is observed closer to its source, rather than at 1 AU, the gradients between these regions should sharpen. Therefore, it may be possible to pick out chunks within a slow solar wind stream that have different plasma properties reflecting their different origins within the magnetically closed corona. Related to this is the intense interchange reconnection observed at the coronal-hole boundary. Solar Probe Plus and Solar Orbiter should observe the effects of this reconnection in the magnetic field data, especially as they get closer to the Sun. Additionally, previous studies have found that reconnection does exist within the solar wind at 1 AU. How the nature of this reconnection changes with distance from the Sun may indicate whether or not this reconnection is the open-open reconnection observed in Chapter 4 or is fundamentally a separate process. To help with the predictions regarding the magnetic field, it would be possible to extract simulated in-situ observations from the calculations above to predict what exactly the instruments might observe as they fly through these S-Web arcs undergoing rapid magnetic reconnection and topological changes.

To further investigate the dynamic extent of the S-Web, two easy extensions of the above numerical simulations could be designed. First, by placing two or more smaller drivers along the S-Web corridor calculation in Chapter 4, it would be possible to study how the scale of the dynamics relates to the scale of the driver. Placing multiple drivers on either of the above simulations could also augment existing predictions of the extent to which open magnetic field can penetrate into the closed-field region. This dynamic width of the boundary is what determines the dynamic width of the S-Web and consequently the width of slow solar wind streams. Such calculations may also contribute to the discussion of the nature, width, and location of coronal-hole boundaries as observed in EUV measurements.

Another essential future calculation is one with multiple coronal-hole corridors. The nature of the interchange and open-open reconnection in Chapter 4 was that it spread field lines all along the extent of the arc. The next question is: Can field lines from one arc easily propagate across arcs? If so, this would result in an even larger longitudinal spread of field lines (and consequently plasma) in the heliosphere. This may be particularly important to the study of the longitudinal spread of SEP events.

For the prediction of SEP spread in the heliosphere, more theoretical calculations are needed. Future work should define the extent of spreading that is allowed by each of the following processes: diffusion, field line spreading over the time scale of particle propagation to 1 AU, and the degree of change in field line mapping in a small region within a coronal-hole corridor over the length of flare. By further quantifying each of these effects it would be possible to estimate the total longitudinal extent of these energetic particles in the heliosphere from a given coronal-hole flux distribution. One possible numerical calculation with a direct effect on SEP spread would be a simulation of an S-Web corridor as in Chapter 3, but with a much larger lower-latitude coronal hole. This would change the location of the S-Web arc within the heliosphere and could widen the longitudinal extent of energetic particles predicted by the calculations. Finally, now that a link between the S-Web and SEP longitudinal distributions has been established, a statistical study of the spread of SEP events compared to the flaring region's proximity to a coronal hole corridor (and consequently an S-Web arc) could be particularly enlightening.

APPENDICES

APPENDIX A

Methods for the S-Web Corridor Calculation

For this calculation we used the Adaptively Refined Magnetohydrodynamic (MHD) Solver (ARMS) to solve the following ideal 3D MHD equations in spherical coordinates:

$$\begin{aligned}
\frac{\partial\rho}{\partial t} + \nabla\cdot(\rho\mathbf{u}) &= 0, && \text{(A.1)}\\
\frac{\partial\rho\mathbf{u}}{\partial t} + \nabla\cdot(\rho\mathbf{u}\mathbf{u}) &= \frac{1}{4\pi}(\nabla\times\mathbf{B})\times\mathbf{B} - \nabla P + \rho\mathbf{g}, && \text{(A.2)}\\
\frac{\partial\mathbf{B}}{\partial t} - \nabla\times(\mathbf{u}\times\mathbf{B}) &= 0, && \text{(A.3)}
\end{aligned}$$

In the equations above, ρ is the plasma mass density, $\mathbf{u}$ is the plasma velocity, $\mathbf{B}$ is the magnetic field, P is the plasma pressure (defined by $P = 2\rho k_B T/m_P$), and $\mathbf{g}$ is the gravitational acceleration where $\mathbf{g} = -GM_\odot r/r^3$. ARMS uses Flux Corrected Transport methods to minimize diffusion and capture steep gradients. It uses a staggered grid to keep the magnetic field divergence to zero and solves the equations using a second-order predictor/corrector in time and a fourth-order integrator in space. Magnetic reconnection takes place only through numerical diffusion at locations where the current density develops fine structure at the grid scale. We do not use an explicit resistivity, but in these locations the effective numerical resistivity depends on the flow speed and grid spacing.

The domain and grid can be seen in Figure A.1. The domain extends from 1 to 30 solar radii, 11.25 - 79.75 degrees in theta, and -90 degrees to +90 degrees in phi. Figure A.1A shows the surface at the bottom boundary. The color contours show the radial magnetic field, and the block boundaries are also shown in black. Each block contains 8x8x8 grid cells. This is the layer of highly refined cells along the bottom boundary to ensure the velocity gradients as the solar wind is accelerated are appropriately resolved, as well as to capture the tangential velocities of the imposed driver. Figure A.1B shows Figure 3.3 from a different viewpoint. Additionally, a transparent radial surface at 12 solar radii has been added to show the grid structure. We refine all along the HCS and the S-Web arc in order to capture the desired dynamics. Near the poles and in the corners of the domain we allow to grid to coarsen to save computational power.

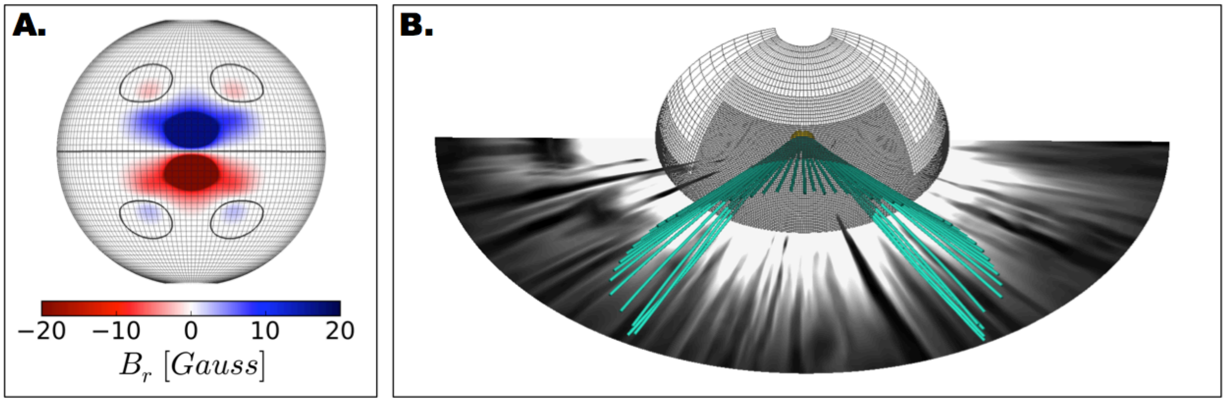

Figure A.1: Initial magnetic field and grid setup. A. A radial surface at 1 solar radius colored by the radial component of the magnetic field. The color bar is purposely saturated to show the small opposite polarity regions. At the equator the largest value for $|B_r|$ is 51.2 Gauss. The thick black lines represent the polarity inversion lines. The block boundaries of the grid at this bottom surface are also shown in black. B. A modification of Figure 3.3 viewed from above. A radial surface at 12 solar radii showing the block boundaries demonstrates how the grid is highly refined along the HCS and in the region encompassing the S-Web arch.

To initialize the atmosphere, we use Parkers transonic solar wind equation for an isothermal plasma (*Parker*, 1958):

$$\frac{v^2(r)}{c_s^2} \exp\left(1 - \frac{v^2(r)}{c_s^2}\right) = \frac{r_s^4}{r^4} \exp\left(4 - 4\frac{r_s}{r}\right), \tag{A.4}$$

where $v(r)$ is the solar wind speed, c_s is the sound speed ($c_s = 2k_BT_0/m_P$) and r_s is the sonic point ($r_s = GM_\odot m_P/4k_BT_0$). We assume an isothermal, fully ionized, hydrogen gas held at T = 1MK. We choose the initial plasma density at the bottom boundary to be 3.6 x 109 cm^{-3}. We set the radial bottom boundary condition to zero radial and tangential velocity (line-tying the magnetic field), and we allow mass to flow into but not out of the system. The 3 radial guard cells beneath this boundary are held at the initial density and velocity. Mass is allowed to flow through all other boundaries, and the magnetic field is extrapolated using zero-gradient conditions. The boundary conditions at the outer radial boundary extrapolate the radial velocity using zero gradient conditions, and allow for semi-slip conditions on the tangential components. For the side walls, the boundary conditions extrapolate the tangential velocity using zero gradient conditions and allow for semi-flow-through of the normal velocity components. These radial boundary conditions combined with the initial atmosphere profile create a self-sustaining solar wind that is replenished from below.

The magnetic field is initialized using the Potential Field Source Surface (PFSS) (*Altschuler and Newkirk*, 1969) solution for the configuration described in citetantiochos11, chosen specifically to create a narrow coronal-hole corridor. We set our source surface at 3 solar radii and we use the same configuration in the northern and southern hemispheres so that the system is initially symmetric across the equator. To start we use a global dipole at the center of the Sun such that the magnetic field on the surface at the poles is equal to 10 Gauss (*Long et al.*, 2013) and we have two polar coronal holes with a closed-field belt around the equator. We then add five dipoles near the surface to create the corridor, which can be seen in Figure A.1A. The large dipole straddling the equator has a maximum value of +/- 52 Gauss. This serves to pull the coronal-hole boundary from the poles towards the equator creating an elephant trunk. The width of this trunk is then modulated using the four additional dipoles, one on either side of the corridor in the north and south. The color bar was purposefully saturated to view the magnitude of these side dipoles, which is only

6.6 Gauss.

Once the magnetic field and atmosphere have been initialized, they are not in equilibrium. Therefore, we allow a period of relaxation before the driving, which allows the magnetic field and solar wind to find an unsteady balance between the solar wind pushing outward and the tension in the magnetic field. We do not use the highest resolution grid during this time, instead refining as the system reaches its equilibrium, allowing the system to relax as quickly as possible. After the system has relaxed, we then impose the surface flow to distort the coronal-hole boundary and observe the dynamics that follow.

To simulate the motion of supergranular convection, we impose a circular rotation across the corridor, which encompasses the coronal-hole boundary on either side (see Figure 2C). The flow is placed on the bottom boundary and has only theta and phi components. Supergranules on the Sun have radial and rotational motions. For distorting the magnetic field and injecting stress, the rotational component is the most important. Therefore, we use a purely rotational flow, which conserves the normal component of the magnetic field. To ensure

$$\frac{\partial B_r}{\partial t} = -\nabla_\perp \cdot (\mathbf{v}_\perp B_r) = 0, \tag{A.5}$$

we chose the perpendicular component of the velocity to be equal to the curl of a purely radial vector with components (ψ, 0, 0). We then define

$$\psi\left(\theta, \phi, t\right) \equiv V_0 f(t) g(\xi) h(\beta), \tag{A.6}$$

where

$$f(t) = \frac{1}{2}\left[1-\cos\left(2\pi k\frac{t-t_0}{t_2-t_1}\right)\right], \tag{A.7}$$

$$g(\xi) = \frac{(m+l+1)}{(l+1)}\left[1-\xi^{2(l+1)}\right]-\left[1-\xi^{2(m+l+1)}\right], \tag{A.8}$$

$$h(\beta) = \frac{1}{2}\beta^2. \tag{A.9}$$

The parameters k, t_0, t_1, and t_2 allow the manipulation of the amplitude of the flow so that the speed is gradually increased from zero to the maximum velocity and vice versa. This makes certain that all disturbances are smooth. Between the ramp up and ramp down phase we allow the flow to continue constantly at its maximum velocity. The equation for $g(\xi)$ defines an annulus in spatial coordinates where

$$\xi^2 \equiv 4\left(\frac{\theta-\theta_0}{\theta_2-\theta_1}\right)^2+4\left(\frac{\phi-\phi_0}{\phi_2-\phi_1}\right)^2. \tag{A.10}$$

The center of the annulus is at coordinate (θ, ϕ) and its extent is determined by the limits (θ_1, ϕ_1) and (θ_2, ϕ_2). We set m = l = 1, which yields a thick annulus with a velocity peak at the center of the annulus. In the equation for h, β is the magnetic field coordinate determined by

$$\beta \equiv \max\left(\min\left(B_r, B_2\right), B_1\right). \tag{A.11}$$

where we choose $B_1 = 0$ Gauss and $B_2 = 60$ Gauss so that β is always equal to B_r. The flow is centered at (32.5°, 0.0°). We chose a large diameter of 150,000 km so that the flow would capture both sides of the coronal-hole corridor. The flow is ramped up to a maximum velocity of 10 km/s over the course of 3 hours, allowed to continue at this speed for 3.5 hours, and then ramped back down to zero over the course of another 3 hours. Our maximum velocity is 10 km/s, and at no location does the maximum speed exceed 5% of the Alfvén speed.

Typical supergranules have diameters around 30,000 km and rotational speeds of 1 km/s. Our values were chosen to best simulate the properties of supergranular rotation and its effect on coronal-hole boundaries while still being computationally resolved. The flow spans 40 points in theta and 46 grid points in phi. After the driving has stopped the system is allowed to relax for an additional 22.75 hours. The driving and relaxation period afterwards are shown in the movies available online, which Figures 3.5 and 3.6 were extracted from.

APPENDIX B

Movies

Figure B.1: Full length movie corresponding to Figures 2.3 and 2.4. See text for details.

Figure B.2: Full length movie corresponding to Figure 2.6. See text for details.